

Doctoral Thesis

Water mass spiciness and thickness anomalies, and their
propagation in the upper North Pacific

北太平洋上層における水塊の
スパイシネス・厚さの偏差とその伝播

Tong Wang
(王 童)

Department of Geophysics
Graduate School of Science
Tohoku University

Thesis Committee Members

Professor Toshio Suga (Chair, Supervisor)
Professor Sayaka Yasunaka
Professor Tadahiro Hayasaka
Professor Kelvin J. Richards (University of Hawai'i)
Professor Bo Qiu (University of Hawai'i)
Professor Niklas Schneider (University of Hawai'i)
Associate Professor Shoichi Kizu
Associate Professor Shusaku Sugimoto
Associate Professor Futoki Sakaida
Senior Researcher Shinya Kouketsu (JAMSTEC)

Abstract

The thermohaline variations in oceans can be considered in two mechanisms. One is the density-compensated temperature and salinity anomalies, so-called spiciness anomalies. The other is the vertical displacement of isopycnals, which can be traced by the thickness anomalies of the isopycnal layers. Previous studies had proposed that spiciness and thickness anomalies can reflect multiple processes in the ocean and the air-sea interactions and can, in turn, impact the climate system through local and remote responses. However, the descriptions of their variations had been conducted mainly in 2-dimensions or short periods and were insufficient to understand their evolutions in space and time. This situation is mainly due to the limited observations before. In recent years, Argo observations, which started in the 2000s, reached both a data period and a spatial coverage that make it possible to describe three-dimensional spiciness and thickness anomalies from seasonal to decadal and longer time scales for the first time. On the other hand, the propagation processes of the anomalies had been investigated quantitatively in modelling studies, but they lack observational evidence.

The purpose of the present study was to give a comprehensive interpretation of spiciness and thickness anomalies in the upper North Pacific. The investigation was mainly based on Argo data. In order to catch and understand the features effectively, the investigation was conducted with foci on three typical water masses, Subtropical Mode Water (STMW), Central Mode Water (CMW), and Eastern Subtropical Mode Water (ESTMW). The first goal is to describe the temporal variations, spatial patterns, and spatial evolutions of the spiciness and thickness anomalies, and to link them with the characteristics and processes of the water masses (Chapters 3, 4). The study also aimed to quantify the effects of different processes on the propagation of the anomalies (Chapter 5)

In Chapter 3, the spiciness anomalies were investigated. The freshening of the subtropical thermocline was found within the Central Mode Water (CMW) and the North Pacific Intermediate Water (salinity minimum). Meanwhile, the salinity increased in the lighter layer within the North Pacific Tropical Water (salinity maximum). In the STMW, the salinity was dominated by a quasi-decadal variability and did not show rapid freshening. The interannual and longer variability in the CMW during the Argo period were described for the first time. The salinity of CMW decreased with a quasi-decadal variability, which was weaker and out of phase compared with the STMW. In the ESTMW, the salinity was dominated by year-to-year variability.

The spiciness anomalies originated mainly in the outcrop region of the isopycnals, where they were accompanied by the formation and the subduction of the mode waters. The subducted spiciness anomalies showed a good correlation with the meridional migration of the outcrop line and the associated mixed layer salinity anomalies in the western to central North Pacific. This correlation, combined with the spatial patterns, supported the southward pathway from the KE region to the STMW directly and is opposed to the westward pathway from the outcrop region in the eastern basin, which modelling studies had suggested. They propagated following the geostrophic current and decayed downstream. However, a few interannual anomalies found in the northern part of the CMW were almost dampened before spreading further south. In addition, some anomalies in the ESTMW appeared and intensified without a connection to the mixed layer. These anomalies occurred far from the outcrop line, suggesting the effects were likely caused by a salt-finger that is related to the modification of the mode waters. Furthermore, the propagation of the spiciness anomalies in the western to central subtropics was significantly faster than the geostrophic current and inclined to the inner side of streamlines. These indicated the transport by eddies in addition to geostrophic current.

In Chapter 4, the thickness anomalies were investigated. In the STMW, volume was dominated by a quasi-decadal variability, but it had an earlier phase than salinity. The thickness anomalies of its lighter and denser parts showed opposite signs in some years. The volume of the CMW showed a significant decreasing trend with a quasi-decadal variability that was out of phase of the STMW. The phase of CMW volume was lagged by CMW salinity. The regional confined robust year-to-year variations and the distinct variations between L-CMW and D-CMW, which were shown in CMW salinity, were not applicable to CMW volume. The ESTMW volume showed a quasi-decadal variability and a rapid shrinking in 2010-2011. The time scale of ESTMW volume was longer than that of salinity, indicating that the thickness anomalies were generated by processes other than spice injection.

A thicker STMW can be caused by both a thicker mixed layer and a wider outcrop range during its formation, indicating the role of late winter buoyancy loss in generating thickness anomalies. This correlation was weak in both CMW and ESTMW. The latitudinal position of outcrop line, which is important in generating spiciness anomalies, did not show a good correlation with thickness anomalies. The propagation of thickness anomalies was also faster than the geostrophic currents in the western subtropics but was slower than spiciness anomalies. Unlike spiciness anomalies, thickness anomalies with low frequency were preserved only in the upstream portion and decayed much more rapidly. In addition, the propagation velocity of thickness anomalies had a larger zonal component and a smaller meridional component in both

the western and eastern subtropics. The above differences between spiciness and thickness anomalies suggested the contributions of Rossby waves on propagating thickness anomalies, as suggested by previous studies.

Lag correlations were conducted between the anomalies and both the KE and PDO, and were discussed with the phenomena that imply large-scale synchronized variations. The time change rates of salinity and thickness of STMW showed correlations with KEI, at a lag of ~ 1 year and 0, respectively. The PDO phase shift in 2014 caused an increased volume and a decreased salinity in CMW. ESTMW and CMW showed opposite correlations with PDO with a 1-year delay in thickness. The lower part of ESTMW and the lighter part of STMW showed synchronized thickness anomalies, and is consistent with their correlations to PDO at a lag of 1–2 years. Besides, thickness anomalies of different time scales were generated west and east of the dateline on the CMW density range and propagated at different directions and speeds.

In Chapter 5, we estimated the contributions of different processes involved in the propagation of the signals. Based on a salinity conservation equation on isopycnals, this study reconstructed the propagation of spiciness anomalies with observational data for the first time. It demonstrated the dominant role of the mean advection term in the propagation of the spiciness anomalies. The two time-dependent terms, which are the anomalous advection term and the eddy term, can induce the anomalies with a different phase from the mean advection term and the anomalies with high frequency, especially in the western subtropics, respectively. Large deviations were found in the upstream region near the outcrop line and the ESTMW distribution region. They were likely caused by neglecting the mixing and diffusion and missing data near the outcrop line. Nevertheless, this study shows the possibility of quantitatively estimating the propagation processes based on observational data and providing instructive results.

Finally, using a high-resolution reanalysis dataset, we calculated the eddy-induced bolus velocity, which cannot be fully resolved in Argo data. The southward and westward components in the STMW regions can explain the propagation speed faster than the geostrophic speed and the propagation pathway to the inner side of the streamline in the western subtropics. However, the bolus velocity is insufficient to explain the observed speed difference fully. Besides, the different propagation velocities between spiciness and thickness anomalies were not explained in this study. Therefore, future work was expected to estimate the effects of other processes such as Rossby waves and submesoscale eddies.

Acknowledgement

First of all, I would like to express my deepest gratitude to my supervisor, Professor Toshio Suga, for the constant guidance throughout the doctoral course. I have been extremely lucky to have a supervisor who is always patient to answer my questions and respond to my requests. He not only gave me concrete advice on every step of my study, but also taught me how to grow as a researcher. I also appreciate the opportunities he gave me to connect with other researchers. What I learned from him will be instructive in my whole life.

The completion of this dissertation would not have been possible without the scientists cooperated with me. Dr. Shinya Kouketsu at Japan Agency for Marine-Earth Science and Technology provided me with the dataset used in this study and gave me priceless suggestions on the revision of my work. Professor Kelvin J. Richards, Professor Bo Qiu, and Professor Niklas Schneider at the University of Hawai'i had intense discussions with me and gave me invaluable recommendations on my study.

I am also grateful to all the people I met in the Physical Oceanography group, Tohoku University during the last 6 years. I gratefully acknowledge Professor Kimio Hanawa, Professor Sayaka Yasunaka, Professor Shoichi Kizu, Professor Shusaku Sugimoto and Professor Futoki Sakaida for the inspiring comments and discussions on both my work and the fundamental scientific topics. Thanks should also go to Ms. Akane Oikawa and Ms. Sachie Prestel for supporting my study activities in the laboratory. Mr. Daiki Ito, Mr. Ryohei Yamaguti, Mr. Takato Nakai, Mr. Satoshi Kimura, Mr. Yuta Murai, Mr. Mochamad Riza Iskandar, Ms. Mina Sasaki, Mr. Masato Kanakubo and Mr. Shinya Suzuki, who are my upper-level students, helped me a lot to get my life on track when I first arrived in Japan and gave me useful advice on my study. Graduates and students Mr. Kazuki Hidaka, Mr. Kaihei Yamazaki, Mr. Terao, Mr. Terakawa, Mr. Karaki, Ms. Yanguo Li, Ms. Mizuki Iida, Ms. Fumika Sanbe, Mr. Suguru Hanzawa, Mr. Satoshi Nitta, Mr. Shunsuke Okada, Mr. Hanani Adiwira, Ms. Saki Okamoto, Mr. Shota Sera, Mr. Asuto Sakai, Mr. Tomoya Kubo, Mr. Yusuke Miura, Ms. Ratu Almira Kismawardhani, Ms. Emelie Breunig, Mr. Yoshinobu Furukawa, Mr. Naoto Horigome, Mr. Ryota Miyaki, Mr. Hikaru Goto, Mr. Gaku Nishihira, Mr. Hayato Kanazawa, Mr. Tomoharu Saito, Mr. Jin Furuya, Ms. Yui Kobayashi, Ms. Aya Takagi, Mr. Riku Shinohara, Ms. Harua Uno, and Mr. Shuzo Kambayashi shared interesting moments with me during the seminar, coffee break, drinking party and the cruise. It's so nice to be your labmate. I would like to

extend my sincere thanks to Professor Dongliang Zhao at Ocean University of China and the late Professor Yoshiaki Toba for helping me get into contact with this group.

I am deeply indebted to the International Joint Graduate Program in Earth and Environmental Sciences (GP-EES), Tohoku University for providing me continuous financial support and opportunities of research activities. Many thanks to Ms. Shinobu Okuyama, Prof. Shin Ozawa and the other professors, staff, and students in GP-EES for their encouragement and help. I also received financial support by the JSPS KAKENHI Grant JP19H05700 and the e-Asia Joint Research Program: Marine Heat Waves in the Western Pacific.

Last but not the least, I would like to express my thanks to people who have given me spiritual power. I am deeply grateful to my beloved parents, grandparents, and other family members. Only with their care and love can I get over the days during which I almost gave up. My parents always do their best to understand and support my dreams, which makes it possible for me to accomplish the doctoral course. I thank my old friends in China and the friends I met in Sendai, other cities in Japan, and Hawaii for cheering me up and believing in me. I also thank my icon, Yuzuru Hanyu, who triggered me to consider studying in Sendai. It's exciting to say goodbye to my student days and start a new stage of life in the same season he turned to a professional athlete.

Contents

Abstract.....	i
Acknowledgment.....	iv
Contents.....	vi
1 General Introduction	1
1.1 Background.....	1
1.1.1 Mechanisms and Tracers	1
1.1.2 Water masses in the upper North Pacific.....	2
1.2 Scope of the present dissertation	2
2 Data and Methods	5
2.1 Observational data on isopycnal surfaces.....	5
2.2 Observational data of the mixed layer	5
2.3 High-resolution reanalysis data	5
2.4 Definitions	5
2.4.1 Geostrophic stream function.....	5
2.4.2 Potential vorticity (Q).....	6
2.4.3 Turner angle (Tu).....	6
3 Spatiotemporal evolutions of spiciness anomalies.....	7
3.1 Introduction.....	7
3.2 Mean state	9
3.3 Temporal variations of salinity	14
3.3.1 Linear trend.....	14
3.3.2 STMW	15
3.3.3 CMW	16
3.3.4 ESTMW	17
3.4 Spatial patterns of spiciness anomalies.....	18
3.5 Propagation direction and velocity of spiciness anomalies	20
3.6 Possible origins of spiciness anomalies	23
3.6.1 Vertical structure of the spiciness anomalies.....	23
3.6.2 Meridional shift of the outcrop line	24

3.6.3 Double-diffusion.....	27
3.7 Summary and discussions.....	27
4 Spatiotemporal evolutions of thickness anomalies.....	50
4.1 Introduction.....	50
4.2 Mean state.....	52
4.3 Temporal variations of thickness anomalies.....	52
4.4 Spatial patterns of thickness anomalies.....	56
4.5 Propagation direction and velocity of thickness anomalies.....	57
4.6 Relations of spiciness and thickness anomalies with KEI and PDO.....	59
4.7 Conclusions and discussions.....	62
5 Propagation processes of water mass anomalies.....	83
5.1 Estimation of propagation processes along streamlines by salinity conservation equations.....	83
5.1.1 Methodology.....	83
5.1.2 Forward integration.....	84
5.1.3 Backward integration.....	85
5.2 Estimation of eddy effects with bolus velocity.....	86
5.3 Discussions and conclusions.....	87
6 General conclusions.....	99
References.....	99

1 General Introduction

1.1 Background

1.1.1 Mechanisms and Tracers

Physical variations in the ocean can be divided into two dynamics. One is temperature and salinity variations at a fixed isopycnal, and the other is the vertical displacement of isopycnals (Bindoff and McDougall, 1994). The density-compensated temperature and salinity variations are also referred to as spiciness anomalies, being large with warm and salty water (Munk, 1981). The occurrence of spiciness anomalies is accompanied by pure warming or cooling and pure freshening or salinification. The vertical displacement of isopycnals is accompanied by pure heaving, and can be affected by freshening and warming, causing variations of thickness and depth of an isopycnal layer.

The above variations are affected by various processes in the climate system. Spiciness anomalies can be affected by air-sea heat and freshwater fluxes related to surface warming, changes in evaporation and precipitation, and can also change in response to the ocean circulation including anomalous advection. Vertical displacement of isopycnals can be caused by circulation changes, including wind-driven Ekman transport (Nieves and Spall; Jayne and Marotzke, 2001) and upper ocean ventilation.

The signals generated through atmospheric forcing and ocean adjustment can further cause local and remote responses and, in turn, influence the climate system. To a first-order approximation, spiciness anomalies are advected like a passive tracer (Schneider et al., 1999). Since first hypothesized by Gu and Philander (1997), various modeling studies (Nonaka and Xie, 2000; Schneider, 2000; Yeager and Large, 2004; Luo, 2005; Nonaka and Sasaki, 2007; Furue et al., 2018) have demonstrated that spiciness anomalies generated in the subtropics are subducted to the thermocline and propagated to the equatorial Pacific, and finally play an important role in climate variability through upwelling. On the other hand, vertical displacement of isopycnals is governed by planetary wave dynamics (Latif and Barnett, 1996). Also, by modelling study, Schneider et al. (2002) suggested that Rossby waves carry thermocline depth perturbations to the west, affecting the Kuroshio Extension and resulting in SST anomalies. Therefore, for a better understanding of the varying climate and a more accurate prediction, it is necessary to have a clear cognition of the above anomalies. However, the observational evidence of the above scenarios is still limited, mainly due to the short and sparse in situ observations before the 2000s, observational evidence has been limited.

In this study, the main tracers we used to detect spiciness anomalies and vertical displacement of isopycnals are salinity anomalies on isopycnals and thickness anomalies of isopycnal layers respectively.

1.1.2 Water masses in the upper North Pacific

In order to describe the features of spiciness and thickness anomalies effectively, it is useful to focus on water masses. A water mass is a body of ocean water with a common formation history and a distinctive narrow range of water properties. Spiciness anomalies are related to variations of thermohaline properties and structures of the water masses. Vertical displacement of isopycnals is related to changes in formation and subduction of water masses and their different proportions.

There is a typical kind of water masses in the upper ocean called “mode water”, characterized as water masses with nearly vertical homogeneity over a relatively large area (Hanawa and Talley, 2001). There are three types of mode waters, whose distributions are shown in Figure 1.1: Type I, the subtropical mode waters (STMW), which are associated with subtropical western boundary currents; Type II, the eastern type of subtropical mode waters (ESTMW), which is located in the eastern part of the subtropical gyres; Type III, a denser type of subtropical and subpolar mode waters (Hanawa and Talley, 2001).

In the upper North Pacific, the three types of mode waters are Subtropical Mode Water (STMW; Masuzawa, 1969), located in the western part of the North Pacific subtropical gyre; Eastern Subtropical Mode Water (ESTMW; Hautala & Roemmich, 1998), located in the eastern part of North Pacific subtropical gyre); and Central Mode Water (CMW; Nakamura, 1996; Suga et al., 1997), located just south of the Subarctic Front. Mode waters are formed in the deep mixed layer in the late winter and are capped by the seasonal thermocline in spring (Bingham, 1992). They can carry signals from the mixed layer to the permanent thermocline through subduction, from their formation regions to wider regions during their spreading, and, in turn, impact the mixed layer properties through reemergence (Hanawa and Sugimoto, 2004; Sugimoto, 2005) or obduction (Endoh et al., 2006; Qiu & Huang, 1995). Thus, it is instructive to understand the spiciness and thickness anomalies considering the processes of mode waters.

1.2 Scope of the present dissertation

Based on the previous section (1.1 Background), the present study's purpose is to comprehensively describe spiciness anomalies and thickness anomalies in the upper North

Pacific. Specifically, this dissertation has two objectives. The first one describes the spatial and temporal evolutions of the anomalies, focusing on STMW, CMW, and ESTMW, including comparisons between them (Chapter 3 for spiciness anomalies and Chapter 4 for thickness anomalies). The second one is quantifying the anomalies' propagation and the contributions of different processes (Chapter 5).

The investigation is mainly based on observational data from the Argo program. The vertical coordinates for detecting spiciness and thickness anomalies are neutral density (γ) coordinates for preserving water mass structures better than isobaric coordinates.

The structure of the present dissertation is as follows.

Chapter 2 introduces the datasets information and methods in this study.

In Chapter 3, we investigated the mean state, temporal variations, spatial patterns, and propagation of spiciness anomalies. Because the spreading patterns of the spiciness anomalies are generally consistent with the direction of the geostrophic currents, we investigated the propagation velocity along geostrophic streamlines and discussed the propagation pathways. Besides, we also discussed the possible origins and generating mechanism of the spiciness anomalies.

In Chapter 4, we investigated thickness anomalies in similar aspects as in Chapter 3, i.e., mean state, temporal variations, spatial patterns, and propagation pathway and speed. We also compare the behavior of thickness anomalies with that of spiciness anomalies. Based on similarities and differences between spiciness and thickness anomalies, we further discussed the related processes and characteristics that cause the variations, including the correlation analyses with large-scale variability of KE and PDO.

In Chapter 5, we investigated the roles of different processes in propagating spiciness and thickness anomalies. First, we quantitatively estimated the contributions of different kinds of processes with Argo observations. Second, because the resolution of Argo floats is not enough to fully resolve eddies, we use a high-resolution reanalysis dataset to examine the effects of eddy transport. The results are discussed combined with the unsolved issues in Chapters 3 and 4.

Finally, Chapter 6 provides general conclusions and raises future perspectives.

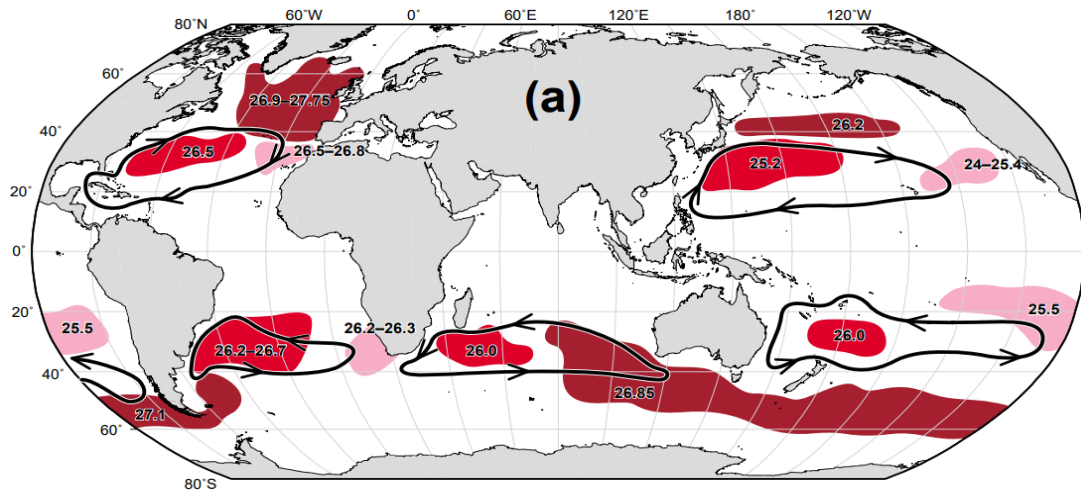


Figure 1.1 Mode water distributions in the world's oceans (Hanawa and Talley, 2001). Red-colored areas show the subtropical mode waters (the first type). Pink-colored areas show the eastern type of subtropical mode waters (the second type). Brown-colored areas show the third type of subtropical and subpolar mode waters. Approximate potential densities (σ_0) are indicated. Black arrows denote the subtropical gyre circulation.

2 Data and Methods

2.1 Observational data on isopycnal surfaces

This study uses temperature and salinity profiles obtained from the Argo profiling floats. The profiles are processed into monthly $1^\circ \times 1^\circ \times 0.05 \gamma$ gridded data of salinity, potential temperature, and thickness following the methods described in Kouketsu et al. (2017) and are extended to 2018 (Argo, 2019). Although the Argo program started in 2000, we focus on the 2004-2018 period because the floats in North Pacific are reasonably sampled only since 2004.

2.2 Observational data of the mixed layer

MILA GPV (Mixed Layer data set of Argo, Grid Point Value) product based on Argo profiles is used, with the mixed layer depth (MLD) being defined by a minimum thickness of either $\Delta\sigma_\theta=0.125\text{kg/m}^3$ or $\Delta T=0.5^\circ\text{C}$ from 10 dbar (Hosoda et al., 2010). To match up to the $1^\circ \times 1^\circ$ isopycnal surface data, the mixed layer data are interpolated onto $1^\circ \times 1^\circ$ grids.

The outcrop line of a γ surface is defined by the contour where the averaged mixed layer neutral density, calculated from the averaged mixed layer temperature and salinity in MILA GPV, is equal to the specified γ value.

2.3 High-resolution reanalysis data

Four-dimensional variational ocean re-analysis for the Western North Pacific over 30 years (FORA-WNP30) (Usui et al., 2017) are used to resolve mesoscale eddies.

The domain of the dataset is $117^\circ\text{E}-160^\circ\text{W}$, $15^\circ\text{N}-65^\circ\text{N}$, and the spatial resolution is $1/10^\circ$ ($1/6^\circ$ east of 160°E) longitude \times $1/10^\circ$ ($1/6^\circ$ north of 50°N) latitude. The period used in this study is 2004-2015. The number of vertical levels is 54 (0-6300m).

In this study, we interpolated the dataset from pressure coordinates to potential density coordinates with a similar range as 2.1 using the Akima spline (Akima, 1970).

2.4 Definitions

2.4.1 Geostrophic stream function

Approximate geostrophic stream functions and velocities were computed on γ surfaces following McDougall and Klocker (2010) (with the use of GSW V3.0 library, TEOS-10), which

is more accurate than the more commonly used Montgomery stream functions (Montgomery, 1937) for isopycnal or neutral surfaces. The zero-velocity reference level was set to 1500 dbar.

2.4.2 Potential vorticity (Q)

The calculation of potential vorticity (Q) follows Talley (1988), neglecting relative vorticity:

$$Q = \frac{f \Delta\rho}{\rho \Delta z}, \quad (1)$$

and is applied to γ coordinates as:

$$Q = \frac{f}{\gamma + 1000} \frac{\Delta\gamma}{\Delta z}, \quad (2)$$

where f is the Coriolis parameter, and $\Delta\gamma/\Delta z$ is calculated by the range of $\gamma \pm 0.025$ and its thickness.

2.4.3 Turner angle (Tu)

Tu was calculated as:

$$Tu = \tan^{-1} \left(\alpha \frac{\partial\theta}{\partial z} - \beta \frac{\partial S}{\partial z}, \alpha \frac{\partial\theta}{\partial z} + \beta \frac{\partial S}{\partial z} \right) \quad (3)$$

after McDougall et al. (1988), where θ is conservative temperature, α is thermal expansion coefficient and β is salinity contraction coefficient.

3 Spatiotemporal evolutions of spiciness anomalies

3.1 Introduction

The observational evidence of spiciness anomalies has been limited, mainly due to insufficient observations. The basin-wide network of expendable bathy-thermograph (XBT) observations detected decadal temperature signals propagated from the North Pacific subtropics to tropics (Schneider et al., 1999; Zhang & Liu, 1999). However, without salinity observations, these studies cannot separate the density-compensated spiciness anomalies from the temperature anomalies caused by wave dynamics. Repeat hydrographic data revealed spiciness anomalies in the thermocline in North Pacific Tropical Water (NPTW) (Suga et al., 2000), in Subtropical Mode Water (STMW) (Oka et al., 2017), and near Hawaii (Lukas, 2001; Lukas & Santiago-Mandujano, 2008). Nevertheless, they are limited to specific sections or a small area; hence, they cannot provide a three-dimensional description of how the spiciness anomalies evolved.

Since the early 2000s, the Argo program has provided a global dataset with spatially and temporally unbiased sampling (Roemmich et al., 2009) and makes it possible, for the first time, to describe large-scale three-dimensional evolution of spiciness anomalies. Sasaki et al. (2010) first detected a negative spiciness anomaly on $\sigma_\theta = 25.0 - 25.5$ originated at the eastern subtropical North Pacific and propagated southwestward during 2004-2008, with speed consistent with the mean geostrophic velocity. Kolodziejczyk and Gaillard (2012) and Li et al. (2012) detected similar propagations from both northeastern and southeastern Pacific. They also found the spiciness anomalies diffusing along the pathways but reaching the equator, which proves the important role of spiciness anomalies suggested by modeling studies. Propagation of spiciness anomalies is also observed in NPTW on $\sigma_\theta = \sim 24$ (Katsura et al., 2013), in South Pacific Tropical Water on $\sigma_\theta = 24.5$ (Zhang & Qu, 2014), in Subtropical South Atlantic on $\sigma_\theta = 26.3$ (Kolodziejczyk et al., 2014), and in South Indian Ocean on $\sigma_\theta = 24.0\sim 25.0$ (Li and Wang, 2015).

Spiciness anomalies are mainly generated in the formation regions of thermocline water masses, by processes including air-sea interactions (Bindoff and McDougall, 1994), anomalous advection across the mean isopycnal spiciness fronts (Schneider, 2000), and diapycnal mixing across subducted isopycnals (Yeager and Large, 2004).

As stated above, previous observational studies in the upper North Pacific mainly concentrated on spiciness anomalies in the tropics or the eastern subtropics; the latter has a relationship with the variability of ESTMW (Sasaki et al., 2010; Katsura, 2018), while those in

STMW and CMW have not been described sufficiently in three-dimension yet. However, early studies have suggested that STMW and CMW have various variabilities in formation, distribution, and dissipation. First, STMW formation has interannual to decadal variations attributed to the variability in atmospheric forcings, such as wintertime monsoons (Hanawa, 1987; Suga and Hanawa, 1995; Taneda et al., 2000). Another topic of current interest is the decadal variability of STMW (Cerovecki & Giglio, 2016; Miyazawa et al., 2009; Oka et al., 2015; Qiu et al., 2007; Qiu & Chen, 2006) related to the decadal variability of Kuroshio Extension (KE) system (Qiu et al., 2014; Qiu & Chen, 2005). Besides, CMW temperature decreased after the 1976/1977 regime shift related to surface heat loss and Ekman transport associated with the intensification of the westerlies (Yasuda and Hanawa, 1997). This change is later considered as decadal variability of CMW caused by PDO by numerical simulations (Ladd and Thompson, 2002; Hosoda et al., 2004), and is also observed in 1988/1989 with temperature and salinity increased but only along 180° repeat section (Suga et al., 2003). Additionally, mesoscale eddies can also affect the formation and distribution of STMW (Nishikawa et al., 2013; Nishikawa et al., 2010; Pan & Liu, 2005; Uehara et al., 2003) and CMW (Qu et al., 2002; Oka et al., 2009; Kouketsu et al., 2011).

The aforementioned variability of STMW and CMW processes addressed the need to explore what consequent anomalies occur in their properties and how these anomalies spread. However, due to the inadequate salinity observations before the Argo period, observational evidence of spiciness anomalies is still insufficient. Oka et al. (2017) demonstrated the freshening trend and decadal variability of salinity in STMW, but their investigation is only along the 137°E section. Using Argo observations, Yan et al. (2017) detected a freshening trend on $\sigma_\theta = 24.5\text{-}25.4$ in the eastern Luzon Strait during 2003-2012, which can be traced back to the northwestern subtropical outcrop region. However, they did not mention its association with STMW. Li et al. (2019) demonstrated a positive salinity trend for the upper 200m and a freshening trend for the 200-600m in the Pacific Ocean during 2005-2015. However, their study is on isobaths rather than isopycnals.

The purpose of this chapter is to comprehensively describe the spiciness anomalies and their propagation in the upper North Pacific, with focus on STMW, CMW, and ESTMW. The investigation is based on Argo profiles and is mainly on neutral density (γ) coordinates for preserving water mass structures better than isobaric coordinates. Because temperature and salinity anomalies are density-compensated, we investigate salinity anomalies on γ surfaces as a proxy of spiciness anomalies. The remainder of this chapter is as follows: Section 3.1 shows the climatology of the upper North Pacific and the long-term salinity trends. Section 3.2

describes the temporal evolutions in the three water masses. 3.3 describes the spatial evolutions of spiciness anomalies on their core γ surfaces. 3.4 quantifies the propagation speeds of spiciness anomalies and compares them with the geostrophic currents. 3.5 discussed the origins and causes of the variability. 3.6 summarizes the finding and raise issues for future work.

3.2 Mean state

Before studying the water mass anomalies on neutral density (γ) surfaces, we first looked at the mean distributions of salinity and neutral density in the upper North Pacific during 2004–2018. The vertical distributions of climatology and the standard deviation of salinity are shown in Figure 3.1. A vertical salinity maximum at $\gamma = 23$ – 25 was observed in each region within 5 – 34°N (Figure 3.1 a–c). The maximum within 35 – 44°N was centered at $\gamma = 25$ and only existed west of 170°W . Salinity variations near the vertical salinity maximum were also prominent within 25 – 44°N . Standard deviations of >0.2 were distributed widely up to $\gamma = 26.0$ in the western to the central part of the gyre boundary (35 – 44°N , 140°E to 160°W), where both the salinity and the large variations were found to be uniform vertically. The layers were outcropping in the wintertime; thus, their large standard deviations reflected the large variability on sea surfaces. A maximum of salinity variations was also found centered at 140°W within 25 – 44°N with up to $\gamma = 24.5$. In addition, the above regions with large subsurface salinity variations were found close to the formation and distribution regions of CMW, STMW, and ESTMW.

The spiciness anomalies focused on CMW, STMW and ESTMW were investigated. The criteria for water mass properties are often influenced by different periods or datasets; therefore, we defined the mode waters by their fundamental feature or lateral potential vorticity (Q) minimum (Hanawa and Talley, 2001).

Climatological potential vorticity values on selected γ surfaces are summarized in Figure 3.2. The lateral Q minimum at the northwestern corner of the subtropical gyre was recognizable from $\gamma = 24.70$ with a contour of $Q < 2.5$. The $2 \times 10^{-10} \text{ m}^{-1}\text{s}^{-1}$ was recognizable from $\gamma = 25.00$ and 25.20 . The lowest contour at $Q < 1.5 \times 10^{-10} \text{ m}^{-1}\text{s}^{-1}$ was found at $\gamma = 25.30$, which was centered at 29°N , 150°E . The Q minimum in the STMW spread eastward to the region of CMW was continuous with the increase in γ ; however, the separation of the low Q cores found between STMW and CMW was identified at $\gamma = 25.60$. In the CMW, $Q < 2.00 \times 10^{-10} \text{ m}^{-1}\text{s}^{-1}$ was found at $\gamma = 26.00$. The lowest contour with $Q < 1.75 \times 10^{-10} \text{ m}^{-1}\text{s}^{-1}$ was largest at $\gamma = 26.30$, which was centered at 35°N , 165°W . The Q minimum in the CMW extended southwestward with the

increase in γ and merged with the tropical low Q at $\gamma = 26.50$. This was consistent with the extension of the low Q tongue described by Suga and co-workers (Suga et al., 2004). The ESTMW showed a higher Q than the STMW and CMW. Its Q minimum represented a clear separation with the western value on the 24.40–25.20 γ surfaces. Q values of $< 4.5 \times 10^{-10} \text{ m}^{-1}\text{s}^{-1}$ were found on γ in the range of 24.65–25.15. The lowest contour with $Q < 4 \times 10^{-10} \text{ m}^{-1}\text{s}^{-1}$ was widest at $\gamma = 25.00$ and centered at 25°N , 140°W .

The Q distribution in each month was much noisier; thus, it was difficult to find a continuous and clear boundary in some months. This was when the same Q criteria used by Suga and co-workers for mode water cores (Suga et al., 2004) or that only for summertime (Sugimoto and Hanawa, 2007) were used. In the work of Toyama and Suga (Toyama and Suga, 2010), which also used Argo data to calculate Q, a few of the low Q waters were mixed layer remnants or internal wave fluctuations on isopycnals if we use their methods. To reduce these disturbances and the artificial mixing created by interpolating data in outcropping, we first choose relatively loose Q criteria on each month and γ surface. However, we only used grids that were within the widest low Q contour and excluded the grids outside. We also excluded the grids with depths that were shallower than the MLD. We tested various criteria for Q, γ , latitude, and longitude according to monthly Q distribution maps (not shown here). The most reasonable criteria that define the mode waters in this study are described in In this chapter, observational data sets provided by Argo floats were used to investigate the spiciness anomalies and their propagation in the upper North Pacific during 2004–2018. The temporal and spatial evolutions of the spiciness anomalies were illustrated with a focus on the three mode waters (i.e., STMW, CMW, and ESTMW), which were defined by their density range, location, and low Q limitation (Figure 3.2). The primary results of the study are summarized in Figure 3.18. In general, the spiciness anomalies were generated mostly in the formation regions of the mode waters (i.e., the outcropping region of the isopycnals). The seasonal and year-to-year variations were dampened largely within the upstream part. Meanwhile, the low-frequency variations were preserved downstream. They propagated and decayed in the direction of geostrophic currents. However, some cases showed cross-streamline propagation, and some cases were not caused by mixed layer changes.

A freshening trend in the thermocline of the subtropical gyre at a density range consistent with CMW and NPIW ($\gamma = 25.7\text{--}27$) was observed on a large scale. It was connected to an intense freshening of the surface layer, which was near the northern boundary of the subtropical gyre. It was capped with a salinification trend in a sea surface and a layer corresponding to the NPTW (Figure 3.3). The trend patterns supported the intensification of the hydrological cycle,

which reflected salinity trends in surface layer (i.e., Hosoda et al. (2009) and Durack et al. (2012)). The density and rate of the freshening during 2004–2018 were consistent with the long-term freshening, which ascended to the 1960s (Wong et al., 2001; Nakano et al., 2007; Oka et al., 2017), and were different from those of the rapid freshening of the upper thermocline since the 1990s (Lukas, 2001; Nakano et al., 2015; Nan et al., 2015; Oka et al., 2017).

In the STMW, the salinity was dominated by a quasi-decadal variability with an amplitude of 0.07 (Figure 3.4). On its core surface (25.3γ), the spiciness anomalies appeared initially simultaneously in the STMW formation region and the central latitudes. They were found to spread southwestward to the entire domain of the STMW in 1–2 years. They disappeared finally at the western boundary without spreading northeastward after a direction change in geostrophic currents (Figure 3.4, 7, and 11). The southwestward propagation speed of the spiciness anomalies in the western subtropics was in the range of 0.06–0.09 m/s, almost twice the geostrophic current speed (Figure 3.11), suggesting the transport by eddies. Among isopycnals, the spiciness anomalies were relatively homogeneous in the STMW; however, they showed a delay from 25.00γ to 25.60γ during several months. These differed from the simultaneous decadal salinity variations found among latitudes and isopycnals along the 137°E (Oka et al., 2017).

The interannual and longer variability in the CMW during the Argo period were described for the first time. Salinity in the CMW showed a significant decreasing trend of $-0.004/\text{year}$, which was part of the large-scale freshening of the entire subtropics in the density range that was centered at 26.3γ and quasi-decadal variability that was out of the phase of the STMW (Figure 3.5 and 9). The spiciness anomalies at 26.3γ appeared initially near the western part of the CMW formation region. They spread southward to the majority of the CMW within the subtropical gyre and eastward to the eastern boundary near the boundary between the subtropical and subpolar gyres (Figure 3.9). Their propagation pathway in the subtropical gyre was not strictly along the geostrophic current; however, it was in the inner side of the gyre with a large southward component (Figure 3.12), which was likely caused by eddy transport. While low-frequency signals were propagated from the northern to the southern parts of the CMW with a 2-year delay, the robust year-to-year variations were confined to the northern part and the formation region of the CMW, where strong spiciness fronts existed (Figure 3.5, 9, and 12). These were likely due to a double-diffusion related to the modification of the TRMW. In addition, L-CMW ($\gamma < 26.20$) and D-CMW ($\gamma > 26.20$), which have different formation regions, showed different year-to-year variations in a number of years.

In the ESTMW, the salinity values with a total time-scale of 3–4 years (Figure 3.6) showed larger seasonal and year-to-year variations than the other water masses. The spiciness anomalies appeared initially near its formation region and propagated clockwise in a direction and velocity that were consistent with the geostrophic currents. They finally arrived at the western boundary in the western tropics (Figure 3.8 and 10). The transport times across the domain of the ESTMW for the spiciness anomalies were within 1 year, which was shorter than the other water masses considered. Among different isopycnals, the spiciness anomalies between the light part ($\gamma < 24.85$) and dense part ($\gamma > 24.85$) of the ESTMW showed different year-to-year variations without a steady lag; however, the ranges found in their raw salinity were uniform (Figure 3.4c, 5c, and 6c).

Furthermore, we discussed the origins of the spiciness anomalies in the thermocline. In the western to central subtropics, the interannual spiciness anomalies in the thermocline were synchronized with the meridional shift of the outcrop lines of the isopycnals and the consequent interannual salinity anomalies in the mixed layer near the outcrop line - (negative salinity anomalies with further north outcrop line), with a lag of no longer than one year (Figure 3.13 and 14). Our results indicated that the spiciness anomalies observed in STMW and CMW were generated mainly in and subducted from the western to central parts of their outcropping region. It was consistent with some previous findings (Yan et al., 2017; Oka et al., 2019) and rejected the pathway the eastern subtropics-tropics to the western subtropics as supported by other results (Zhang and Liu, 1999; Ogata and Nonaka, 2020).

Meanwhile, in eastern subtropics, a few interannual signals appeared in the thermocline without a corresponding earlier occurrence in the mixed layer (Figure 3.13 and 14). These signals intensified after leaving the outcrop line (Figure 3.10 and 13). Notably, spiciness anomalies in the thermocline that corresponded to the meridional shifts of the outcrop line and the accompanying mixed layer salinity anomalies were found only near the center of ESTMW formation region. This implied the limited contribution of the mixed layer salinity variations in the generation of the spiciness anomalies in the eastern subtropics. It also provided new evidence for the contributions of spice injection after the work of Katsura (Katsura, 2018).

The main subject of this chapter was the spiciness anomalies that were subducted to the thermocline; therefore, we provided concise explanations of the generation mechanisms involved. However, there are several issues that remain to be explained. For example, we found that the propagation speeds of the spiciness anomalies were faster than the geostrophic current in western subtropics. In addition, the spread of the spiciness anomalies was inclined to the

inner side of the relevant streamlines and linked with eddy effects. Furthermore, the relationship between the salinity changes and the climate modes was interesting to discuss.

Table 3.1. The distributions of the detected mode waters were generally consistent with previous descriptions.

3.3 Temporal variations of salinity

3.3.1 Linear trend

The linear trends in salinity during 2004–2018 (Figure 3.3) were obtained by the least-squares method, with a modified Mann-Kendall test (Hamed and Rao, 1998) of significance on the 95% level. The most striking feature found was the significant large-scale freshening trend in the subsurfaces of subtropics on both isobars and isopycnals at 25.5–26.6 γ (about 200–500 dbar) west of 150°W and within 15–24°N. The trend was at 25.6–26.8 γ (350–450 dbar) on all longitudes; however, the separation was near 140°W and within 25–34°N. The magnitude was stronger than $-0.002/\text{year}$. The distribution of the subtropical freshening trend was deeper and thicker in the west than east and higher latitude than lower latitude on isobars. This corresponded to the distribution of γ surfaces, which supported the advantage of investigating salinity anomalies on γ instead of pressure coordinates. The subsurface freshening trend was connected to the mixed layer at 35–44°N in the central longitudes (150°E to 150°W), which is also an outcrop region of the isopycnals with much stronger signals. This suggested subsurface freshening in the subtropics that resulted from the subducted surface freshening in higher latitudes.

The density range of the freshening encompassed the full range of the CMW and the lighter part of the salinity minimum in the subtropics (Figure 3.1b–1c), i.e., the North Pacific Intermediate Water (NPIW) (Talley, 1993). The density range of the freshening was consistent with that which can be traced back to the 1960s detected along hydrographic sections, which have σ_θ values in the range of 25.5–27.0 along the 137°E north of 10°N during 1967–2016 (Oka et al., 2017), between the main thermocline and NPIW north of 15°N along the 137°E during 1967–2005 (Nakano et al., 2007), and in the NPIW along the 24°N during the 1960s to 1985 (Wong et al., 2001). However, previous results with more recent starting time have suggested a lighter range in the significant freshening with σ_θ values of 25.0–26.0 near the Hawaii Ocean Time Series station (22°N, 158°W) during 1988–2001 (Lukas, 2001), σ_θ values of 25.0–26.0 along the 24°N that were comparison between historical and Argo data of 2003–2006 (Ren and Riser, 2010), σ_θ values of 25.0–26.2 along the 137°E north of 12°N during 1997–2016 (Oka et al., 2017), and from the sea surface to the subsurface salinity maximum along the 137°E during 1992–2009 (Nan et al., 2015). Thus, there was a long-term freshening of the entire thermocline

in the subtropics during 2004–2018 and possibly dating back to the 1960s. However, the rapid freshening of the upper thermocline, possibly since the 1990s, likely underwent a hiatus from 2004 to 2018.

In the western to the central longitudes at $\gamma < 25$ ($p < 150$ dbar) within 5–24°N (Figure 3.3 a and b) and near the eastern boundary at $\gamma < 25.5$ ($p < 150$ dbar) within 25–44°N (Figure 3.3 c and d), a salinification trend that extended from the mixed layer to the upper thermocline was found over the subsurface freshening. The former coincided with the salinity maxima, i.e., the NPTW (Figure 3.1) (Cannon, 1966). The latter encompassed the northeastern part of the ESTMW. Previous studies have investigated the NPTW using hydrographic data that were mainly along 137°E and revealed that the salinity of the NPTW increased after the 1976/77 regime shift and decreased with decadal variations thereafter (Suga et al., 2000; Nakano et al., 2015; Nan et al., 2015; Oka et al., 2017). The recent increase in salinity during 1997–2016 was recently reported (Oka et al., 2017). The area with an amplitude that was stronger than 0.008/year occupied a large part of the salinification region. Under the freshening layer, there was also a positive but weak salinity trend in the 5–34°N.

The above patterns in salinity trends that were derived from a recent and short period (2004–2018) were consistent with the long-term global trend in salinity patterns, which were observed in earlier and longer periods in surface layer (i.e., 1950–2010 (Skirris et al. 2014), 1950–2000 (Durack et al., 2012), and 1960–2007 (Hosoda et al., 2009)) and near the upper-ocean salinity maximum and the intermediate salinity minimum (1970–2005 (Helm et al., 2010)). The upper-ocean salinity maximum layer and the sea surface of its outcrop region in the subtropics, where evaporation dominates precipitation, became saltier. Meanwhile, the intermediate salinity minimum and the sea surface of its outcrop region in high latitudes, where precipitation dominates evaporation, became fresher. This may be related to the enhancement of the hydrological cycle (Allen and Ingram, 2002; Held and Soden, 2006), but we still need further investigation on the effects of warming/cooling and heating to examine it.

3.3.2 STMW

Salinity in the STMW was dominated by a quasi-decadal variability. Its seasonal variability was smaller compared to interannual or longer variability (Figure 3.4a). The peak and trough of the STMW salinity were in 2006 and 2010 with a difference of ~ 0.1 , which was consistent with the clear freshening of the STMW during 2009–2010 (Sugimoto et al., 2013) and freshening of the northwestern Pacific at $\sigma_\theta = 24.5$ – 25.4 during 2003–2012 (Yan et al., 2017). The linear trend observed during 2004–2018 was -0.002 /year and failed the 95% significance test. This trend was consistent with that found during 1967–2016 along the 137°E

section (Oka et al., 2017) and weaker than that found during 1997–2016 ($-0.005/\text{year}$) (Oka et al., 2017) and 1987–2012 ($-0.004/\text{year}$) (Nan et al., 2015) along the same section. Although it was difficult to separate the decadal variability from the peak to trough and the freshening trend in the considered 15-year period, the value of the linear trend obtained was in favor of a long-term weak freshening that was superimposed on decadal variability. This was in contrast to the more recent rapid freshening observed in previous studies. In addition, in the vertical diagram of salinity trends (Figure 3.3), the freshening in the density range of the STMW was not significant and lighter than the density range of significant freshening.

Compared to the northern and middle parts, the salinity in the southern part of the STMW showed smaller seasonal variations (Figure 3.4b), a smaller amplitude of the decadal cycle, and a delay of several months. These results suggested an STMW spreading away from its formation region by the subtropical gyre (Bingham, 1992). In addition, the spiciness anomalies were spread and dampened at the same time. Similar dampening of seasonal variations and delay of signals from the northern to the southern sides were also found in the CMW (Figure 3.5b) and ESTMW (Figure 3.6b); however, their consistencies were not as good as in the STMW.

Vertically in the STMW, we found a delay in salinity anomalies from light to dense surfaces. The bottom in 2010 and 2011 was at $\gamma = 25.00\text{--}20.05$ and $\gamma = 25.50\text{--}25.60$, respectively (Figure 3.4c). Denser isopycnals outcrop further north, subduct to deeper depths, and show slower geostrophic currents (data not shown); thus, the signals need more time to fill the corresponding portion of the STMW.

3.3.3 CMW

In the CMW, the salinity showed a 95% significant freshening trend of $-0.004/\text{year}$ during 2004–2018 (Figure 3.5a). The salinity decreased since 2005 and reached the bottom in 2012. It increased to a second peak in 2014 and then decreased rapidly since 2015. These show an overall quasi-decadal cycle with a smaller amplitude and earlier phase compared to the STMW. This decadal variability has been detected by hydrographic data along 180° during the 1988/1989 climate shift (Suga et al., 2003) and along 137° during 1967–1996 (Oka et al., 2017). However, it has not been reported after the 2000s. The freshening was also consistent with the freshening at $\sigma_\theta = 26.0$ and 26.4 along 137° during 1996–2016 (Oka et al., 2017).

While the middle and southern parts of the CMW ($27\text{--}36^\circ\text{N}$) were essentially homogeneous on both salinity and salinity changes with a 1-year lag, the northern part that was also in the formation region of the CMW ($37\text{--}39^\circ\text{N}$) showed a much lower salinity (i.e., 0.05

and 0.15 lower in 32–36°N and 40–41°N, respectively compared to the middle to southern parts). This part also showed much larger seasonal variations and more significant year-to-year variations, which obscured its decadal variability (Figure 3.5b). These were because of the strong climatological salinity gradients that existed north of 39°N. The interannual variations on the northern side were preserved up to the southern side with a total delay of about 2 years. The year-to-year variations were dampened significantly; thus, the decadal variability and trend were more significant. For example, the salinity increased at >0.06 and peaked in 2009 within 40–41°N. It increased by 0.02 within 37–39°N and was flat during 2009–2010 within 32–36°N. These will be discussed in section 0.

The salinity in the CMW showed a similar trend on each surface; however, the interannual variations showed differences between the light ($\gamma = 26.00\text{--}26.15$) and dense ($\gamma = 26.20\text{--}26.45$) layers, for example, in 2012 (Figure 3.5c). The inconsistency in interannual variations corresponded to the different formation regions and circulation pathways in the light part (L-CMW) and the dense part (D-CMW) of the CMW. The L-CMW is formed between the KE front and the Kuroshio bifurcation front (KBF) and distributed along the inner part of the eastern subtropical gyre. The D-CMW is formed between the KBF and the subarctic frontal zone (SAFZ) and distributed in the outer part (Oka and Suga, 2005; Oka et al., 2011; Oka et al., 2020).

3.3.4 ESTMW

In the ESTMW, a significant trend in the salinity was not observed; however, it showed much larger seasonal and year-to-year variations compared to the STMW and the CMW (Figure 3.6a). The entire ESTMW showed a 3–4-year variability with higher-frequency variations on a time scale of 1–2 years, which smoothed gradually from the northern part (near its formation region) to the middle and the southern parts (Figure 3.6b). The delay observed from the northern part (27–31°N) to the southern part (17–21°N) is within one year. Although previous studies have suggested decadal variability in density and volume of the ESTMW (Ladd and Thompson, 2000; Guo et al., 2018), decadal variability was not found in the ESTMW salinity. This suggested dynamic changes during the ESTMW formation, which likely have limited effects on the spiciness anomalies in the distribution region of the ESTMW. In the ESTMW, the northeastern part showed a significant positive salinity trend (Figure 3.3 and Section 3.3.1); however, significant trends were not observed in its other parts or total salinity.

The salinity values that decreased with an increase in the density and the prominent vertical delay of salinity anomalies from light to dense surfaces, which were observed in STMW and the CMW, were not found in ESTMW. Besides, the salinity changes in the ESTMW were similar among the different isopycnals in most years. This was except in years with a vast year-to-year variation (i.e., 2009–2011 and 2014), during which the light ($\gamma = 24.65\text{--}24.80$) and dense ($\gamma = 24.85\text{--}25.15$) parts showed different changes. These features among different γ surfaces in the ESTMW corresponded to the weak stratification (Hautala and Roemmich, 1998) and the strong vertical mixing due to salt-finger convection (Sugimoto and Hanawa, 2007; Toyama and Suga, 2010).

3.4 Spatial patterns of spiciness anomalies

The annual mean spiciness anomalies on the core surfaces of the STMW ($\gamma = 25.3$), ESTMW ($\gamma = 25.0$), and CMW ($\gamma = 26.3$) are shown in Figure 3.7, Figure 3.8, and Figure 3.9, respectively. In addition, we calculated the anomalies in the entire γ range of each water mass and weighted the values by thickness. Their amplitudes and spatial patterns were consistent with the core γ surfaces only. Therefore, we investigated the propagation of spiciness anomalies on the core γ surfaces of the mode waters.

Around the region of the STMW (Figure 3.7), positive (negative) spiciness anomalies >0.004 (<-0.004) appeared initially in 2004 (2009) near the outcrop line ($30\text{--}35^\circ\text{N}$) in both the $140\text{--}150^\circ\text{E}$ and the central latitudes ($160^\circ\text{E}\text{--}160^\circ\text{W}$). The former was in the STMW formation area, while the latter was beyond the eastern boundary of the STMW formation area, which was 175°E (Oka and Suga, 2003), and beyond the low Q boundary in the monthly PV maps (not shown). The anomalies were found to spread southwestward to the entire domain of the STMW in 2005–2006 (2010–2012). They then weakened gradually in the same direction from northeast to southwest sides during 2007–2009 (2012–2015). At the end of the data period, new positive anomalies appeared in 2016, which were found to spread to the entire STMW region in 2018. The path of southwestward propagation of the anomalies was generally consistent with the streamlines in the region (Figure 3.2); however, it was closer to the inner part of the streamlines, which suggested cross-streamline spreading.

In the ESTMW (Figure 3.8), the spiciness anomaly in each positive or negative period appeared initially at $150\text{--}130^\circ\text{W}$ near the outcrop line ($30\text{--}40^\circ\text{N}$). This was near the ESTMW formation region, which is slightly further north than it. The anomalies spread initially

clockwise to the domain of the ESTMW in 1–2 years and then southwestward to the dateline in the subtropics. They finally arrived at the western boundary of the tropics. The propagation path was consistent with the direction of geostrophic streamlines (Figure 3.2) and similar to those detected by Sasaki and co-workers (Sasaki et al., 2010) and Katsura (Katsura, 2018) during 2004–2008 and 2005–2013, respectively. The rapid signal change near the outcrop line and the continuous propagation of signals caused the meridional contrasts of positive and negative anomalies in the eastern side of the subtropical gyre (Figure 3.8).

On the surface $\sigma_t = 26.3$ (Figure 3.9) during 2004–2018, the entire North Pacific subtropical gyre experienced a freshening from 2004–2018, especially in the distribution region of the CMW. The anomalies were found to be most intensive near the boundary of subtropical and subpolar gyres, which were accompanied by a strong salinity frontal structure that determines the distribution of the CMW (Oka and Suga, 2005). The negative salinity anomalies (i.e., < -0.06) appeared initially at 155°E and 37°N in 2014, as shown in Figure 3.9. These were around the western part of the CMW formation region (Oka and Suga, 2005). They spread southward within the subtropical gyre to the majority of CMW and eastward along the North Pacific current to the northeastern corner, where they mixed with positive anomalies during 2015–2018. The two propagation pathways were also found in the positive period. The northern pathway was also suggested by Taguchi and Schneider (2014) and Kouketsu et al. (2017). Unlike the anomalies in the STMW with cores that migrated downstream along the spreading path (Figure 3.7), the upstream part of the CMW remained as the core of the anomalies. This might imply the importance of eddy transports in the propagation of anomalies. Another possible implication is that the long-term changes in forcing were more effective in generating anomalies than the variability of the STMW.

The separation of CMW and Transition Region Mode Water (TRMW) (Saito et al., 2007, 2011) was not conducted here. The TRMW in a density range of $26.3\text{--}26.6 \sigma_\theta$ typically shows fresher and colder properties (salinity < 34.0) than the CMW. The modification of a part of the TRMW into D-CMW associated with double-diffusion salt-finger convection has been suggested (Saito et al., 2011; Suga et al., 2013). This process occurs in a favorable condition due to geostrophic shear with a density-compensating temperature-salinity front. At $40\text{--}41^\circ\text{N}$, the salinity decreased to < 33.95 in 2017 (Figure 3.5b), and an isopycnal salinity front existed (Figure 3.9); thus, the water in the area may also consist of TRMW. To examine the potential for double-diffusion, we calculated the Turner angle (Tu) (Ruddick, 1983). Double-diffusion

becomes active when the $Tu > 71.6^\circ$ (Johnson, 2006). At $\gamma = 26.3\text{--}26.5$ along 40°N east of Japan, which coincides with the location of the TRMW, the Tu showed a value $> 71.6^\circ$ from February to April, indicating an active salt-finger double-diffusion (calculation and figures are described in the Supplementary Material). Therefore, the modification processes of the TRMW likely contributed to the year-to-year variations that were prominent on the northern side and very weak on the southern side of the CMW. A few spiciness anomalies were generated and diffused near the spiciness fronts without propagating downstream.

3.5 Propagation direction and velocity of spiciness anomalies

The propagation directions of salinity anomalies in Figure 3.7–3.9 were generally consistent with the geostrophic currents; therefore, we traced the anomalies on the core γ surfaces of the mode waters along the mean streamlines that pass through the distribution regions. A comparison of the propagation speeds with the advection of the mean flow is shown in Figure 3.10–3.12. Along a streamline, seasonal variations dominated upstream and near the outcrop line; however, most of the signals attenuated quickly in the south of the outcrop line. Low-frequency signals dominated the downstream regions, which was consistent with the spatial differences found in the salinity time series (Figure 3.4–3.6). The low-frequency signals were found to propagate and decay at the same time.

Along the streamline that passes through the ESTMW (Figure 3.10), the detected low-frequency signals were found to change phase every 3 years south of the outcrop line (points 0–2 in Figure 3.10) during 2004–2018. Almost all the low-frequency signals were propagated from the outcrop line near 30°N and 140°W until they reached the western boundary near 10°N . The propagation speed of spiciness anomalies accelerated from ~ 0.02 m/s in the eastern subtropics to ~ 0.12 m/s in the western tropics, which was consistent with the mean geostrophic velocity. This was similar to the observations in previous studies (Sasaki et al., 2010; Kolodziejczyk and Gaillard, 2012; Katsura, 2018). The amplitudes of low-frequency anomalies decayed rapidly along the streamlines, especially after passing through the south of Hawaii (see point 4 in Figure 3.10).

The low-frequency signal that did not reach the western boundary was only the negative signal that appeared initially during 2008–2009 (Figure 3.10). This signal was intruded by the positive signals and almost disappeared in the south of Hawaii in 2012. From the slope of the continuous anomalies in Figure 3.10 b, the intrusion might be a branch of the former positive signal, which propagated slower than the geostrophic current with a slope larger than the mean

advection line. It could also be a branch of the latter positive signal that propagated faster than the geostrophic current with a slope smaller than the mean advection line.

Along the streamline that passed through the STMW (Figure 3.11), continuous downstream propagations were observed only in the southwestward part of the streamline (points 1–6). Unlike the good agreement found between spiciness anomalies' propagation speed and the mean geostrophic velocity in the eastern subtropics, the propagation speed of spiciness anomalies in the western subtropics was much faster than the geostrophic current. Calculating from the strongest amplitudes of signals that were propagated from the easternmost to the westernmost points (distance of 0.5–3.5 Mm) in ~1.5 years, the propagation speed of spiciness anomalies was about 0.06–0.07 m/s. Meanwhile, the mean geostrophic speed was only approximately 0.03 m/s. When we investigated the neighboring streamlines and streamlines on adjacent isopycnals, the transit time of spiciness anomalies from the outcrop lines to the southmost STMW was 1–2 years with a speed of 0.06–0.09 m/s.

After the streamline turned northeastward, the low-frequency anomalies fragmented and could not propagate downstream (Figure 3.11). The spiciness anomalies propagated from point 5 to point 4. The anomalies between points 5 and 0 were simultaneous, despite the large eastward geostrophic speed. These results imply that the spiciness anomalies were generated simultaneously near the outcrop line in the wide range of the STMW formation area. They propagated southwestward and finally disappeared near the western boundary. The fact that the signals propagated at a higher speed than the geostrophic current in the southwestward part of the gyre and southwestward in the northeastward part of the gyre suggested that the spiciness anomalies in the western subtropics were propagated by both the geostrophic current and other processes (e.g., eddies). Using an eddy-resolving model, Nishikawa and co-workers (Nishikawa et al., 2010) revealed the southward eddy thickness transport in the STMW core density. However, since the resolution of the Argo was not sufficient for mesoscale and sub-mesoscale eddies, we did not investigate the contributions of eddies on the transport spiciness anomalies.

Along the streamline that passed through the CMW domain at the $\gamma = 26.3$ surface (Figure 3.12b), the spiciness anomalies were not propagated from the upstream to the end. However, we observed the propagation of strong signals in some parts. For example, the center of the strongest positive anomaly propagated from 165°E (point 2) to 165°W (point 5) during 2004–2009. The anomaly then turned gradually negative, and the resulting negative anomaly propagated from the 170°E (point 8) to the western boundary (point 13) during 2014–2018. The time when the anomaly turned to negative was not a monotonic increase downstream, which is 2010, the end of 2012, and the beginning of 2012 at 165°E (point 2), 180° (point 6), and 170°E

(point 8), which suggested that the spread of the freshening anomaly did not follow the downstream direction of the mean flow. The above positions were far from the outcrop line, and the freshening in 2011–2013 in this region occurred only under the mixed layer (Figure 3.13d); thus, the extension of negative anomalies among points 5–8 in 2012 was not caused by local outcropping. On the other hand, the long-term trend of CMW salinity and mixed layer salinity in the CMW formation region (Figure 3.5 and Figure 3.14) showed good agreement; therefore, we considered that the salinity anomalies were still propagated from the outcrop to the downstream regions along a pathway that was different from the mean flow. Using the XCTD section data in 2001, it has been suggested that a part of the D-CMW was transported southward across the eastward mean flow by mesoscale eddies and then spread along the subtropical gyre (Suga et al., 2013). Inspired by this idea, we hypothesized the existence of a large southward transport by eddies at speed much faster than the quasi-zonal geostrophic current; thus, the overall transport of a spiciness anomaly is in the inner side of a streamline. Therefore, the synchronized occurrence of freshening among points 6–9 was affected due to the anomalies far northwest (points 2–3), which were brought via eddy transports.

Meanwhile, the anomalies advected from the points just upstream by the geostrophic current were also likely to affect the changes in the eastern part (points 6–7). This was supported by the spatial patterns found in Figure 3.9. As a result, we were able to observe the propagation of anomalies along the streamline and the different occurrence times of freshening that were not consistent with the streamline simultaneously. Further studies using an eddy-resolving dataset are needed to examine our hypothesis.

The streamline at the gyre margin at $\sigma = 26.3$ surface was also investigated. Salinity was dominated by the high-frequency seasonal variations in the western side (points 0–2) that were close to the outcrop line, both seasonal and interannual variations in the middle portion (points 2–4), and the low-frequency anomalies across the date line (point 4). The eastward propagation of the low-frequency anomalies was consistent with that suggested in a previous report (Taguchi et al., 2017), which was based on historical observations and the ocean general circulation model (OGCM). The boundary where seasonal variations played a dominant role varied significantly in different years. This was consistent with the significant changes in outcrop line positions in $160^{\circ}\text{E}\sim 180^{\circ}$, as shown in Figure 3.9, and related to the changes in the CMW formation region. The high-frequency variations that extended to point 4 were likely a result of strong eddy activities in the central North Pacific near the gyre margin and in favor of the eddy-induced southward transport to the downstream part of the CMW.

3.6 Possible origins of spiciness anomalies

3.6.1 Vertical structure of the spiciness anomalies

Besides the horizontal patterns on each isopycnals, it is also instructive to observe the vertical structures during the occurrence of the spiciness anomalies. The γ -time diagram of interannual salinity anomalies was averaged in the formation and the downstream distribution regions of the STMW, CMW, and ESTMW. The results are presented in Figure 3.13.

In formation regions of the STMW and the CMW (Figure 3.13a and 13c), the strong anomalies under the MLD of up to $\gamma = 26.8$ were found to be connected to anomalies found in the mixed layer. However, some variations that lasted no more than 1 year were confined in the mixed layer. Therefore, the anomalies subducted into the thermocline showed a lower frequency. The low-frequency anomalies were preserved and further smoothed in the downstream distribution regions of both STMW and CMW (Figure 3.13b and 13d). The above behaviors were consistent with the dampening of seasonal and year-to-year salinity variations from the northern to the southern sides of both STMW and CMW (Figure 3.4b and 5b).

During the large-scale freshening period, the migration of the core surfaces of the anomalies found in the STMW and CMW distribution regions was in accordance from $\gamma < 25.0$ before 2009 to $\gamma = 25.5$ in 2012 and finally at $\gamma = 26.0$ – 26.5 since 2015 (Figure 3.13b and 13d). The migration of the signal coincided with the delay from the light to the dense layers, as shown in the STMW time series (Figure 3.4c). The occurrence time of the anomalies showed no vertical delay in both the STMW and the CMW formation regions (Figure 3.13a and 13c); thus, the vertical migration of an anomaly core in the distribution regions can be explained by the further north outcropping position, the accompanying longer subduction path of denser isopycnals (Figure 3.7–3.9), and a decrease in the geostrophic speed with depth. Its synchronization between STMW and CMW suggested sharing common causes on decadal to longer time scales in the salinity anomalies found in both STMW and CMW. Meanwhile, the interannual variations in the CMW were also influenced by other processes in the mixed layer of the formation region.

However, the connections between the thermocline and the mixed layer anomalies in mode water formation regions and the vertical delay in mode water distribution regions did not apply to the eastern subtropics. Instead, almost in the same year, spiciness anomalies in the ESTMW

distribution region appeared at $\gamma = 24.5\text{--}26.0$, with the strongest signals at $\gamma = 25.0\text{--}25.5$. In the ESTMW formation region at $\gamma = 25.0\text{--}26.0$ (Figure 3.13e), a positive anomaly during 2005–2007 or a negative anomaly during 2012–2014 was not found in the earlier mixed layer. Another positive anomaly occurred at the mixed layer and $\gamma = 26.0\text{--}26.5$ isopycnals almost the same time during 2015–2017, which suggested sources of anomalies other than outcropping. Coincidentally, the above three anomalies were intensified downstream after leaving the outcrop line during 2005–2007, 2013–2015, and 2016–2018 on the distance-time diagram along $\gamma = 25.3$ isopycnal (Figure 3.10). An intensification of the anomalies was also observed widely at $\gamma = 25.0\text{--}25.7$ in the ESTMW distribution region (Figure 3.13f) during 2006–2007, 2014–2015, and 2017–2018. The former two cases of downstream intensification were consistent with a study at $\sigma_\theta = 25.0\text{--}25.2$ near the ESTMW formation region (Katsura, 2018). These were explained by the subsurface spice injection that occurred at the base of the ESTMW. In our Tu maps (see Supplementary Material), Tu values $>71.6^\circ$ were distributed widely in $150\text{--}135^\circ\text{W}$, $23\text{--}30^\circ\text{N}$ at $\gamma = 25.2\text{--}25.3$, which was at the base of the ESTMW from March to May and found during February to September, indicating a salt-finger double-diffusive convection during the formation and dissipation periods of the ESTMW. Considering the similar behaviors found among the three cases, the new positive anomaly that occurred near the outcrop line in 2016 and intensified downstream during 2017–2018 was likely due to the salt-finger double-diffusion.

3.6.2 Meridional shift of the outcrop line

The spiciness anomalies in the thermocline were connected to the mixed layer in most cases, especially in the western to central subtropics; therefore, we looked at the changes in the mixed layer near the outcrop line. Modeling studies indicated that a meridional shift of the outcrop line determined the spiciness variability in the western North Pacific at $\sigma_\theta = 25.4$, i.e., warm-salty (cold-fresh) anomalies with a distinct equatorward (poleward) shift (Nonaka and Sasaki, 2007; Ogata and Nonaka, 2020). We examined the influence of the meridional shift of outcrop line on the spiciness anomalies in the observations and the application of the shift mechanism in the central and eastern North Pacific. The latitudes of the late winter outcrop line, the salinity anomalies in the mixed layer along the winter outcrop line, and the late winter MLD are shown in Figure 3.14.

In the formation region of the STMW (outcrop line of $\gamma = 25.3$ in $140\text{--}60^\circ\text{E}$ shown in Figure 3.14a), the outcrop line position was in the northmost (southmost) during 2009–2011 (2005 and 2017). The mixed layer salinity along the outcrop line was dominated by negative (positive) anomalies, which were synchronized with the negative (positive) spiciness anomalies

in the STMW distribution region at $\gamma = 25.3$ during the same period (Figure 3.7). The peaks and bottoms in the weight-averaged salinity time series in the STMW below the MLD (Figure 3.4) were also consistent with the above variations with a delay of 1 year. Meanwhile, the late winter MLD along the outcrop line also correlated with the salinity anomalies but was not as good as the latitudinal position. A deeper (shallower) MLD was accompanied by an increasing (decreasing) of the spiciness anomalies in STMW in 2005, 2011, and 2017 (2006 and 2008) (Figure 3.4), but this was not applicable in 2016. However, the changes in MLD did not show a clear relationship with the salinity anomalies in the mixed layer, suggesting that the deepening (shoaling) of the MLD influenced the STMW salinity most likely through dynamic mechanisms.

While a study (Ogata and Nonaka, 2020) explained the spiciness anomalies in the western North Pacific by the meridional shift of outcrop line around the central-eastern North Pacific, we found that the anomalies were more consistent with the meridional shift of outcrop line and the accompanying mixed layer anomalies in the western North Pacific (Figure 3.14b–14c). They were also not synchronized with the anomalies in the eastern North Pacific.

To further investigate whether the signals in the northeastern Pacific propagated to the western subtropics, we checked the time-longitude diagram of salinity anomalies at $\gamma = 25.3$ that were averaged in 25–30°N (Figure 3.15). The continuous westward propagation of salinity anomalies from 160°W to 145°N during 1998–2001 based on OGCM (Figure 9 in Ogata and Nonaka, 2020) is not shown here. Instead, we observed different propagations between the eastern and the western sides. The positive (negative) anomalies that originated at 130°W in 2006 (2009) propagated westward up to 180° in 2010 (2013) and did not spread to the west. Meanwhile, the anomalies in the western subtropics showed consecutive propagation at a small amplitude back to 170°E in 2009. However, the anomalies that originated around 170°W in 2012 and 2014 showed consecutive eastward propagation at a high amplitude to the eastern boundary. The results supported that the salinity anomalies in the western subtropics were generated mainly in the northwestern subtropics rather than the eastern subtropics. This was in agreement with the origin and pathway suggested by other groups (Yan et al., 2017; Oka et al., 2019).

In the annual mean maps of spiciness anomalies at $\gamma = 25.3$ shown in Figure 3.7, the anomalies appeared initially at the same time in the center of the STMW formation region and 160°E to 160°W near the outcrop line. It was most likely explained by the large-scale and simultaneous changes that occurred in the entire outcropping region. This was supported by the synchronized vertical migration of low-frequency signals between the western and the central subtropics (Figure 3.13b and 13d). The above results discorded the continuous propagation

from 30°N, 160°W to the western subtropics, which were shown in previous experiments (Ogata and Nonaka, 2020). In addition, the results were not in agreement with the “subtropical pathway” of anomalies, which originated in the eastern subtropics to the tropics and propagated westward in the subtropics and then northeastward along the Kuroshio path toward the midlatitudes, raised by another study (Zhang and Liu, 1999). Since the zonal propagation of the anomalies around the central to eastern latitudes showed different directions in different years (see Supplementary Material Figure 3), further work is needed to clarify whether the disagreement of propagation path was caused by models or different events in different years.

We also investigated the influences of the meridional shifts of outcrop line in the CMW and ESTMW (Figure 3.14 b and c). They were applicable to the CMW only. In the CMW formation region, the further south outcrop line, which was accompanied by a large mixed layer salinity along the line, was observed during the early years (i.e., 2005–2006 and 2008–2010). The further north outcrop line, which was accompanied by a small mixed layer salinity, was observed in the second half of the data period (i.e., 2011, 2014–2015, and 2017). This was consistent with the significant freshening trend of CMW salinity (Figure 3.5). In addition, the further north outcrop line and fresher mixed layer in 2007 and 2011 caused the interannual variations observed in the northern part of the CMW (Figure 3.5b and Figure 3.9).

The above relationship was not applicable in the ESTMW. During 2004–2005 and 2014–2015 (2007, 2013, and 2017–2018), the outcrop line at $\sigma = 25.0$ in the ESTMW formation region (150–130°W) shifted poleward (equatorward). The mixed layer salinity along the line was dominated by negative (positive) anomalies; however, the corresponding salinity variations were not found in the subducted ESTMW (Figure 3.6). Synchronized significant anomalies were detected at $\sigma = 25.0$ only near the center of the ESTMW formation region (30°N, 140°W) and were not found in 2005 (2017) (Figure 3.8). The above results, combined with limited connections of anomalies between the mixed layer and the denser isopycnals in the ESTMW (Figure 3.13), suggested that the outcrop line shift and the accompanying salinity anomalies in the mixed layer in eastern subtropics only influenced the near center of the ESTMW formation region. Meanwhile, the spiciness anomalies in the downstream region and the denser layers were caused by other processes such as spice injection. The limited influence of the mixed layer on spiciness anomalies in the ESTMW than both the STMW and CMW was related to the distinct vertical structure in the ESTMW. The water was cooler and fresher below the ESTMW, which caused the rapid dissipation of the ESTMW through a salt-finger type convection (Sugimoto and Hanawa, 2007; Toyama and Suga, 2010).

3.6.3 Double-diffusion

In order to examine whether the vertical structures at the mode waters have the potential for double-diffusive convection, Turner angle (Turner, 1973; Ruddick, 1983) was calculated according to equation (5). When Turner Angle exceeds 71.6° , double diffusive convection becomes active (Schmitt, 1981; Johnson, 2006).

On $\gamma = 26.3-26.5$ along 40°N east of Japan, coinciding with the location of TRMW, Tu shows a value larger than 71.6° from February to April (Figure 3.16), indicating active salt-finger double-diffusion. Therefore, the year-to-year variations that are prominent on the northern side of CMW but are very weak on the southern side of CMW are possibly explained by modification processes of TRMW, i.e., some of the spiciness anomalies are generated and diffused near the spiciness fronts, without propagating downstream.

In our Tu maps, $Tu > 71.6^\circ$ is widely distributed in $150-135^\circ\text{W}$, $23-30^\circ\text{N}$ on $\gamma = 25.2-25.3$, which is at the base of ESTMW, from March to May, and is recognizable during February to September, indicating salt-finger double-diffusive convection during the formation and dissipation periods of ESTMW. Considering similar behaviors between the three cases, the new positive anomaly which occurred near the outcrop line in 2016 and intensified downstream during 2017-2018 may also be explained by salt-finger double-diffusion. However, we did not estimate the effects of horizontal mixing. So, further work is needed to give a quantitative description of the contributions of the double-diffusion and the horizontal mixing.

3.7 Summary and discussions

In this chapter, observational data sets provided by Argo floats were used to investigate the spiciness anomalies and their propagation in the upper North Pacific during 2004–2018. The temporal and spatial evolutions of the spiciness anomalies were illustrated with a focus on the three mode waters (i.e., STMW, CMW, and ESTMW), which were defined by their density range, location, and low Q limitation (Figure 3.2). The primary results of the study are summarized in Figure 3.18. In general, the spiciness anomalies were generated mostly in the formation regions of the mode waters (i.e., the outcropping region of the isopycnals). The seasonal and year-to-year variations were dampened largely within the upstream part. Meanwhile, the low-frequency variations were preserved downstream. They propagated and decayed in the direction of geostrophic currents. However, some cases showed cross-streamline propagation, and some cases were not caused by mixed layer changes.

A freshening trend in the thermocline of the subtropical gyre at a density range consistent with CMW and NPIW ($\gamma = 25.7\text{--}27$) was observed on a large scale. It was connected to an intense freshening of the surface layer, which was near the northern boundary of the subtropical gyre. It was capped with a salinification trend in a sea surface and a layer corresponding to the NPTW (Figure 3.3). The trend patterns supported the intensification of the hydrological cycle, which reflected salinity trends in surface layer (i.e., Hosoda et al. (2009) and Durack et al. (2012)). The density and rate of the freshening during 2004–2018 were consistent with the long-term freshening, which ascended to the 1960s (Wong et al., 2001; Nakano et al., 2007; Oka et al., 2017), and were different from those of the rapid freshening of the upper thermocline since the 1990s (Lukas, 2001; Nakano et al., 2015; Nan et al., 2015; Oka et al., 2017).

In the STMW, the salinity was dominated by a quasi-decadal variability with an amplitude of 0.07 (Figure 3.4). On its core surface (25.3γ), the spiciness anomalies appeared initially simultaneously in the STMW formation region and the central latitudes. They were found to spread southwestward to the entire domain of the STMW in 1–2 years. They disappeared finally at the western boundary without spreading northeastward after a direction change in geostrophic currents (Figure 3.4, 7, and 11). The southwestward propagation speed of the spiciness anomalies in the western subtropics was in the range of 0.06–0.09 m/s, almost twice the geostrophic current speed (Figure 3.11), suggesting the transport by eddies. Among isopycnals, the spiciness anomalies were relatively homogeneous in the STMW; however, they showed a delay from 25.00γ to 25.60γ during several months. These differed from the simultaneous decadal salinity variations found among latitudes and isopycnals along the 137°E (Oka et al., 2017).

The interannual and longer variability in the CMW during the Argo period were described for the first time. Salinity in the CMW showed a significant decreasing trend of $-0.004/\text{year}$, which was part of the large-scale freshening of the entire subtropics in the density range that was centered at 26.3γ and quasi-decadal variability that was out of the phase of the STMW (Figure 3.5 and 9). The spiciness anomalies at 26.3γ appeared initially near the western part of the CMW formation region. They spread southward to the majority of the CMW within the subtropical gyre and eastward to the eastern boundary near the boundary between the subtropical and subpolar gyres (Figure 3.9). Their propagation pathway in the subtropical gyre was not strictly along the geostrophic current; however, it was in the inner side of the gyre with a large southward component (Figure 3.12), which was likely caused by eddy transport. While low-frequency signals were propagated from the northern to the southern parts of the CMW with a 2-year delay, the robust year-to-year variations were confined to the northern part and

the formation region of the CMW, where strong spiciness fronts existed (Figure 3.5, 9, and 12). These were likely due to a double-diffusion related to the modification of the TRMW. In addition, L-CMW ($\gamma < 26.20$) and D-CMW ($\gamma > 26.20$), which have different formation regions, showed different year-to-year variations in a number of years.

In the ESTMW, the salinity values with a total time-scale of 3–4 years (Figure 3.6) showed larger seasonal and year-to-year variations than the other water masses. The spiciness anomalies appeared initially near its formation region and propagated clockwise in a direction and velocity that were consistent with the geostrophic currents. They finally arrived at the western boundary in the western tropics (Figure 3.8 and 10). The transport times across the domain of the ESTMW for the spiciness anomalies were within 1 year, which was shorter than the other water masses considered. Among different isopycnals, the spiciness anomalies between the light part ($\gamma < 24.85$) and dense part ($\gamma > 24.85$) of the ESTMW showed different year-to-year variations without a steady lag; however, the ranges found in their raw salinity were uniform (Figure 3.4c, 5c, and 6c).

Furthermore, we discussed the origins of the spiciness anomalies in the thermocline. In the western to central subtropics, the interannual spiciness anomalies in the thermocline were synchronized with the meridional shift of the outcrop lines of the isopycnals and the consequent interannual salinity anomalies in the mixed layer near the outcrop line - (negative salinity anomalies with further north outcrop line), with a lag of no longer than one year (Figure 3.13 and 14). Our results indicated that the spiciness anomalies observed in STMW and CMW were generated mainly in and subducted from the western to central parts of their outcropping region. It was consistent with some previous findings (Yan et al., 2017; Oka et al., 2019) and rejected the pathway the eastern subtropics-tropics to the western subtropics as supported by other results (Zhang and Liu, 1999; Ogata and Nonaka, 2020).

Meanwhile, in eastern subtropics, a few interannual signals appeared in the thermocline without a corresponding earlier occurrence in the mixed layer (Figure 3.13 and 14). These signals intensified after leaving the outcrop line (Figure 3.10 and 13). Notably, spiciness anomalies in the thermocline that corresponded to the meridional shifts of the outcrop line and the accompanying mixed layer salinity anomalies were found only near the center of ESTMW formation region. This implied the limited contribution of the mixed layer salinity variations in the generation of the spiciness anomalies in the eastern subtropics. It also provided new evidence for the contributions of spice injection after the work of Katsura (Katsura, 2018).

The main subject of this chapter was the spiciness anomalies that were subducted to the thermocline; therefore, we provided concise explanations of the generation mechanisms

involved. However, there are several issues that remain to be explained. For example, we found that the propagation speeds of the spiciness anomalies were faster than the geostrophic current in western subtropics. In addition, the spread of the spiciness anomalies was inclined to the inner side of the relevant streamlines and linked with eddy effects. Furthermore, the relationship between the salinity changes and the climate modes was interesting to discuss.

Table 3.1 Criteria for mode waters

	Upper limit of Q (γ range) ($\times 10^{-10} \text{ m}^{-1}\text{s}^{-1}$)	Latitude, longitude limits
STMW	2.5 (25.00-25.15) 2.25 (25.20-25.60)	20-35°N, 125°E-170°W
CMW	2 (26.00-26.35) 1.75 (26.40-26.45)	27-41°N, 170°E-160°W
ESTMW	4.5 (24.65-25.15)	17-31°N, 170-120°W

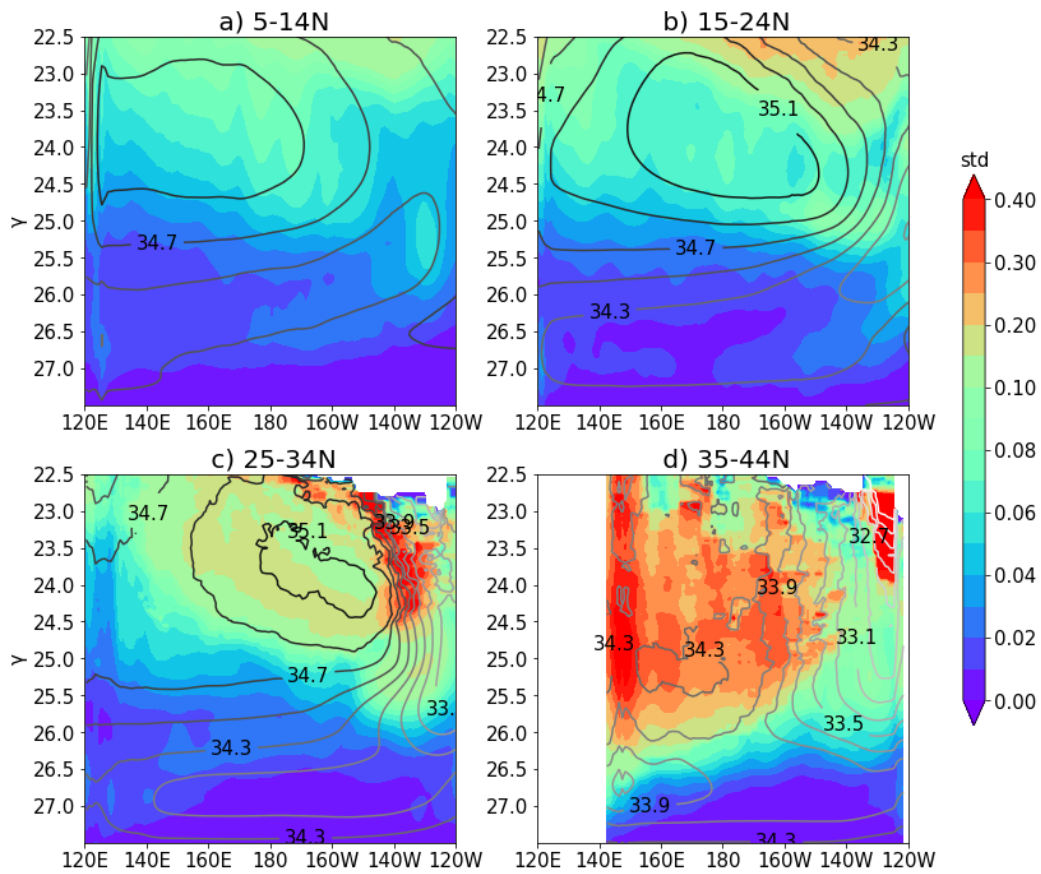


Figure 3.1 Climatology (contour) and standard deviation (color) of salinity (contour) during 2004-2018 with respect to neutral density, averaged in (a) 5°-14°N, (b) 15°-24°N, (c) 25°-34°N and (d) 35°-44°N respectively. Contour interval is 0.2. (The grids in the Sea of Japan are whitened in (d).)

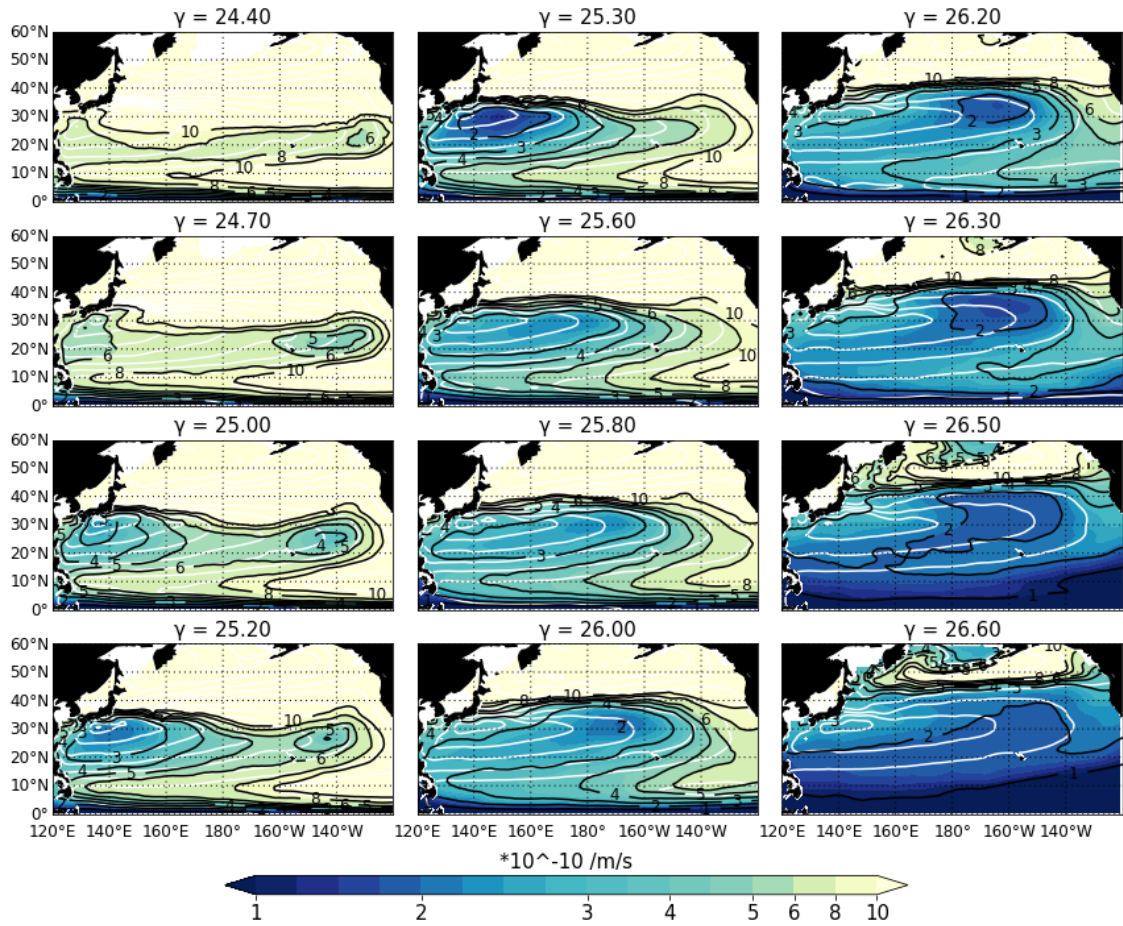


Figure 3.2 Climatological potential vorticity (Q ; unit: $10^{-10} \text{ m}^{-1}\text{s}^{-1}$) on surfaces $\gamma =$ (a) 24.40, (b) 24.70, (c) 25.00, (d) 25.30, (e) 25.60, (f) 25.8, (g) 26.00, (h) 26.30, and (i) 26.50. Black contours are for $Q = 1, 2, 3, 4, 5, 6, 8, 10 \times 10^{-10} \text{ m}^{-1}\text{s}^{-1}$. Colors in $1 \times 10^{-10} < Q < 3 \times 10^{-10} \text{ m}^{-1}\text{s}^{-1}$ change by every $0.25 \times 10^{-10} \text{ m}^{-1}\text{s}^{-1}$, and colors in $3 \times 10^{-10} < Q < 5 \times 10^{-10} \text{ m}^{-1}\text{s}^{-1}$ change by every $0.5 \times 10^{-10} \text{ m}^{-1}\text{s}^{-1}$. White contours denote isopycnal geostrophic streamfunction relative to 1500 dbar, with interval of $1 \text{ m}^2\text{s}^{-2}$.

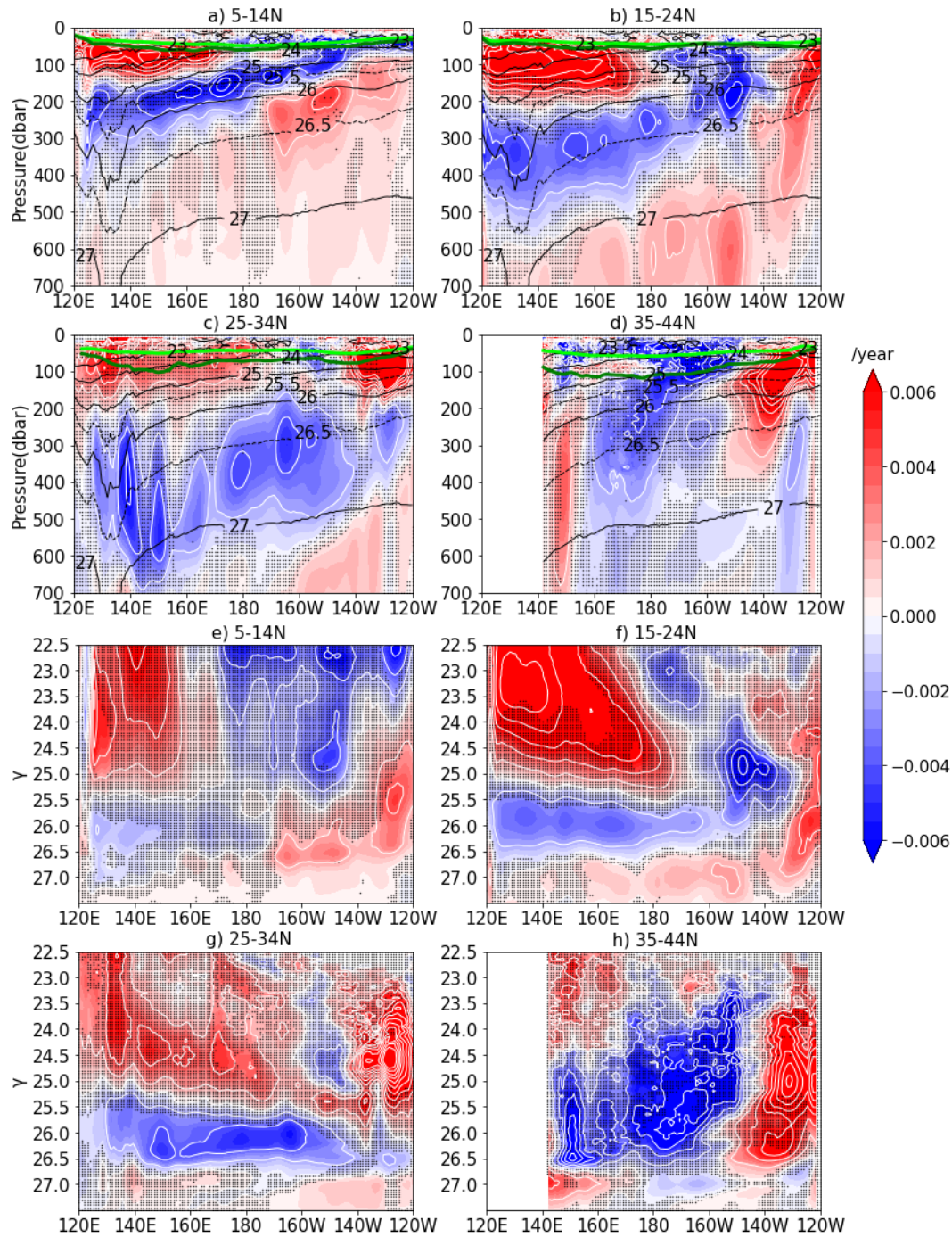


Figure 3.3 Salinity linear trend [color, and white contours (every 0.002); unit: year⁻¹] with respect to (a)-(d) pressure and (e)-(h) γ during 2004-2018, averaged in (a) (e) 5°-14°N, (b) (f) 15°-24°N, (c) (g) 25°-34°N and (d) (h) 35°-44°N. Stippled grids indicate where the trend is insignificant at 95% confidence level. In (a)-(d), light green and dark green lines represent all-season mixed layer depths and those only in Feb-Mar, respectively, and black contours indicate climatological neutral density (unit: kg·m⁻³).

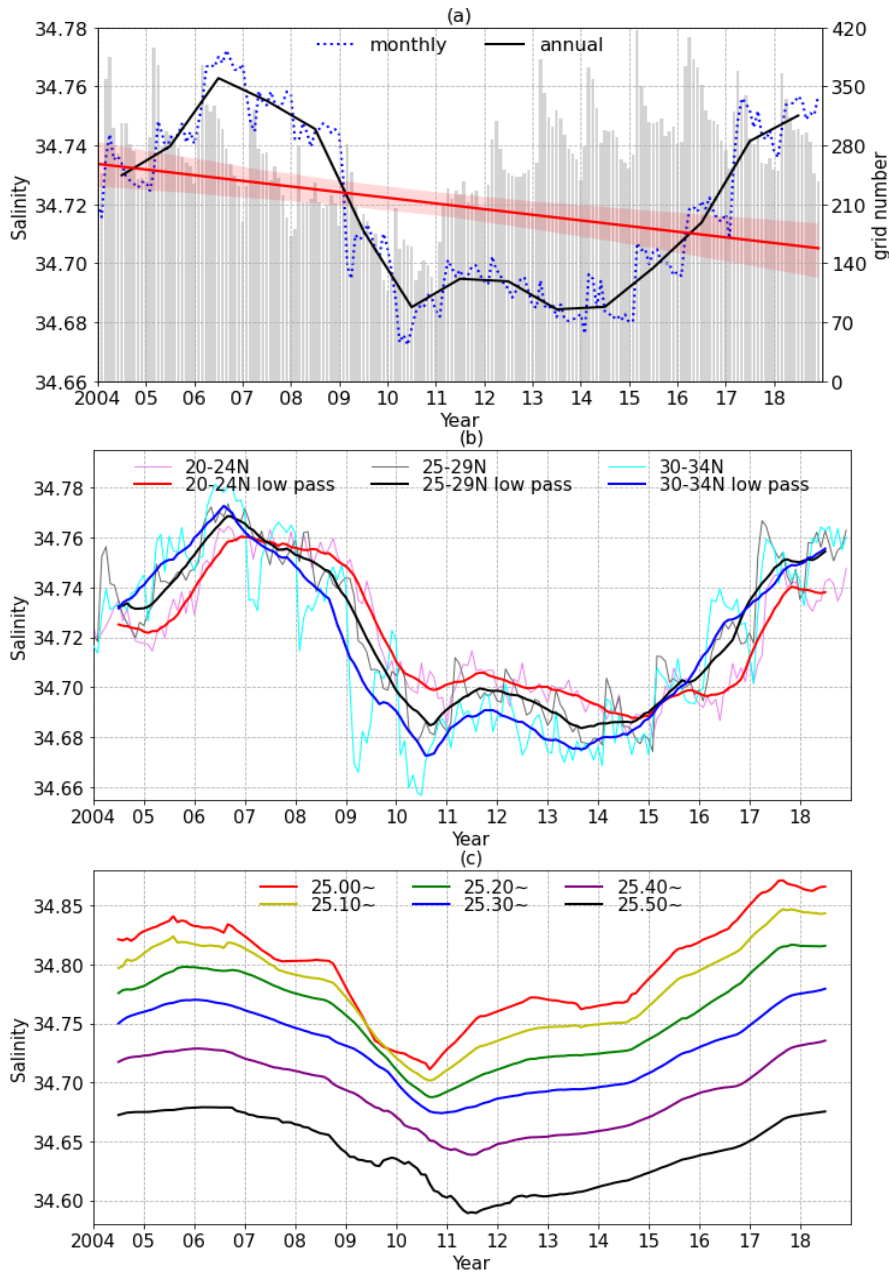


Figure 3.4 Time series of salinity in STMW: (a) Monthly (dotted blue), annual mean (solid black), and linear trend (solid red) with a 95% confidence interval (red band) of salinity, weight-averaged at each grid by the thickness of each γ surface. Gray bars represent the average number of $1^\circ \times 1^\circ$ grids that are used on one γ surface. (b) Salinity is weight-averaged by thickness in three latitude ranges: Pink (monthly) and red (12-month moving average) for 20-24°N, gray and black for 25-29°N, and light blue and blue for 30-34°N. (c) 12-month moving average salinity averaged on surfaces $\gamma = 25.00-25.05$ (red), $25.10-25.15$ (yellow), $25.20-25.25$ (green), $25.30-25.35$ (blue), $25.40-25.45$ (purple), and $25.50-25.60$ (black).

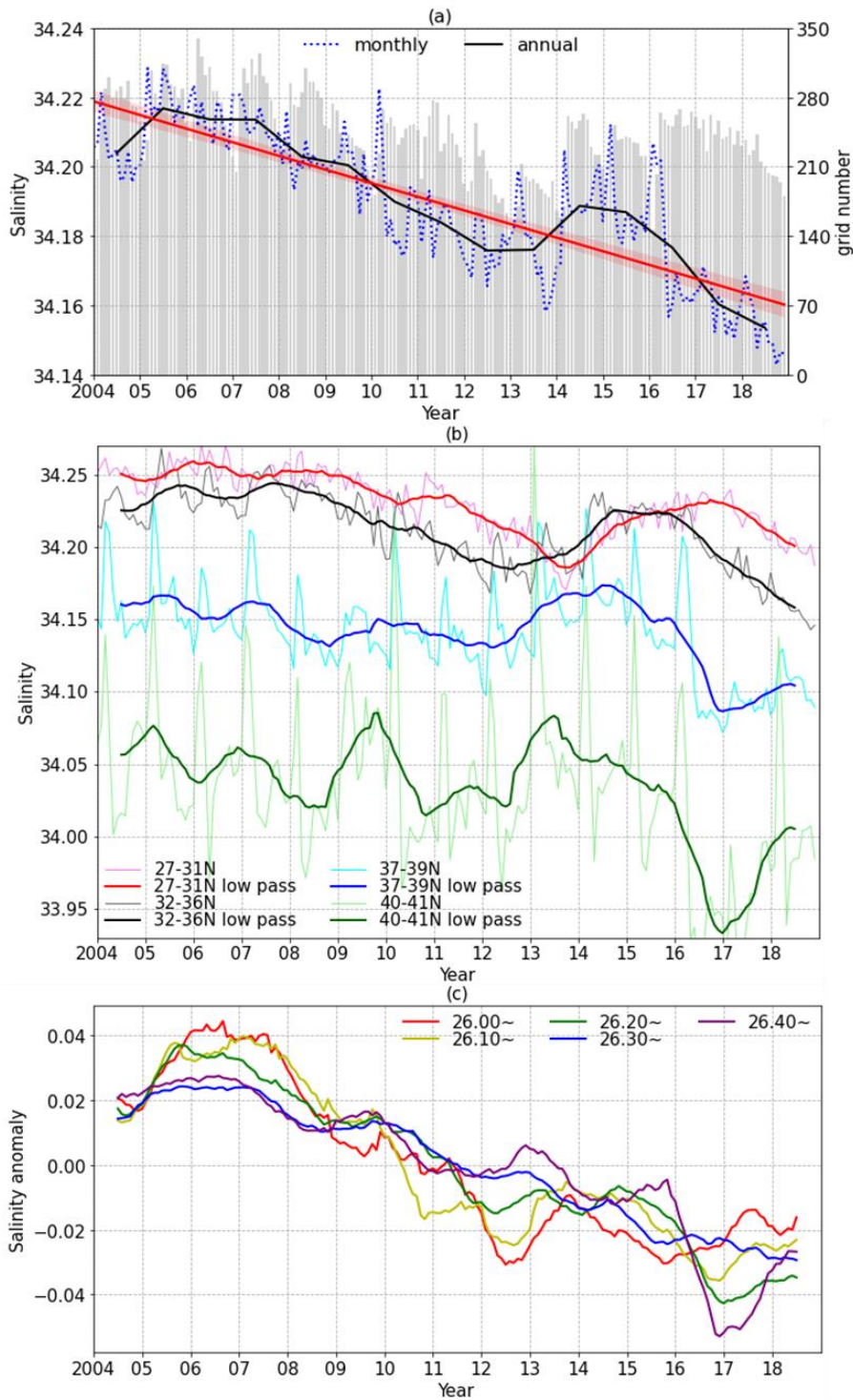


Figure 3.5 Same as **Figure 3.4** but for CMW, and (c) is for salinity anomaly because salinity ranges between different surfaces vary a lot in CMW. (b) In 27-31°N (pink and red), 32-36°N (gray and black), and 37-39°N (light blue and blue), 37-39°N (light green and green). (c) On surfaces $\gamma = 26.00-26.05$ (red), 26.10-26.15 (yellow), 26.20-26.25 (green), 26.30-26.35 (blue), and 26.40-26.45 (purple).

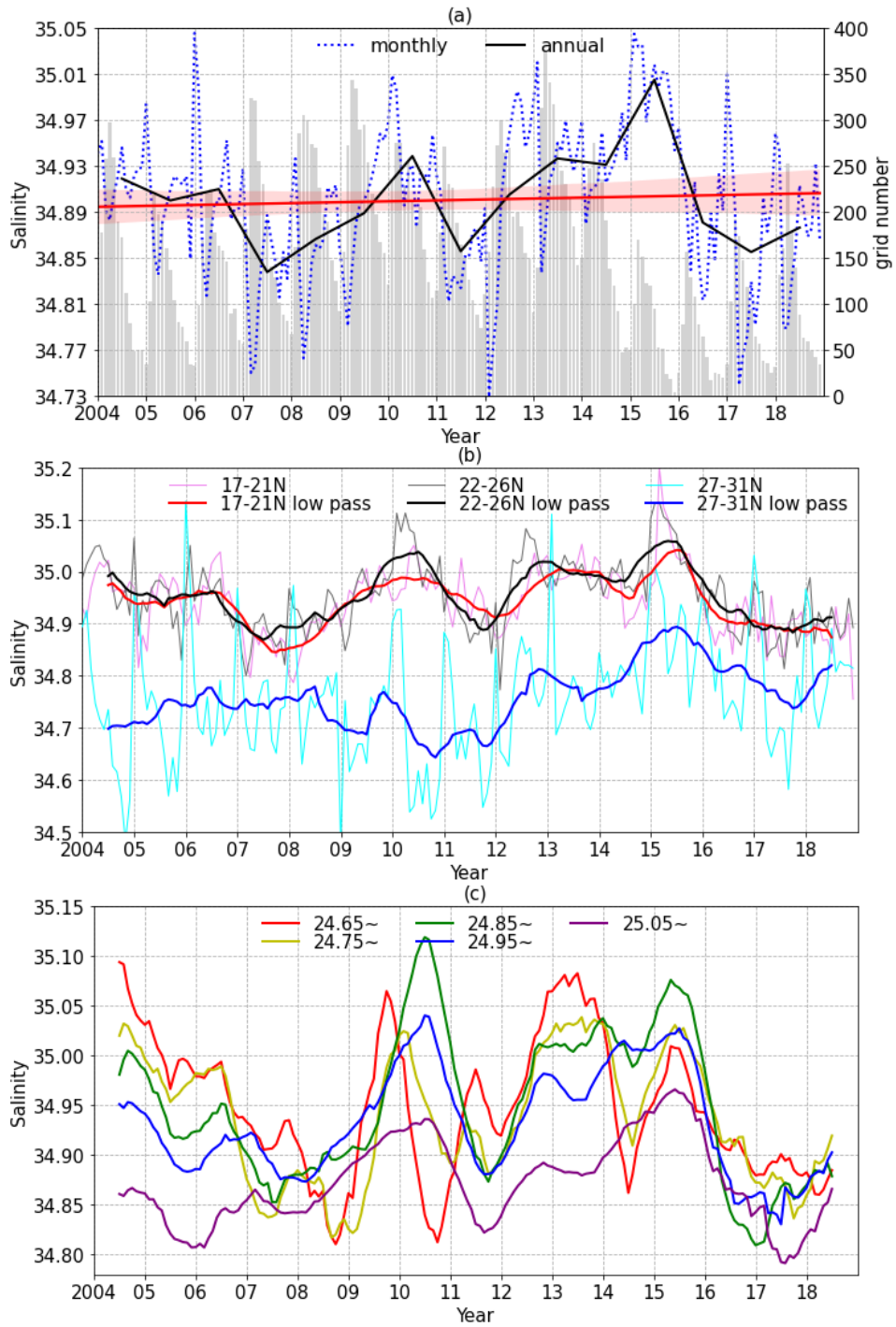


Figure 3.6 Same as **Figure 3.4** but for ESTMW. (b) In 17-21°N (pink and red), 22-26°N (gray and black), and 27-31°N (light blue and blue). (c) On surfaces $\gamma = 24.65$ -24.70 (red), 24.75-24.80 (yellow), 24.85-24.90 (green), 24.95-25.00 (blue), and 25.05-25.15 (purple).

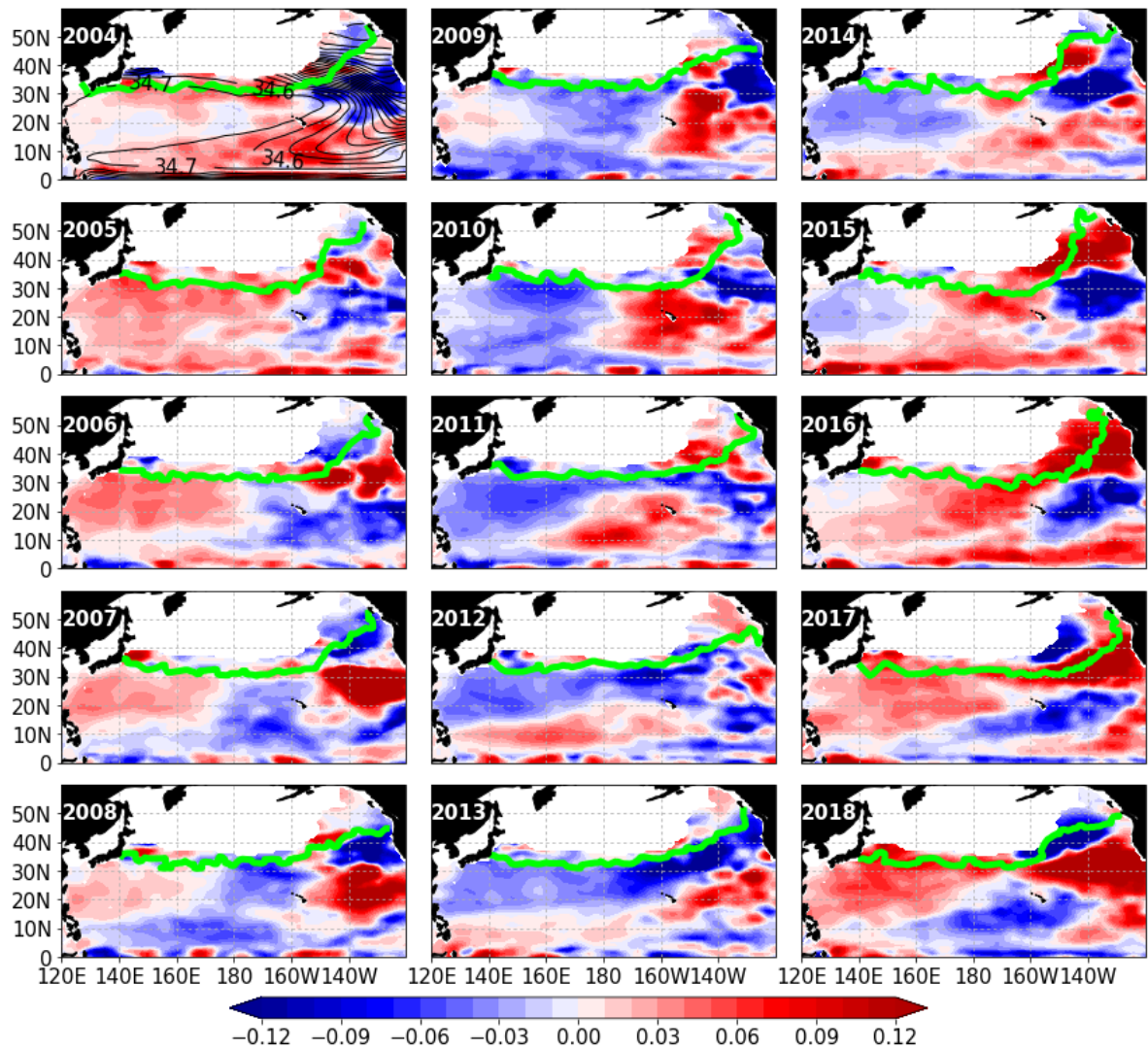


Figure 3.7 Annual mean anomalies of salinity on 25.3 γ surface. Climatological salinity (black contours) is shown in the subplot of 2004 with intervals of 0.1 and labels of 34.6 and 34.7. Light green lines denote the late winter outcrop line, averaged in February and March of each year.

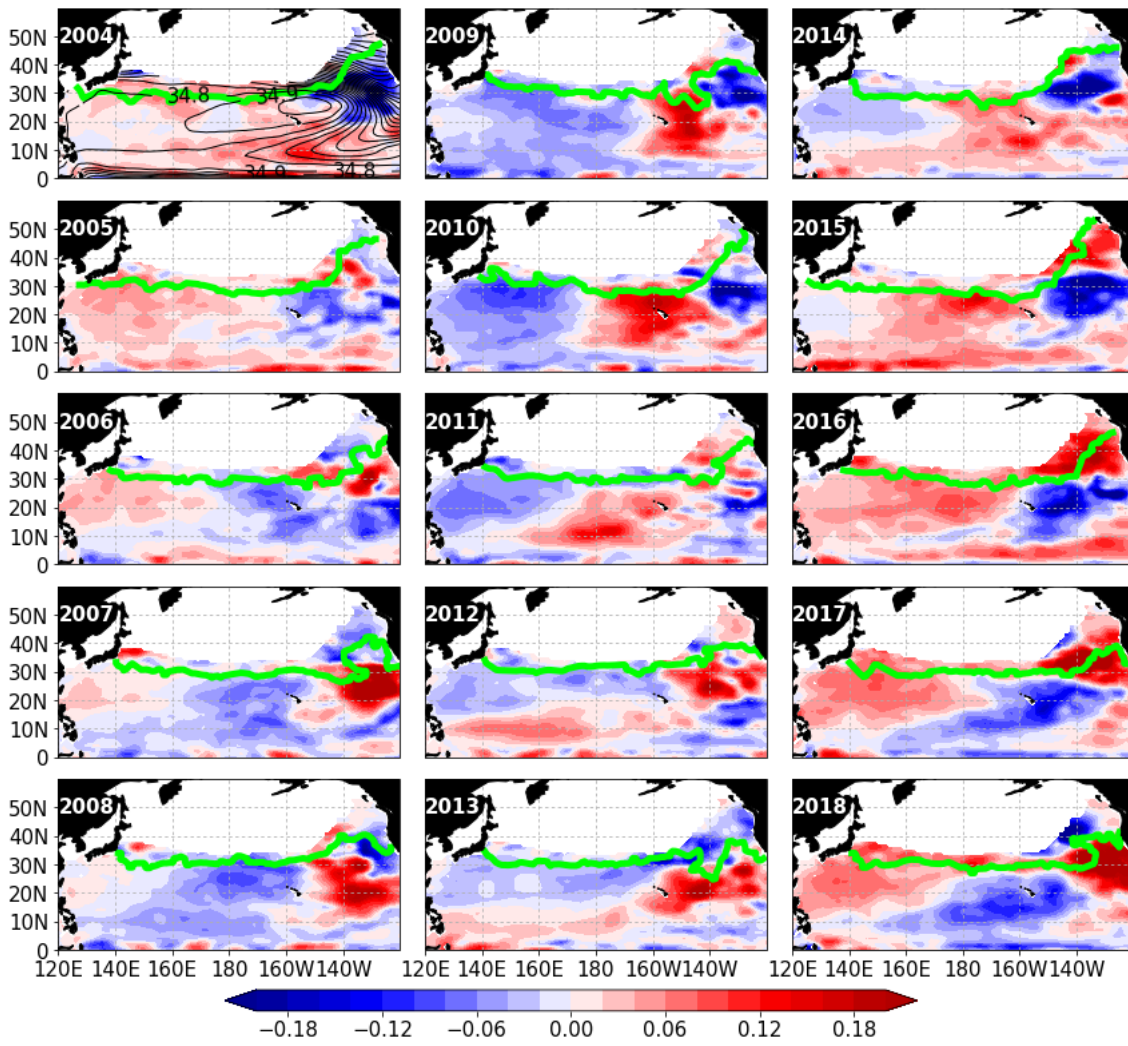


Figure 3.8 Same as Figure 3.7 but on a 25.0γ surface, with labels of 34.2 and 34.3.

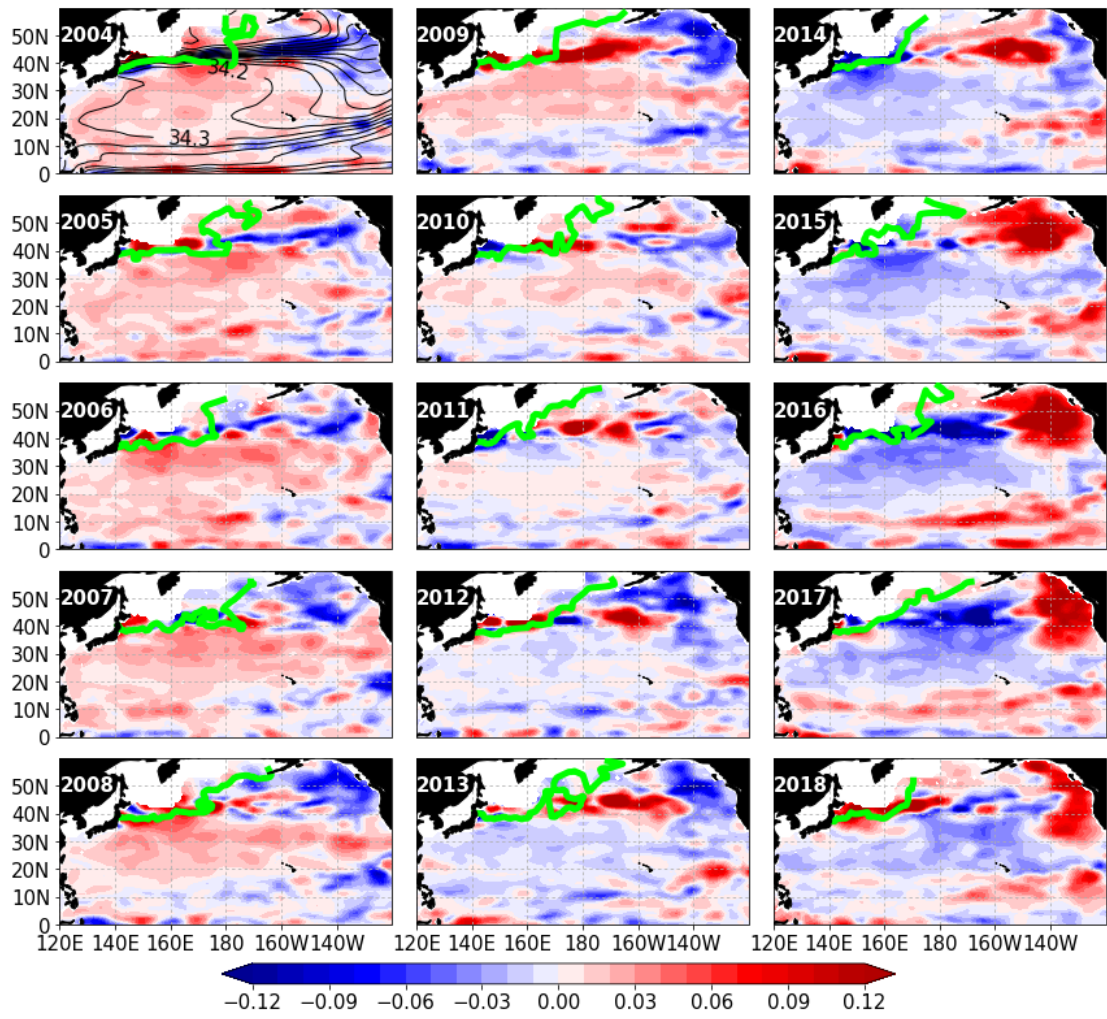


Figure 3.9 Same as Figure 3.7 but on a 26.3 γ surface, with labels of 34.8 and 34.9.

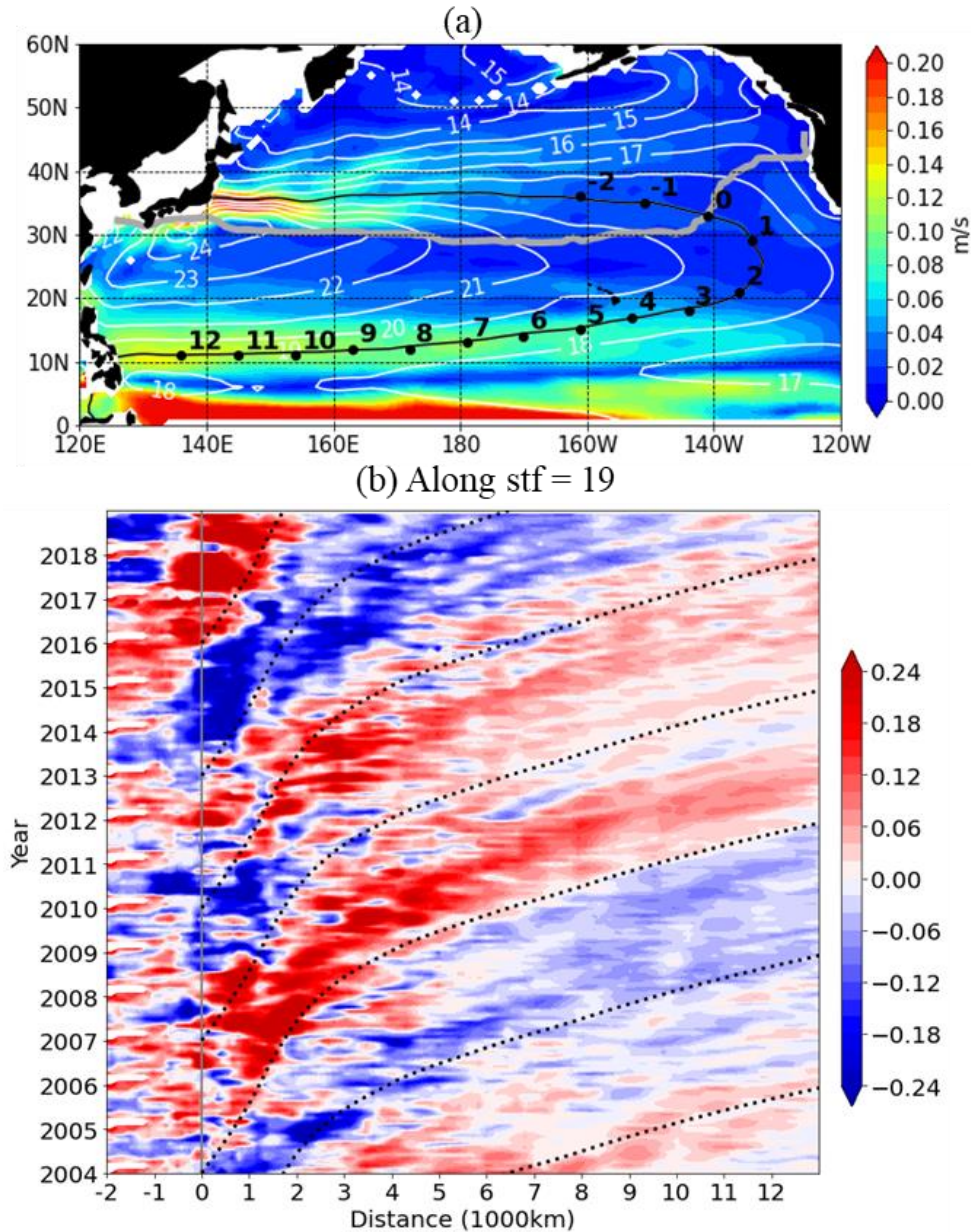


Figure 3.10 (a) Geostrophic velocity (color) and streamline (white contour) on $\gamma = 25.0$ surface (unit: m/s) relative to 1500 dbar. Black contour denotes the 19 isopycnal streamfunction isopleth, with positions dotted every 1000 km distance (the great-circle distance at each pressure) from the “0” point. Thick gray line denotes the winter outcrop line of $\gamma = 25.0$ surface. (b) Time-distance diagram of salinity anomalies along the 19 isopycnal streamfunction isopleth (Same as the black contour in (a)). Dotted black curves denote the advection by mean geostrophic velocity along the streamline, integrated from the “0” point (gray line). The positions of every 1000km distance are the same as the dotted points in (a).

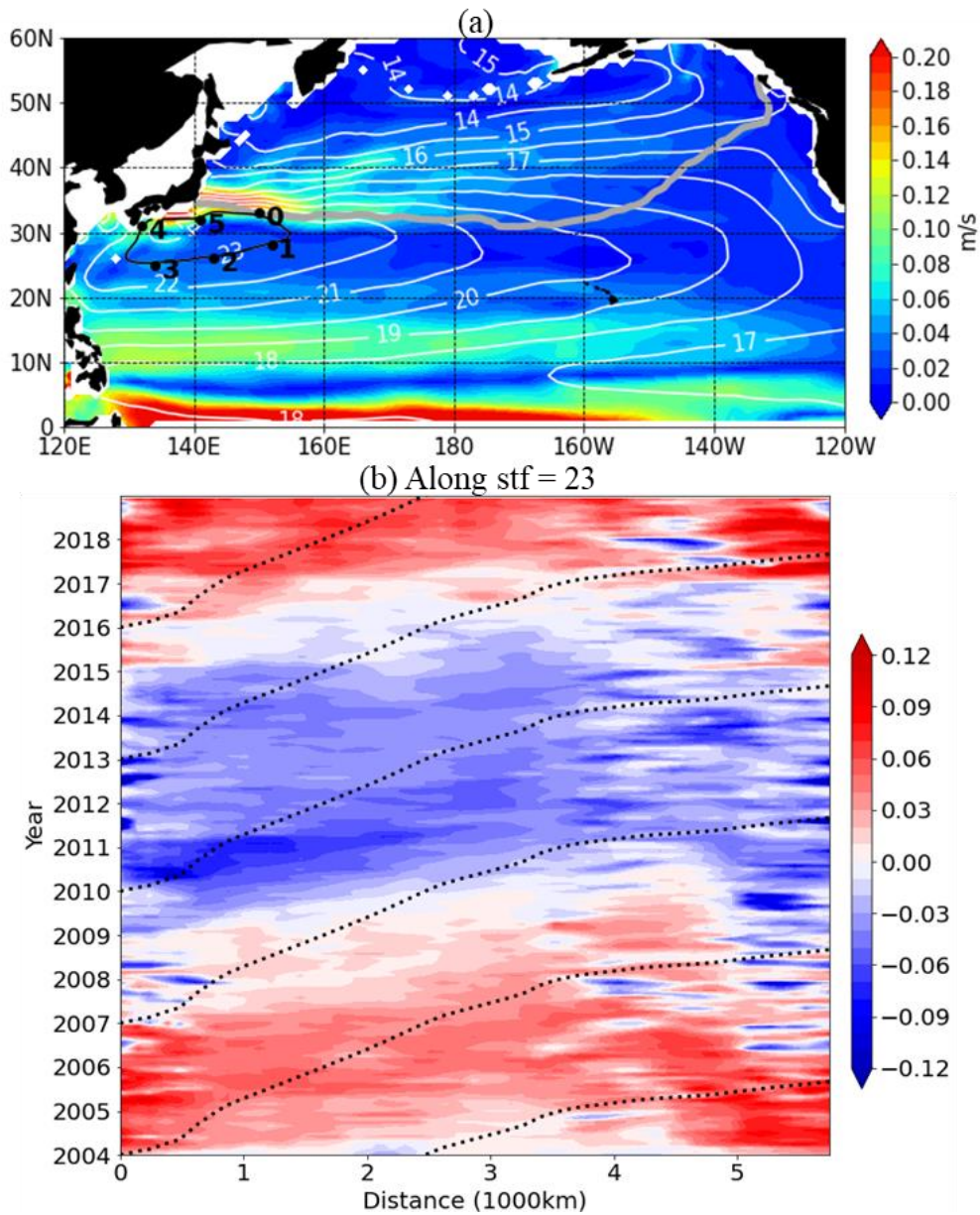


Figure 3.11 Same as **Figure 3.10** but on $\gamma = 25.3$ surface along 23 streamfunction isopleth.

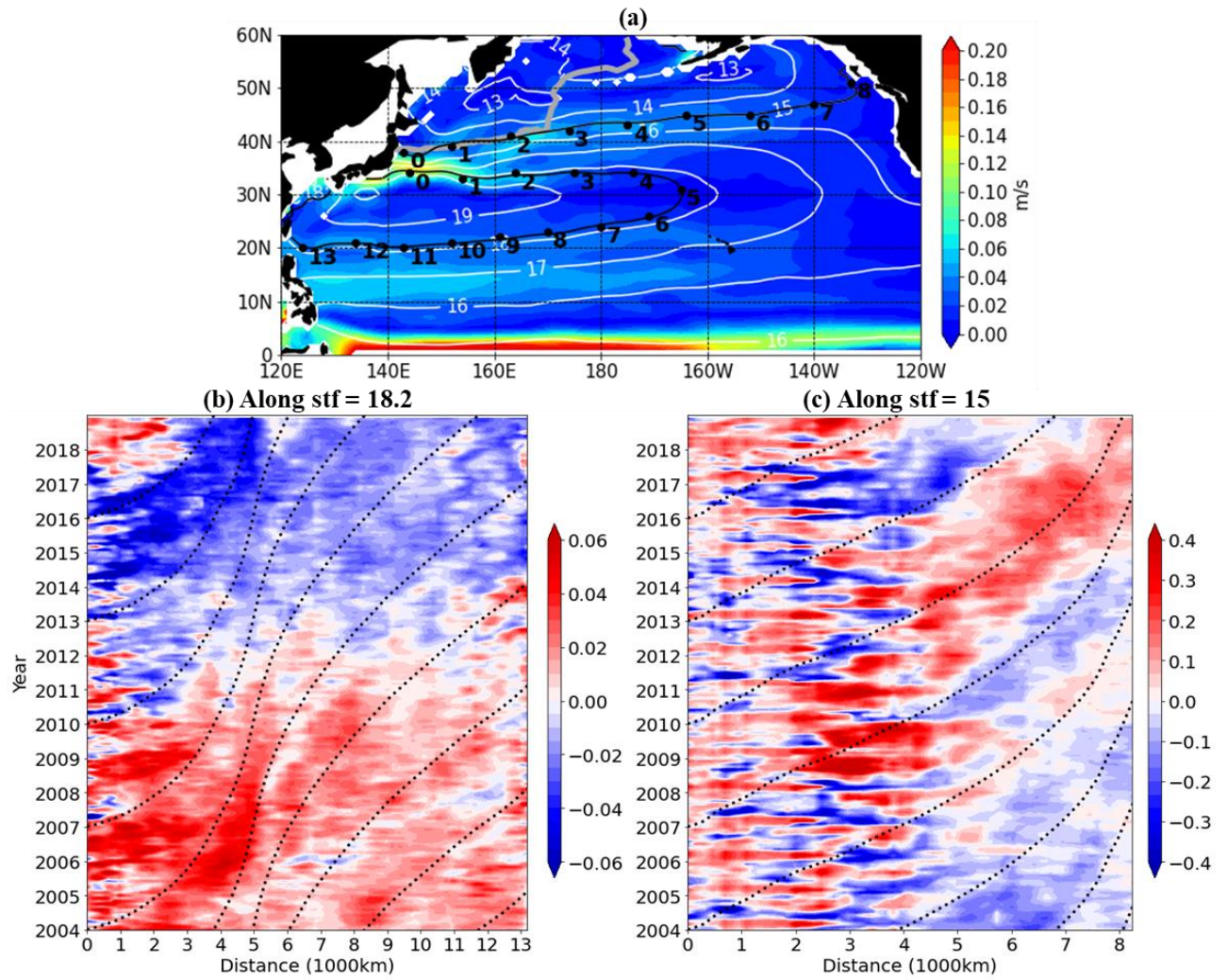


Figure 3.12 Same as **Figure 3.10** but on $\gamma = 26.3$ surface along (b) 18.2 and (c) 15 streamfunction isopleths.

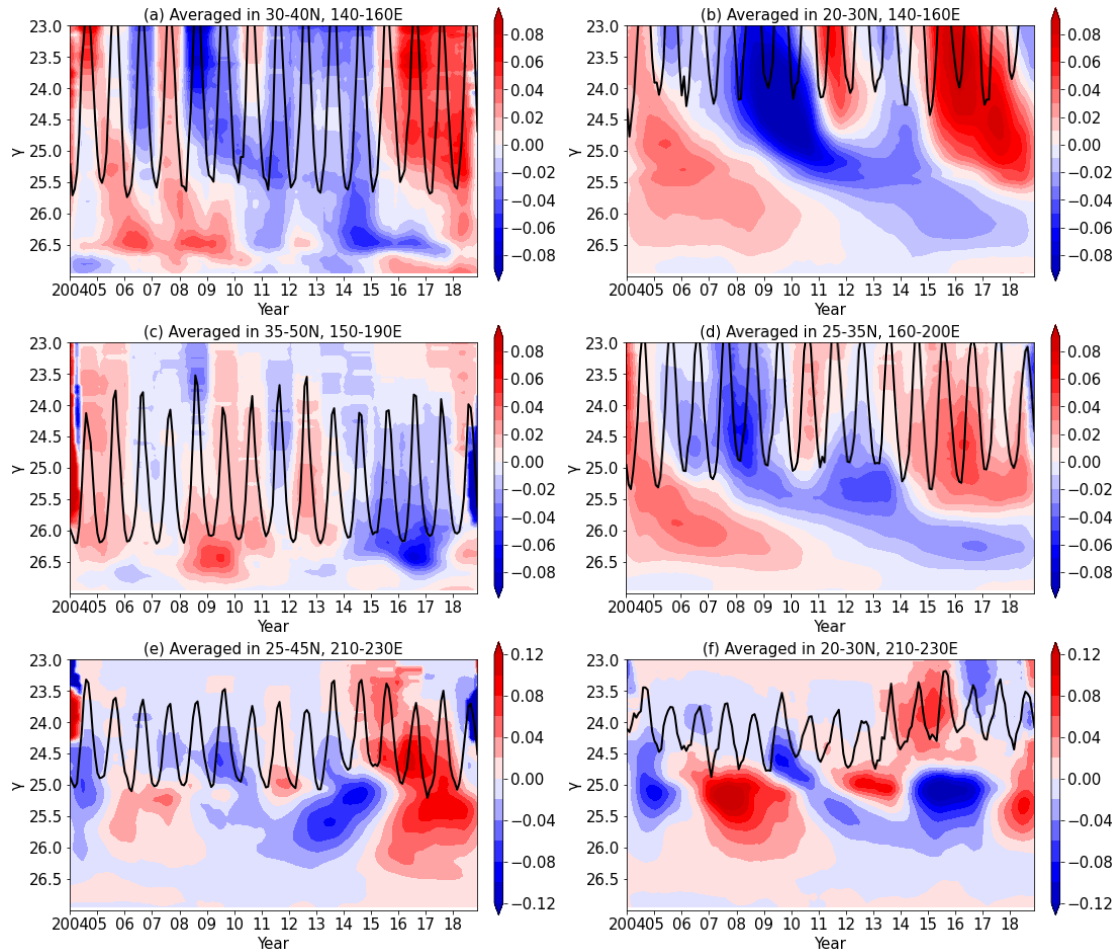


Figure 3.13 γ -time diagram of 12-month running average salinity anomalies averaged in boxes representing the formation region and downstream distribution region of the three mode waters: (a) 30-40°N, 140-160°E, representing STMW formation region, (b) 20-30°N, 140-160°E, representing STMW distribution region, (c) 35-50°N, 150°E -170°W, representing CMW formation region, (d) 25-35°N, 160°E -160°W, representing CMW distribution region, (e) 25-45°N, 150-130°W, representing ESTMW formation region, (f) 20-30°N, 150-130°W, representing ESTMW distribution region. Black contours denote the potential density of the mixed layer. The latitude ranges of (a) (c) (e) are chosen based on **Figure 3.14**.

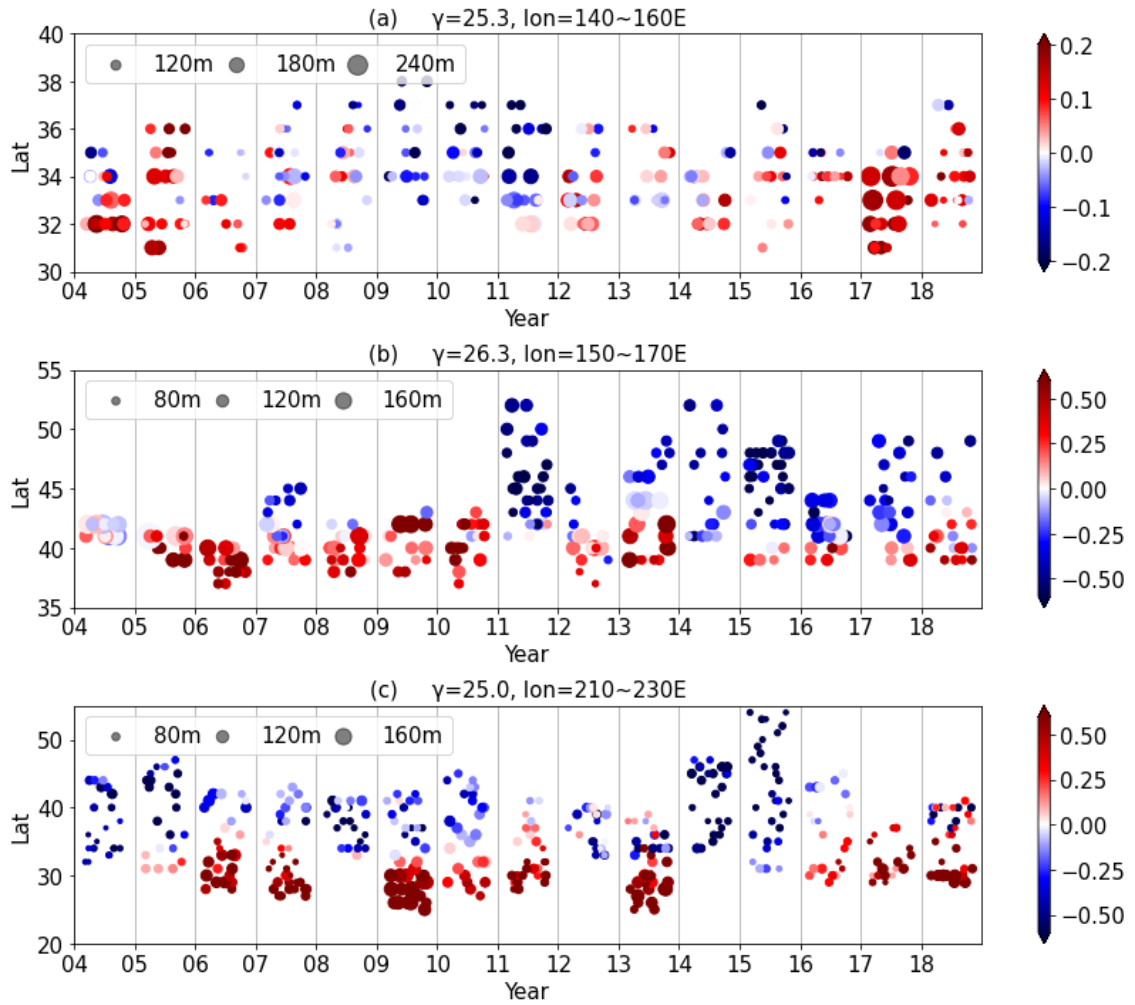


Figure 3.14 Scatterplot of the latitudes of the grids on late-winter outcrop line of the mode water core surfaces in their main formation regions in each year: (a) for $\gamma = 25.3$, in $140\text{-}160^\circ\text{E}$, (b) for $\gamma = 26.3$, in $150\text{-}170^\circ\text{E}$, and (c) for $\gamma = 25.0$, in $150\text{-}130^\circ\text{W}$. Colors of the scatters indicate salinity anomalies in the late-winter mixed layer, calculated by salinity at each plotted grid subtracted by the climatological salinity averaged at each longitude on the outcrop line. The horizontal position of the scatters was randomly distributed within the bin of each year to avoid overlap. The size of the scatters indicates the MLD.

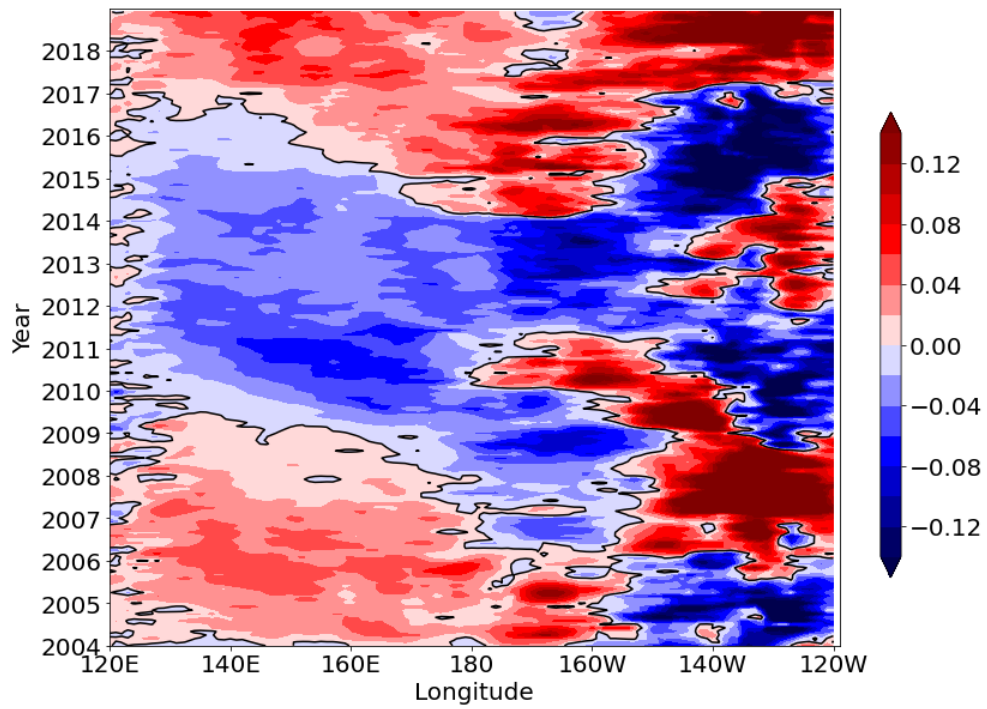


Figure 3.15 Time-longitude diagram of salinity anomalies averaged in 25-30°N on $\gamma = 25.3$. Black contours denote zero value.

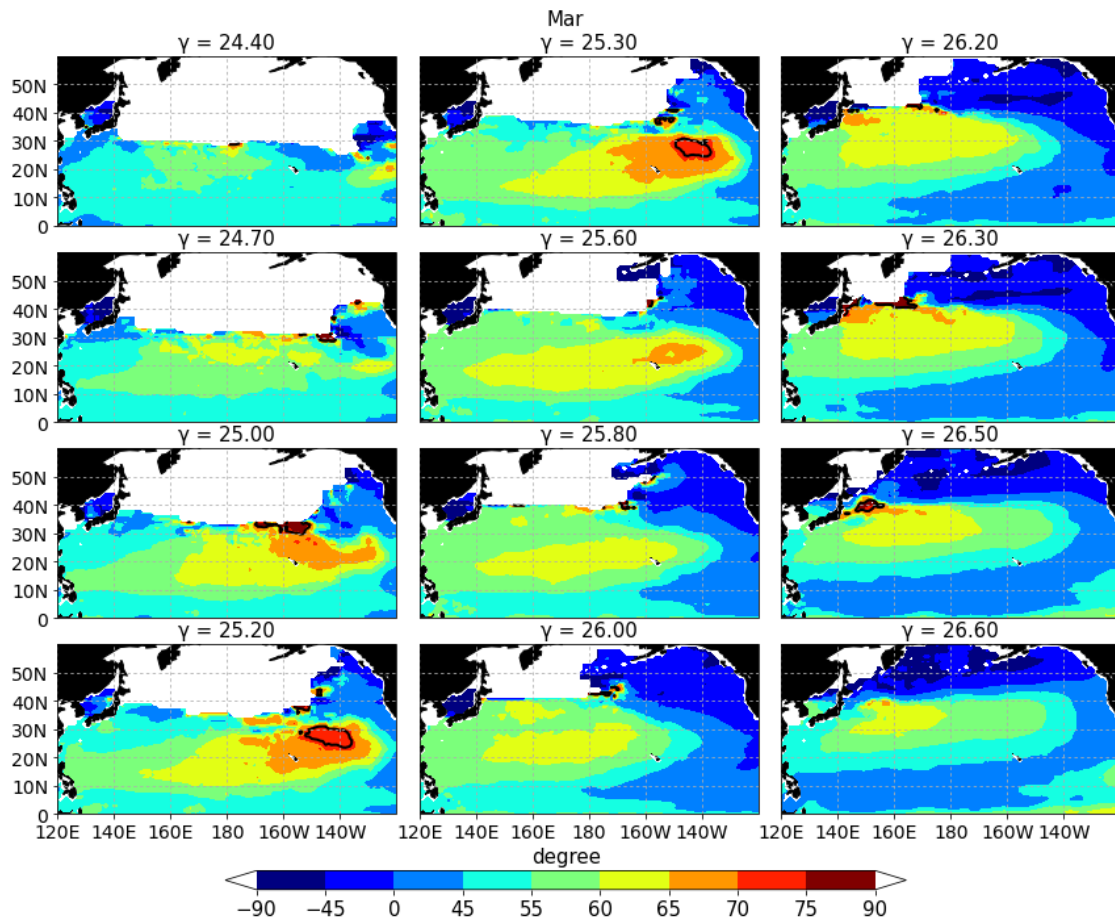


Figure 3.16 Distribution of Turner angle on selected γ surfaces (same as Figure 3.2 in main body); black contours indicate 71.6° .

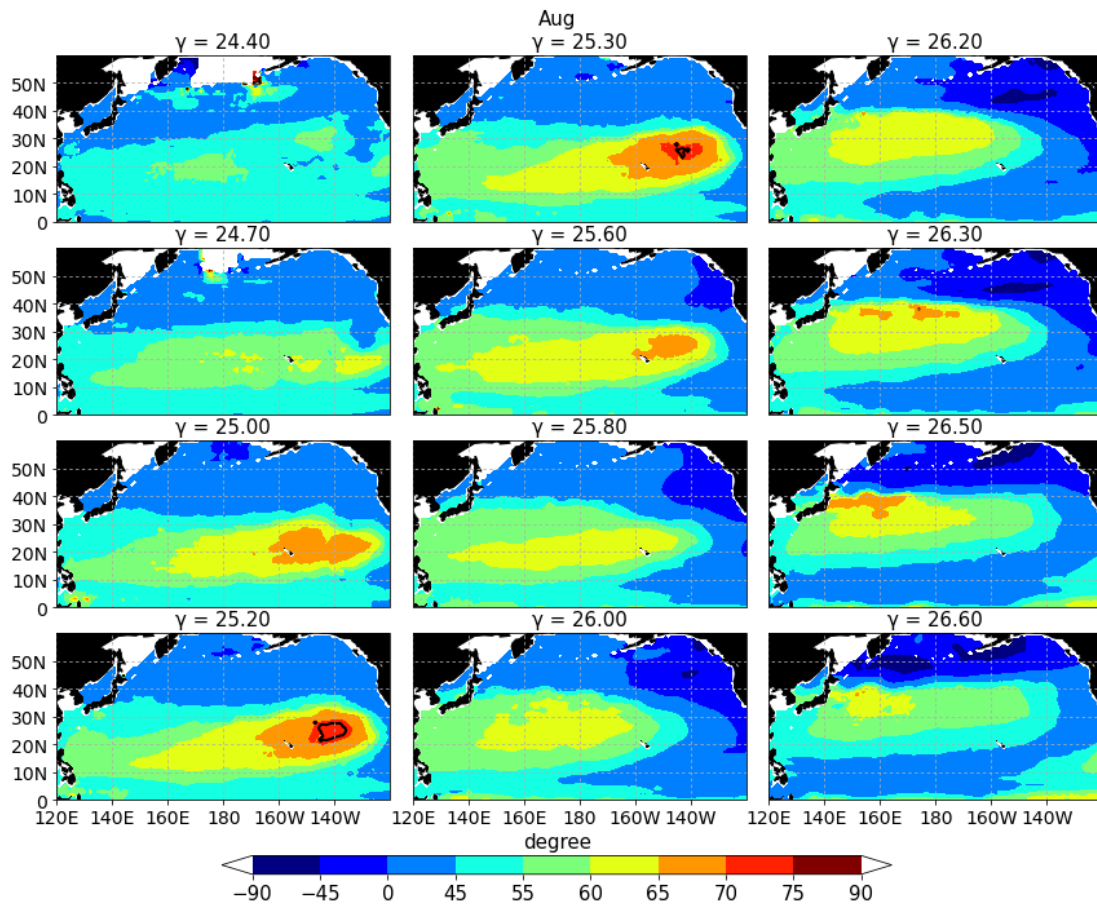


Figure 3.17 Same as **Figure 3.16** but for August.

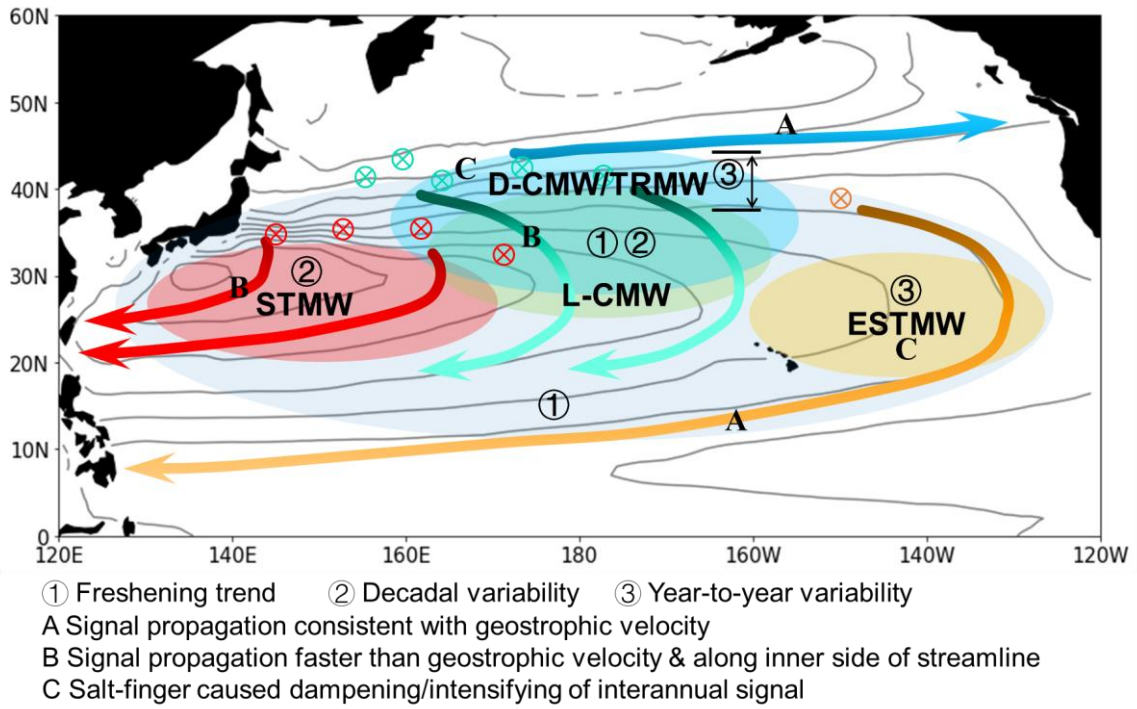


Figure 3.18 Schematic map illustrating the propagation pathways of spiciness anomalies. Gray contours in the background indicate streamlines averaged on $\gamma = 24.4-26.5$. Crosses with circles indicate subduction of mixed layer salinity anomalies.

4 Spatiotemporal evolutions of thickness anomalies

4.1 Introduction

As mentioned in Chapter 1, the thermohaline variations along isopycnals alone are not enough to interpret the climate changes including global warming in ocean. The knowledge of the other component, vertical displacement of isopycnals, is necessary.

Using heave/spice decomposition, Häkkinen et al. (2016) and Desbruyères et al. (2017) revealed that the recent warming of the upper ocean is explained by a deepening of lighter subtropical isopycnal surfaces rather than by the temperature change along the isopycnals. The heave-related warming is damped by negative spiciness anomalies, supporting the “pure warming” scenario of a typical subtropical water column (warm/salty waters over cold/fresh waters) (Bindoff and McDougall, 1994). However, they only diagnosed long-term trends at the basin scale and did not investigate different regions with the linkage of water masses. Kolodziejczyk et al. (2019) suggested large thickness variability at $\sigma_\theta = 26.0\text{--}26.5 \text{ kg/m}^3$ and $\sigma_\theta = 27.0\text{--}27.7 \text{ kg/m}^3$ in the Northern Hemisphere. However, they did not mention those in the lighter layers, and the propagations of the thickness anomalies were only investigated in the South Pacific.

The relationship between STMW thickness and KE has been a controversial issue. Qiu and Chen (2006) first raised that the thickness of STMW is controlled more by the dynamic state of the KE system instead of the air-sea flux forcing in modelling studies. When the KE path is in an unstable state, high eddy activities infuse high-PV water from KE region into the recirculation gyre, increasing the upper-ocean stratification and forming a thinner mixed layer, and resulting in less STMW formation; on the opposite, a stable KE state favors the maintenance of a weak stratification, leading to a deep winter mixed layer and more formation of STMW. They also confirmed this relationship in observational temperature and altimetrically derived sea surface height data. This relationship was later detected by Miyazawa et al. (2009) from reanalysis data. While the above studies suggested that a stable (unstable) KE period causes a large (small) STMW thickness, Oka et al. (2015) addressed that the thickness increased (decreased) gradually during which period.

On the other hand, Sugimoto and Hanawa (2010) suggested that the STMW thickness variation is predominantly controlled by the main thermocline depth related to large-scale atmospheric forcing, using temperature profiles and wind-driven hindcast ocean model. When the main thermocline deepens (shoals), wintertime mixed layer depth is deeper (shallower), and consequently, thicker (thinner) STMW is observed. The changes in main thermocline depth are

caused by a baroclinic response in the ocean to the Aleutian Low activity, especially its meridional movement, and this movement lags STMW formation for about three years. The above dominant role of main thermocline depth on STMW thickness, is also supported by the results in Tsubouchi et al. (2016) using HydroBase T/S climatology, and they also implied the important role of western boundary current transport and suggested the weak influence of surface heat flux on STMW thickness.

Since the western part of the CMW formation region is also around the KE system, the KE variability can also cause variability in CMW formation. This has been revealed by Oka et al. (2012) using Argo floats during 2002-2011: more formation of D-CMW (L-CMW) during stable (unstable) KE, but they did not investigate the propagation of the anomalous formation. Other studies explain the decadal change of CMW volume with large-scale climate regime shifts (Yasuda and Hanawa, 1997; Suga et al., 2003). The latter is related to PDO, and its mechanism has been investigated by numerical simulations (Ladd and Thompson, 2002; Hosoda et al., 2004). However, the decadal or longer variations of CMW thickness in the Argo period have not been well described.

In early studies about ESTMW, Hautala and Roemmich (1998) did not find a substantial change in the ESTMW volume and temperature between 1970–1979 and 1991–1997. More recently, Guo et al. (2018) and Katsura (2018) reported PDO-associated interannual variations of the ESTMW thickness. When the PDO index is positive, more net heat input, more precipitation, lighter sea surface density, and shallower mixed layer depth in the ESTMW formation region result in less ESTMW volume. Since PDO can also influence the formation region of CMW and STMW, it would also be interesting to compare the time scale and phases of the thickness variations of the three mode waters, while few previous studies mentioned. In an eddy-resolving ocean model, Chen et al. (2010) revealed an anti-correlated variability in the subduction rate of western and eastern subtropics related to PDO: during the positive phase of PDO, the winter mixed layer depth gets deeper in the west and shallower in the east, being closely related to the variability in surface heat flux stemming from an enhanced Aleutian Low, and the changes in subtropical gyre circulation also play a role. Using the Simple Ocean Data Assimilation (SODA), Kwon et al. (2013) suggested that a cold phase of PDO causes an increase in volume of CMW density class ($\gamma = 25.6\text{--}26.6$) related to the southward expansion of its winter outcrop window, and it is partly compensated by a reduced water supply to the STMW density class ($\gamma = 24.0\text{--}25.5$). Considering the different correlations between volume change of different mode waters, it would be instructive also to investigate them with Argo profiles and discuss the large-scale changes.

In this chapter, the purpose is to comprehensively describe the thickness anomalies and their propagation in the upper North Pacific, focusing on STMW, CMW, and ESTMW. The remainder of this chapter is as follows: Section 4.2 shows the climatology and standard deviation of isopycnal thickness and depth. Section 4.3 describes the temporal evolutions in the three water masses. 4.4 describes the spatial evolutions of thickness anomalies on their core γ surfaces. 4.5 quantifies the propagation speeds of spiciness anomalies and compares them with the geostrophic currents. 4.6 gives a preliminary discussion on the influence of Kuroshio Extension (KE) and Pacific Decadal Oscillation (PDO; Mantua et al., 1997). Section 4.7 summarizes the finding and raises issues for future work.

4.2 Mean state

It is instructive to first look at the mean state of the isopycnal thickness and depth before investigating their evolutions. Figure 4.1 shows the climatology and standard deviation of the thickness and depth of the isopycnals. Isopycnals with large thickness compared to the surrounding water were found at $\gamma = 25.0-25.5$ west of 180°E in $15-34^\circ\text{N}$, $\gamma = 24.5-25.2$ east of 160°W in $15-34^\circ\text{N}$, and $\gamma = 26.0-26.8$ near the central latitudes in $25-34^\circ\text{N}$. The above density ranges and positions generally correspond to STMW, ESTMW, and CMW, respectively. This is consistent with the fundamental characteristic of mode waters, low Q .

Large variations of thickness occurred at $\gamma = 25-25.5$ in $140-160^\circ\text{E}$ and at $\gamma = 24-25$ east of 160°W in $25-34^\circ\text{N}$, corresponding to the formation region and distribution region of STMW and ESTMW. Large variations were also found at $\gamma = 24.5-26.7$ widely in $35-44^\circ\text{N}$, which not only includes the formation region of CMW but also is related to the outcrop of these isopycnals. Out of the mode waters, large variations of isopycnal thickness were also observed at $\gamma = 27-28$ at all longitudes and latitudes, corresponding to the intermediate waters. The latter two density ranges were consistent with those of large thickness variations in the North Pacific suggested by Kolodziejczyk et al. (2019), which were at $\sigma_\theta = 26.0-26.5 \text{ kg/m}^3$ and $\sigma_\theta = 27.0-27.7 \text{ kg/m}^3$. However, the standard deviation of isopycnal depths shows different patterns (Figure 4.1 e-h). In each latitude range, depth variations are much larger in the western North Pacific than in the eastern North Pacific, indicating stronger heaving movements on the western side.

4.3 Temporal variations of thickness anomalies

The linear trend of thickness and depth anomalies are shown in Figure 4.2. In $5-24^\circ\text{N}$, there was a thickening trend at $\gamma = 27.0-27.5$ in most longitudes, with a value stronger than 0.12

dbar/year (Figure 4.2 a-b). It was accompanied by the shallowing of the layer above and the deepening of the layer below (Figure 4.2 e-f). Especially in 170-135°W, the isopycnals with a significant shallowing trend was at $\gamma = 23.0-26.7$ in 5-14°N and at $\gamma = 25.2-27.2$ in 15-24°N, connected to the seasonal pycnocline and the upper main pycnocline. In 25-34°N, isopycnals with γ value 25.4-25.8 thickened in 160°E-160°W, and accompanied by the deepening of the layer below, while the layer above did not show a significant trend (Figure 4.2 c and g). In 35-44°N, the layer $\gamma = 26.3-27.9$ deepened both west of 175°E and east of 165°W, accompanied by the thickening of the layer $\gamma = 26.2-26.7$ in this region (Figure 4.2 d and h). However, in the central longitudes in 180°-165°W, the deepening of the isopycnals occurred on a lighter density range, which was $\gamma = 25.7-26.4$, accompanied with the shrinking of the layer below, which has a γ range of 26.4-26.8. In the above cases, the corresponding relations between the isopycnal thickness changes and the isopycnal depths changes above and below were not the same, indicating that heaving can influence the stratification of the seasonal and main pycnoclines in a different way.

The total volume of STMW was dominated by a decadal variability (Figure 4.3 a). It showed a significant decrease during 2006-2009, which had been suggested by Cerovecki and Giglio (2016). Compared to the STMW salinity, the phase of volume was earlier, and the volume increased right after the minimum in 2010, unlike the minor change in 2010-2013 of salinity. Besides, the grid number that meets the criteria of STMW, the area-mean thickness of the STMW grids (not shown here), and the total volume of STMW were consistent, indicating the volume change were caused by the changes of both the area that outcropped and the vertical stratification. Compared between different latitude ranges, the volume change was quite uniform, with a larger amplitude on the middle and northern side, and a delay from the northern side to the southern side within one year, and it was shorter than the lag of salinity (Figure 4.3 b). Thickness anomalies between different surfaces were not as consistent as spiciness anomalies. In particular, the parts of $\gamma = 25.00-25.25$ and $\gamma = 25.30-25.60$ showed opposite variations in some years (Figure 4.3 c). It implied the variations in the formation of different proportions of STMW. For example, in 2004 and 2018, the condition in the STMW formation region was in favor of forming denser STMW, while in 2010, lighter STMW were formed. The above results suggested that thickness anomalies in STMW have a higher frequency and a faster propagation speed from the formation region to the entire STMW than spiciness anomalies.

In CMW, total volume decreased at a rate of $10^{13}\text{m}^3/\text{year}$ with a quasi-decadal variability (Figure 4.4 a). Compared to salinity, the interannual and decadal variabilities in volume were more evident. The first peak, the trough, and the second peak of volume were in 2007, 2013, and

2017, respectively, while those of salinity were in 2005, 2012, and 2014, indicating a later phase of volume than salinity. The consistency of variations between different latitude ranges was much better in volume than in salinity (Figure 4.4 b). Both the volume and the interannual variations were the largest in 32-36°N. The interannual variations were similar in 37-39°N, 32-36°N, and 27-31°N, but with a lag of about 2 years from the north to the south. The variations in 40-41°N had a lower frequency, suggesting that the year-to-year variations were most likely generated near 32-36°N. As mentioned before, the year-to-year variations of salinity that were confined only to the northern part of CMW were probably caused by spice injection related to the modification of TRMW. Since the TRMW and D-CMW has comparable densities, this process does not need to cause large density changes. Therefore, the volume changes of CMW, which showed good consistency between different latitudes, were most likely caused by a large-scale change in stratification instead of double diffusion.

The thickness anomalies between different layers of CMW (see Figure 4.4 c), though they showed different variations in some years, did not have a distinct separation between L-CMW and D-CMW, let alone the opposite variations between light and dense parts shown in STMW. This could be considered from the formation of the two mode waters. The formation region of STMW is just north of it and is in a confined area; thus, an increase in denser (lighter) water can cause a decrease in lighter (denser) water. Meanwhile, the formation region of CMW is vast both zonally and meridionally; thus, the source waters of different densities can be from different positions, and they do not need to influence each other.

The volume of ESTMW showed different variations with salinity. There were two peaks in 2009 and 2013, a decrease between them in 2011, and two troughs in 2005 and 2016 (Figure 4.4 a). While the salinity of ESTMW was dominated by year-to-year variations and interannual variations of 3-4 year time scale, the volume of ESTMW overall showed a quasi-decadal variability with a rapid shrinking in 2010-2011. The year-to-year variations of volume were relatively small compared to those in longer time scales and the seasonal variations. The volume changes in different latitudes were quite homogenous, whether in phase time and in amplitude, with a zero lag (Figure 4.4 b). The thickness anomalies between different layers were also consistent with each other on the time scale. However, those on lighter layers were weaker and earlier, while those on denser layers were stronger and more dominant in the total variations with a delay of about 1 year (Figure 4.4 c). The results indicated that the thickness anomalies in the entire ESTMW were caused by changes in low-frequency, while the upper part of ESTMW was also influenced by high-frequency disturbances.

Furthermore, the relationship between the thickness changes and the winter outcropping was investigated. The latitudinal ranges of the outcrop region and the area-mean MLD are shown in Figure 4.10. In the formation region of STMW (Figure 4.10 a), the winter MLD was shallow, and the outcrop area was small further north in 2006, 2009, and 2016, accompanied by a decrease in the total volume of STMW in the following year. This was consistent with the correlation between the wintertime mixed layer south of the KE and the STMW thickness at 137°E reported by Kobashi et al. (2021). However, in the years with a shallow MLD but a wide outcrop region (2014-2015) or those with a narrow outcrop region but a deep MLD (2005 and 2011), STMW volume did not decrease. The results indicated that both a thick (thin) mixed layer and a wide (narrow) outcrop area were responsible for the more (less) formation of the STMW, and they can cancel each other. The correlation was also applicable to the core isopycnal layer of the STMW (Figure 3.14 a). The MLD near the outcrop line of $\gamma = 25.3$ was small (large) in 2006-2009 and 2016 (2004 and 2011), during which the isopycnal thickness decreased (increased). As a result, the thickness in the following year of each period reached a relative trough (peak). The above results suggested the role of the interannual variability of late winter buoyancy loss.

The above relationship in CMW and ESTMW was not as good as in STMW. In the formation region of CMW, a deeper (shallower) MLD was accompanied by a wide (narrow) outcrop area during 2004-2005, 2010-2011, and 2014-2015, and the conditions were opposite between different longitude ranges during 2009, 2012-2013, and 2016-2017 (Figure 4.10 b). Thus, it is difficult to investigate the correlation between the total volume of CMW and the changes in the entire outcrop region. However, the total volume of CMW and the grid number that meets the criteria of CMW, which indicated the total area of the subducted low Q water, showed a good correlation. Meanwhile, along the outcrop line of $\gamma = 26.3$ (Figure 3.14 b), the shallower (deeper) MLD was accompanied by a decrease (increase) of thickness in 2011, 2015 (2013), but was not in 2014 (2004 and 2006), suggesting a weaker correlation in CMW than in STMW.

A shallow (deep) mixed layer and a narrow (wide) outcrop area in the formation region of ESTMW in 2004, 2011, and 2015-2016 (2009 and 2013) were accompanied by a small (large) volume of ESTMW in the same years instead of a decreasing (increasing) (Figure 4.10 c). The correlation in other years was not clear. Similar results were observed between the thickness anomalies of the $\gamma = 25.0$ isopycnal and the latitudinal position of its outcrop line (Figure 3.14 c). The results suggested that the mechanisms by which MLD influenced the thickness are most likely different in the ESTMW and in both the STMW and the CMW.

4.4 Spatial patterns of thickness anomalies

Annual mean thickness anomalies of three selected layers are shown in Figure 4.6 and Figure 4.8. In the western subtropics on the core surface of STMW (Figure 4.6), the propagation of the thickness anomalies had a much larger westward component compared to that of the spiciness anomalies (Figure 3.7). A negative (positive) thickness anomaly appeared initially right in the formation region of STMW in 2006 (2011), propagated along the inner side of the streamlines, reached the southwestern part of STMW and the western boundary in 2008-2009 (2013-2014), and diminished from the northeast to the southwest sides during 2010-2011 (2015-2016). Because of the large westward component of the propagation, the thickness anomalies did not reach the southeastern part of STMW.

In the eastern subtropics, a positive (negative) thickness anomaly appeared initially north of the outcrop line in 2005 (2013) and spread clockwise to the domain of ESTMW in 2008 (2015-2016) (Figure 4.7). At the same time, the positive (negative) anomaly also spread westward directly to the central latitudes along the outcrop line in 2007 (2015) and united with the anomaly with the same signal near the outcrop line in the western subtropics in 2009-2010 (2016-2017). Unlike the spiciness anomalies that propagated clockwise all the way along the geostrophic currents and arrived at the western basin in the tropics, the thickness anomalies had a larger westward component and a weaker southward component. They decayed rapidly across the domain of ESTMW. As a result, the thickness anomalies generated in the eastern subtropics arrived in the western subtropics and did not reach the tropics. The above results suggested that the thickness anomalies in the western subtropics around STMW were influenced by both the anomalies generated in the STMW formation region in higher latitudes and the anomalies propagated from the eastern subtropics in lower latitudes.

On a denser isopycnal, $\gamma = 26.30$, which is the core surface of CMW, the region with the strongest thickness anomalies was near the boundary between the subtropical and the subpolar gyres all the time, centered at the central latitudes (Figure 4.8). The thickness anomalies mixed with the noisier surrounding anomalies and did not show clear propagations.

To understand the differences between the volume variations of the entire density range of a mode water and those of a thin isopycnal layer, vertical-zonal sections of the thickness anomalies were shown in Figure 4.9-1 and 4.9-2, averaged in 25-30°N and 30-35°N respectively. In the western basin in 25-30°N, the layer $\gamma = 24.8-25.7$ showed thickness anomalies of different signs on its different parts every year. In most of the years, thickness anomalies centered at $\gamma = 25.0$ and those centered at $\gamma = 25.5$ showed opposite signs. Only in 2012 and 2017, thickness anomalies at $\gamma = 25.0$ and $\gamma = 25.5$ have an identical sign, with

anomalies of opposite sign occurring between them on $\gamma = 25.3$. The above anomalies in 25-30°N were following those of the same longitudes in 30-35°N in most years, but the vertical pattern in 30-35°N in 2016 appeared in 25-30°N in 2017. The results were consistent with the different volume changes between the light and dense parts of STMW (Figure 4.3). They suggested that the thickness anomalies in the STMW distribution region were most likely caused by the formation of STMW with different density proportions.

At the lower part of ESTMW (25-30°N, west of 160°S, centered at $\gamma = 25.0$), thickness anomalies were synchronized with those at the upper STMW, except for 2004, 2012 and, 2013 (Figure 4.9-1). The two have a similar density range, suggesting a simultaneous change of the layer $\gamma \sim 25.0$ in western and eastern subtropics. However, this synchronized change was less clear in 30-35°N, and was not shown in 2004-2005, 2012-2013, and 2016. Further work was needed to determine the causes.

4.5 Propagation direction and velocity of thickness anomalies

Similar to the methods used in spiciness anomalies in Figure 3.10, Figure 3.11, and Figure 3.12, we also traced the thickness anomalies on core γ surfaces of the mode waters along the mean streamlines (Figure 4.11, Figure 4.12, and Figure 4.13). Because the thickness anomalies observed were noisier than the spiciness anomalies, both the monthly anomalies and the 12-month running averaged anomalies were shown.

Along the streamline goes through ESTMW (Figure 4.11), seasonal variations of thickness were dominated from north of the outcrop line to 1500 km south of the outcrop line, had a more sustainable impact compared to those in salinity anomalies, which were dominated only north of the outcrop line. The interannual variations, however, decayed much more rapidly in thickness than in spiciness anomalies. They lost much of the amplitude after went across south of Hawaii (points 5-6), where Q increased a lot along the streamline (Figure 3.2). The decay of interannual variations in the domain of STMW, where the mean gradient of Q along the streamline was smaller (Figure 3.2), was slower (Figure 4.12). The results indicated the effect of the mean spatial gradient on the temporal variations in thickness. It can also be related to diapycnal and isopycnal mixing/diffusion (e.g., Abernathey et al., 2016; Cerovecki et al., 2013; Downes et al., 2011; Speer & Tzipermann, 1992; Speer & Forget, 2013; Tzipermann, 1986).

Based on the conservation of potential vorticity, thickness anomaly is not a conserved tracer because of the effect of Coriolis parameter. So we also showed panels for a conserved tracer, anomalies of potential thickness (PT) (Figure 4.11 d and e). The definition of PT is adopted from Yasuda (2003), calculated by thickness between two isopycnals divided by the

normalized Coriolis parameter $f(\theta)/f(45^\circ\text{N}) = \sin\theta/\sin(45^\circ\text{N})$ (θ is latitude). Though the decay of PT anomalies was weaker than that of thickness anomalies (Figure 4.11 b-c), it was still more rapid than the spiciness anomalies. So the conclusion of different processes between the transport of spiciness anomalies and thickness anomalies are also applicable here.

The propagation speed of thickness anomalies was comparable with the geostrophic speed along the eastern path (Figure 4.11) but was faster than the geostrophic speed along the western path (Figure 4.12). Notably, the propagation speeds of thickness anomalies along the streamlines were lower than that of spiciness anomalies, despite the propagation pathway to the further inner side of the streamline in thickness anomalies than in spiciness anomalies shown in the annual anomaly maps (Figure 3.7 and Figure 4.6). Besides, the low-frequency anomalies south of the outcrop line showed a shorter period and an earlier phase in thickness anomalies than in spiciness anomalies (further discussions in section 4.6). The results implied that the dominant processes on the propagation of thickness anomalies and spiciness anomalies are different.

The lower propagation speed in thickness anomalies than in spiciness anomalies had also been observed on $\gamma = 26.8$ and 27.2 by Kouketsu et al. (2017). They suggested that the thickness anomalies were influenced more by Rossby waves, and the spiciness anomalies were influenced by the geostrophic currents. The results in Chapter 4 suggested that the spiciness anomalies in the density ranges of this study were mainly propagated by geostrophic currents, but future work was needed to examine the influence of wave dynamics on the propagation of thickness anomalies.

On the surface $\gamma = 26.3$, the thickness anomalies were much noisier than spiciness anomalies (Figure 4.13). Along the streamline in the subtropical gyre (Figure 4.13 b and c), low-frequency thickness anomalies were dominated only in the points of 1-5, and after the geostrophic direction changed from eastward to westward near 30°N , thickness anomalies were dominated by monthly variations, and the continuous propagation of the low-frequency signals were not observed after that.

Along the streamline in the subpolar gyre (Figure 4.13 d and e), the seasonal variations dominated from the east of Japan to 150°W (points 0-6), covered a longer distance than that in spiciness anomalies, which was to 170°W . The seasonal signals were homogenous in sign and amplitude along the way. They occurred initially almost at the same time in $140\text{-}175^\circ\text{E}$ (points 0-3), which was near the outcrop line. The anomalies then reached 150°W within 1-year, propagated at a speed ~ 3 times the geostrophic speed, and decayed rapidly only after went across 160°W . The downstream east of 160°W was dominated by low-frequency thickness

anomalies with a time scale of 4 years, shorter than that of the spiciness anomalies. From the low-pass filtered panel, the low-frequency signals in the downstream occurred initially near 175°W (point 4) and propagated eastward at speed slightly faster than the geostrophic currents. There were also low-frequency signals observed near 175°E (point 3) but with a time scale of 6 years and were separated from those in the east. They showed westward propagation in some years, but the propagation was not very clear. The above results suggested that the seasonal thickness anomalies near the gyre boundary were generated near the outcrop line in the western basin, while the interannual variations of 4-6 years were generated in the central latitudes by different mechanisms. The thickness anomalies with a 4-year time scale generated east of the date line were propagated mainly by the geostrophic currents, while those with a 6-year time scale generated west of the date line and the seasonal variations were propagated by other processes.

4.6 Relations of spiciness and thickness anomalies with KEI and PDO

The decadal variability of STMW salinity on its core surface ($\gamma = 25.3$) is highly consistent with the decadal variability of KE between a stable and an unstable dynamic state (Qiu and Chen, 2005; Qiu et al., 2014; Qiu et al., 2021): KE index (KEI) changed to negative (positive) in 2005 (2009), which indicates KE became unstable (stable), and salinity in STMW on its core surface ($\gamma = 25.3$) began to decrease (increase) in 2006 (2010) (Figure 4.14 a). This can be explained by more fresh/cool water transported from north of the KE to the STMW formation region accompanied by high eddy activity and further north position of KE during an unstable KE state (Oka et al., 2017). Through lagged-correlation analysis, we found KEI lead salinity change rate of STMW for 7~12 months with shorter lag on lighter layers and in a northern region. The lag from KEI to the change rate of STMW total salinity is 1 year at $R = 0.65$. This correlation coefficient is similar to that Oka et al. (2017) reported between the annual-mean KE index and the annual change of the winter mixed layer salinity at 30-35°N, 144°E during 1993-2015 ($R = 0.63$), but their result is without time lag. We also calculated with latitudes confined in 30-35°N and still found lags for several months. The above results, combined with the good correlation between salinity in the winter mixed layer and the salinity in STMW, imply that KE state variability generates salinity anomalies directly in the winter mixed layer, and the signals are then subducted and advected to the distribution region of STMW within 1 year from lighter surface to denser surface.

As STMW salinity decreases during an unstable KE period with a lag, the total thickness of STMW also decreases with a negative KE index. The correlation between the KE index and

the STMW thickness tendency is of zero lag in total, being -1.5, 0.5, and 1 year in 30-35°N, 25-29°N, and 20-24°N. The negative lag likely suggested that the dynamic state of KE and the stratification in the density range of STMW in 30-35°N had a common factor, but the latter responded faster. The positive correlation between the KE index and the STMW thickness tendency at the zero lag, instead of the STMW thickness, supports the argument that the STMW volume decreases during unstable KE period (Qiu and Chen, 2006; Miyazawa et al., 2009; Sugimoto and Hanawa, 2010) and is disagreement with that the STMW volume being small during unstable KE (Oka et al., 2015).

As the further north position of KE and more eddy activities during an unstable KE state can transport negative spiciness anomalies southward to STMW, they may also transport warm and salty water northward to CMW formation region, which has been hypothesized by Suga et al. (2012) on the late 1980s regime shift. Also, Oka et al. (2012) suggested that L-CMW production in western part of formation region is high during unstable KE due to more low Q water transported from southward by eddies. These previous results suggest a negative correlation of the KEI with the tendency of CMW salinity and the L-CMW volume. However, no clear correlation between them were found at zero lag (Figure 4.15). This is likely due to that the volume of CMW formed in its western formation region just north of the KE was compared to the entire CMW volume. Instead, the KEI and the CMW salinity tendency showed negative correlation ($R = -0.4$) at lag = 3-4 years. KEI and CMW thickness tendency showed a weak negative correlation ($R = -0.2$) at lag = -1.5 years. These results are likely related to the transport of the anomalies of temperature, stream function and mixed layer depth originated at the central North Pacific related to PDO to the KE system in 3–5 years (Schneider et al., 2002; Deser 1999; Oka et al., 2015), but further investigation was needed to examine it.

The four parameters indicating KE variabilities showed different contributions on between STMW and CMW, and between salinity and thickness anomalies (Figure 4.16), indicating the influences through different mechanisms. The upstream KE path length and the KE strength are important for both the STMW salinity and thickness tendencies. The upstream KE position is important for STMW thickness but is less important for STMW salinity. The recirculation gyre strength has the largest correlation with STMW salinity, but is less important for STMW thickness. CMW showed clear correlations with recirculation gyre strength and KE position, but those for the KE length and strength are weak.

PDO had a significant phase shift from negative to positive in 2014 (Figure 4.17), after which the CMW volume increased and the CMW salinity decreased. This is consistent with the correlations between CMW and the climate shifts that revealed by previous studies during the

climate shifts in 1976/77 and 1988/89 or in models (Yasuda and Hanawa, 1997; Suga et al., 2003; Qu and Chen, 2009; Chen et al., 2010; Toyama, 2015). However, the correlation between the time series of PDO and CMW was not good. The time change rates of CMW salinity did not show a significant correlation with PDO index at zero lag, but showed a weak correlation ($R = 0.4$) at lag = 1.5–2 years and a negative correlation ($R = -0.4$) at lag = -1–-2 years (positive lags indicate PDO leads water mass properties). The CMW thickness tendency showed a weak positive correlation ($R = 0.3$) with PDO index at a zero lag, and it caused a high correlation between CMW thickness and PDO ($R = 0.8$) at lag = 1.5 years. This indicated that though the regime shift of PDO can cause abrupt changes in CMW properties, the impact of PDO related processes on salinity changes on interannual timescale is limited. From the time lags, the variability of CMW and PDO leads that of KE, and the correlations of CMW with KEI and PDO index were opposite. It may related to the process suggested by previous studies that the signals during positive PDO period are generated in central North Pacific and are propagated westward to KE, making it unstable with a ~3 years lag (Newman et al., 2016; Joh and Di Lorenzo, 2019).

The correlations between ESTMW and PDO are opposite to that of CMW, both in their thickness and the thickness tendencies. ESTMW thickness tendency and PDO showed a negative correlation ($R = -0.3$) at zero lag, and ESTMW thickness and PDO showed a negative correlation ($R = -0.8$) at lag = 1 year. This is consistent with the anti-correlated variability in the subduction rate between central and eastern subtropics in the North Pacific suggested by Chen et al. (2010) using OGCM and by Toyama (2015) using Argo data during 2005-2012, and is also consistent with the negative correlation between ESTMW thickness and PDO index at 1-year-lag reported by Guo et al. (2018) and Katsura (2018). As previous studies explained the subduction rate changes in CMW and ESTMW regions related to PDO mainly by MLD anomalies, we found opposite MLD anomalies between the western to central and the eastern parts of the outcrop region (Figure 4.10) in some years with extreme changes but their corresponding relations were not good enough to explain the subsurface thickness anomalies.

Previous studies also suggested a positive correlation between the subduction rate in STMW region and PDO at a lag of a few years (Qiu and Chen, 2005; Oka et al., 2015; Toyama, 2015). However, we did not found this positive correlation between PDO and STMW total volume or its tendency, consistent with the result suggested by Hu et al. (2011) in models. Nevertheless, the thickness tendency of the lighter part of STMW ($\gamma = 25.00-25.20$) showed weak positive correlation with PDO index at lag = 1 year. Combined with the positive correlation between the thickness tendency of the lower part of ESTMW ($\gamma = 24.85-25.15$) and

the PDO at lag = 2 years, it may explain the almost simultaneous thickness anomalies between STMW and ESTMW in Figure 4.9. But further studies are needed to clarify the processes. Besides, salinity change rate of STMW and ESTMW showed opposite correlations with PDO at lag = 1 year.

4.7 Conclusions and discussions

In this chapter, thickness anomalies and their propagation in the upper North Pacific were investigated during 2004–2018 via Argo profiles, focusing on the three mode waters (i.e., STMW, CMW, and ESTMW).

The total volume of STMW was dominated by decadal variability. Compared to spiciness anomalies, the thickness anomalies in STMW have a higher frequency and a faster propagation speed from the formation region to the entire STMW. The denser and lighter parts of STMW showed different anomalies in some years, implying the variation of the formation of different proportions.

In CMW, total volume decreased with a quasi-decadal variability. The phase of the decadal variability was later in volume than in salinity, different from that in STMW. The volume changes of CMW showed good consistency between different latitudes, different from the year-to-year variations of salinity confined only to the northern part, which were related to spice injection. It suggested that the volume change of CMW was most likely caused by stratification change. A distinct separation between the volume change between L-CMW and D-CMW was not found, probably because the formation region of CMW was too wide to cause a local influence between different isopycnals.

The volume of ESTMW showed a quasi-decadal variability with a rapid shrinking in 2010–2011. The thickness anomalies in the entire ESTMW were caused by changes in low-frequency, while the upper part of ESTMW was also influenced by high-frequency disturbances.

The volume changes of mode waters were consistent with the changes in the winter mixed layer. A thick (thin) mixed layer and a wide (narrow) outcrop area were responsible for the more (less) formation of STMW, and they can cancel each other. The correlation was also applicable to the core isopycnal layer. The results indicated the dominant role of the interannual variability of later winter buoyancy loss. This relationship was also shown in some years in both CMW and ESTMW but was not as good as in STMW.

The propagation of the thickness anomalies had a much larger westward component and a smaller southward component compared to that of the spiciness anomalies. This is observed in both western and eastern subtropics. As a result, the thickness anomalies generated in the

STMW and ESTMW formation region did not reach the southeastern part of STMW and the western tropics, respectively.

Along the streamline goes through ESTMW (Figure 4.11), seasonal variations of thickness had a more sustainable impact compared to those in salinity anomalies. The interannual variations, however, decayed much more rapidly in thickness than in spiciness anomalies. Besides, the propagation speeds of thickness anomalies along the streamlines were lower than that of spiciness anomalies in the western subtropics, calling for further work on wave dynamics.

On $\gamma = 26.30$, the strongest interannual thickness anomalies were near the boundary between the subtropical and the subpolar gyres all the time, centered at the central latitudes, and did not show clear continuous propagations. Seasonal thickness anomalies near the gyre boundary were generated near the outcrop line in the western basin. In contrast, the interannual variations of 4-6 years were generated in the central latitudes by different mechanisms. The thickness anomalies with a 4-year time scale generated east of the date line were propagated mainly by the geostrophic currents, while those with a 6-year time scale generated west of the date line and the seasonal variations were propagated by other processes.

Vertically, thickness anomalies centered at the range of the light and dense parts of STMW showed opposite signs. Notably, the thickness anomalies at the lower part of ESTMW were synchronized with those at the upper STMW in most of the years. The two have a similar density range, suggesting a simultaneous change of the layer in western and eastern subtropics. Future work was needed to determine the causes.

The relationships between anomalies and KEI and PDO were discussed. STMW showed a positive correlation with KEI in its salinity tendency at lag = 1 year and in its thickness tendency at zero lag, indicated a faster response to KE variability in thickness than in salinity. The correlation between STMW and PDO was weak. The results indicated that the STMW was influenced more by the KE changes directly and demonstrated the western pathway from the KE region to the western subtropics. The correlation between KEI and CMW was only shown in salinity tendency at a lag of -3– -4 years, and the impact of KE on CMW volume change is weak.

The phase shift of PDO from negative to positive in 2014 caused a thicker and cooler CMW, consistent with the correlations suggested by previous studies in 1976/77 and 1988/89 phase shifts. On interannual time scale, CMW showed a high correlation with PDO in thickness at lag = 1.5 years but no meaningful correlation for salinity. On the contrary, ESTMW showed a negative correlation with PDO in volume at lag = 1.5 years, consistent with the anti-correlated subduction rate changes between central and eastern subtropics suggested by previous studies.

No meaningful correlation between STMW total volume and PDO was found, and the 1-year lag between STMW and PDO cannot be explained by the transit time of PDO-related anomalies from the central North Pacific to the KE region. However, the volume tendency of the lighter part of STMW showed a weak positive correlation with PDO at 1 year lag, similar to that in denser part of ESTMW.

While previous studies have investigated the influences of PDO-related activities on the formation region and the volume change of mode waters, few have reported the consequent changes in salinity. This study provides evidence, though limited, that PDO also has a correlation with salinity in mode waters. In previous sections, we found a large-scale freshening and a good agreement between interannual spiciness anomalies in the formation region of STMW and that in the central Pacific, which imply that there is probable a common cause of spiciness anomalies in the whole outcropping region.

The earlier phases of PDO and CMW time series to KE, the synchronized thickness anomalies in the light part of STMW and the dense part of ESTMW, and the anti-correlated variations in CMW and ESTMW volume changes as well as in STMW and ESTMW salinity, call for further investigation on the contributions of large-scale changes on generating signals that occurred initially at the central longitudes related to PDO.

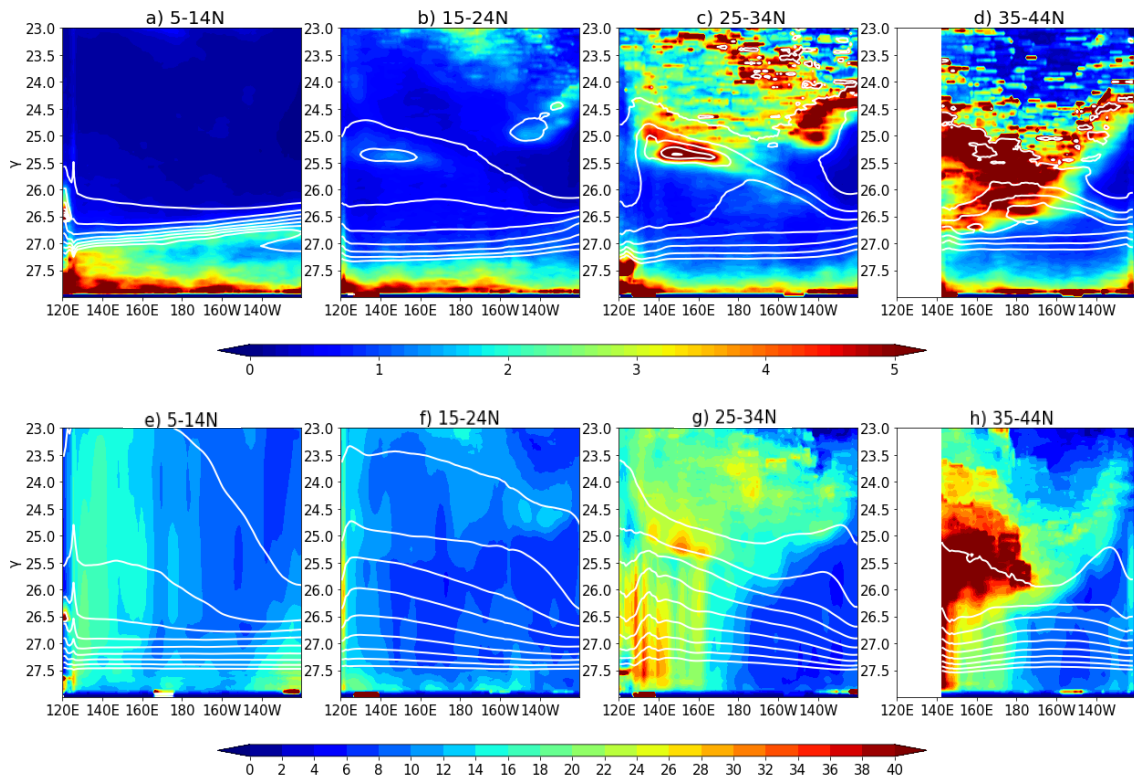


Figure 4.1 Climatology (contour) and standard deviation (color) of isopycnal thickness with respect to neutral density, averaged in (a) 5°-14°N, (b) 15°-24°N, (c) 25°-34°N, and (d) 35°-44°N. (The grids in the Sea of Japan are whitened.) (d)-(g): Same as (a)-(d) but for isopycnal depth.

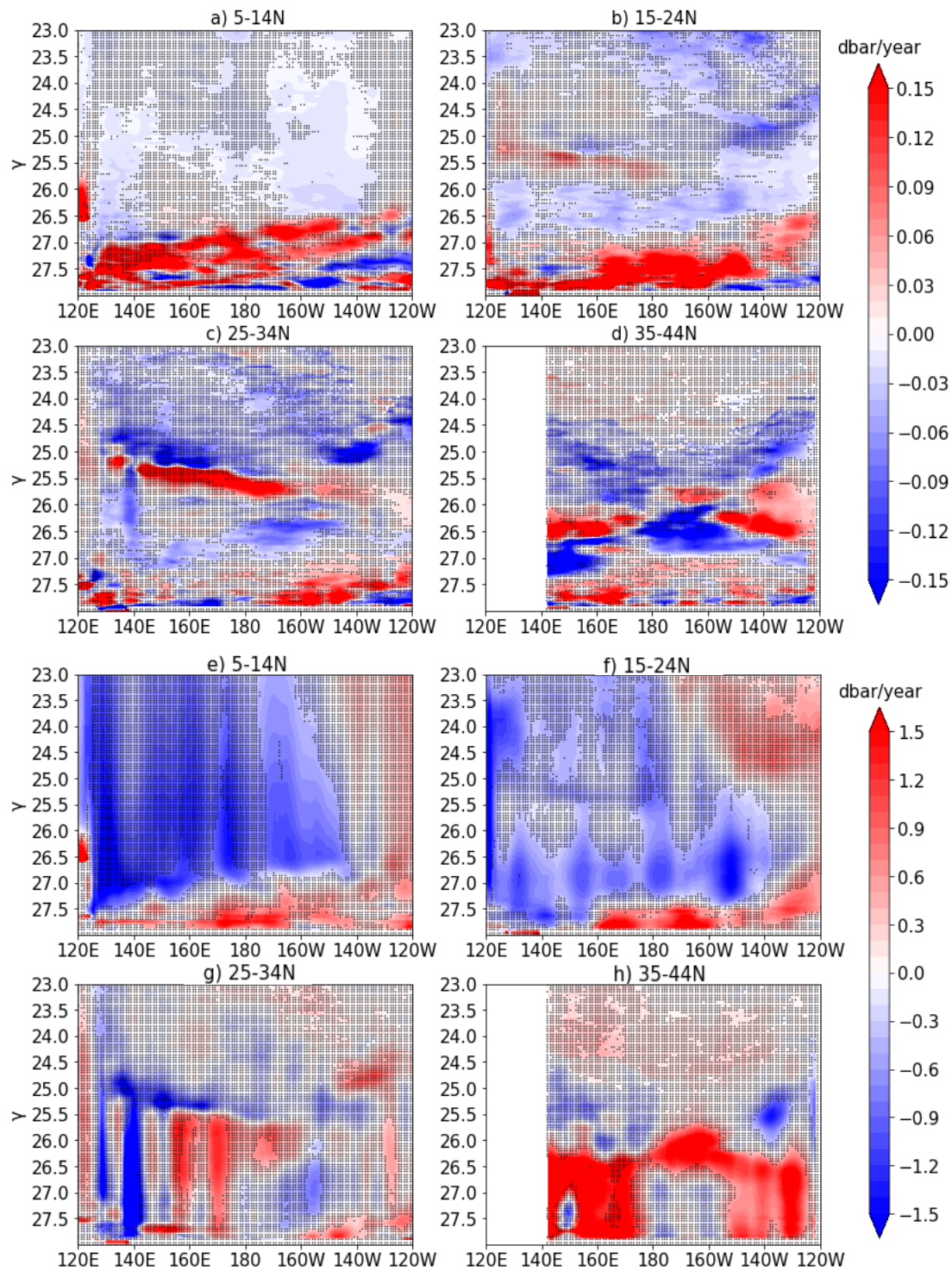


Figure 4.2 Thickness linear trend (color; unit: dbar/year) with respect to γ during 2004-2018, averaged in (a) 5° - 14° N, (b) 15° - 24° N, (c) 25° - 34° N, and (d) 35° - 44° N. Stippled grids indicate where the trend is insignificant at 95% confidence level. (e)-(h): Same as (a-d) but for depth.

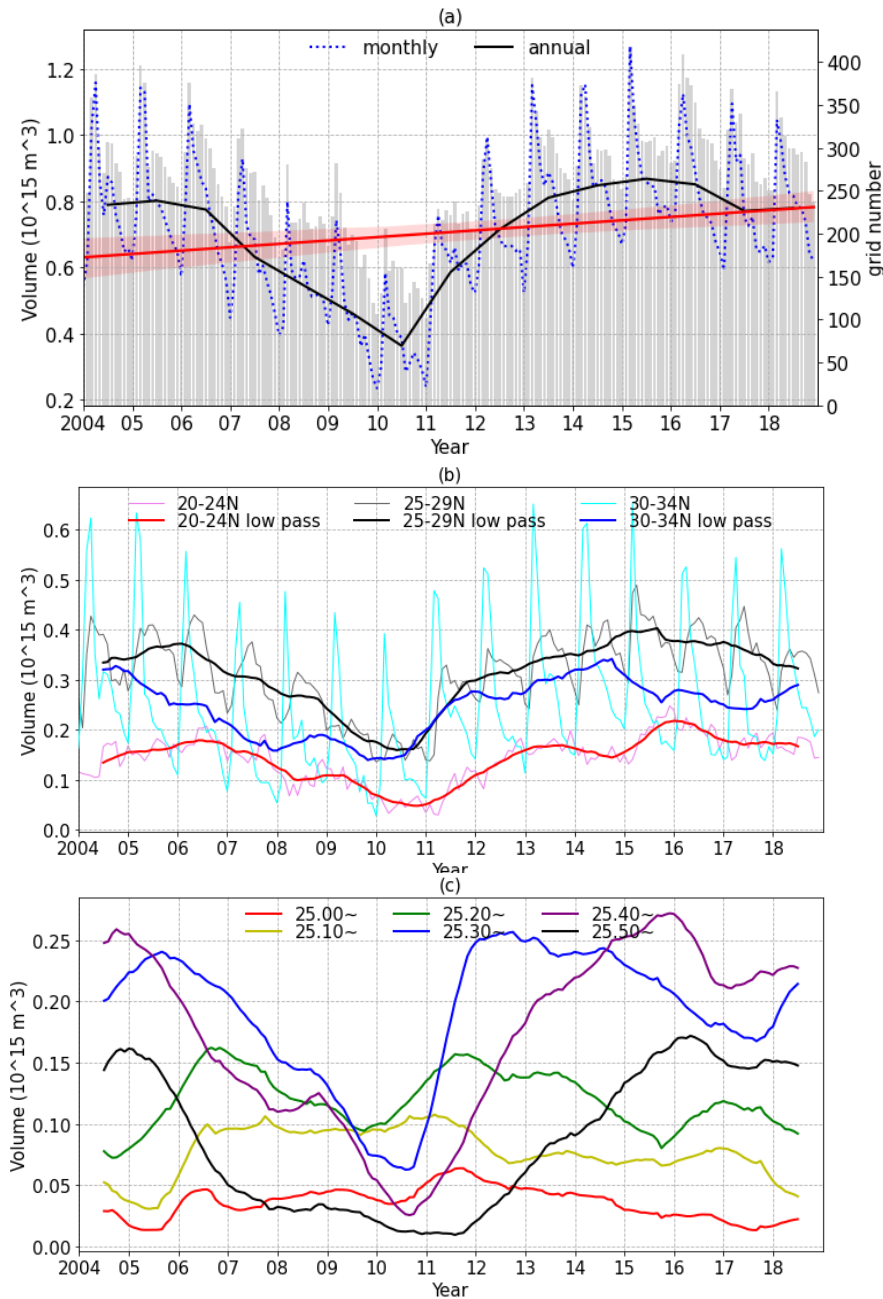


Figure 4.3 Time series of volume (unit: 10^{15} m^3) of STMW: (a) Monthly (dotted blue), annual mean (solid black), and linear trend (solid red) with a 95% confidence interval (red band) of total volume, accumulated from the thickness and horizontal area of each grid box on each γ layer that meets the criteria of STMW of each γ surface. Gray bars represent the average number of $1^\circ \times 1^\circ$ grids that are used on one γ surface. (b) Volume in three latitude ranges: Pink (monthly) and red (12-month moving average) for 20-24°N, gray and black for 25-29°N, and light blue and blue for 30-35°N. (c) 12-month moving average of volume of layers $\gamma = 25.00$ -25.05 (red), 25.10-25.15 (yellow), 25.20-25.25 (green), 25.30-25.35 (blue), 25.40-25.45 (purple), and 25.50-25.60 (black).

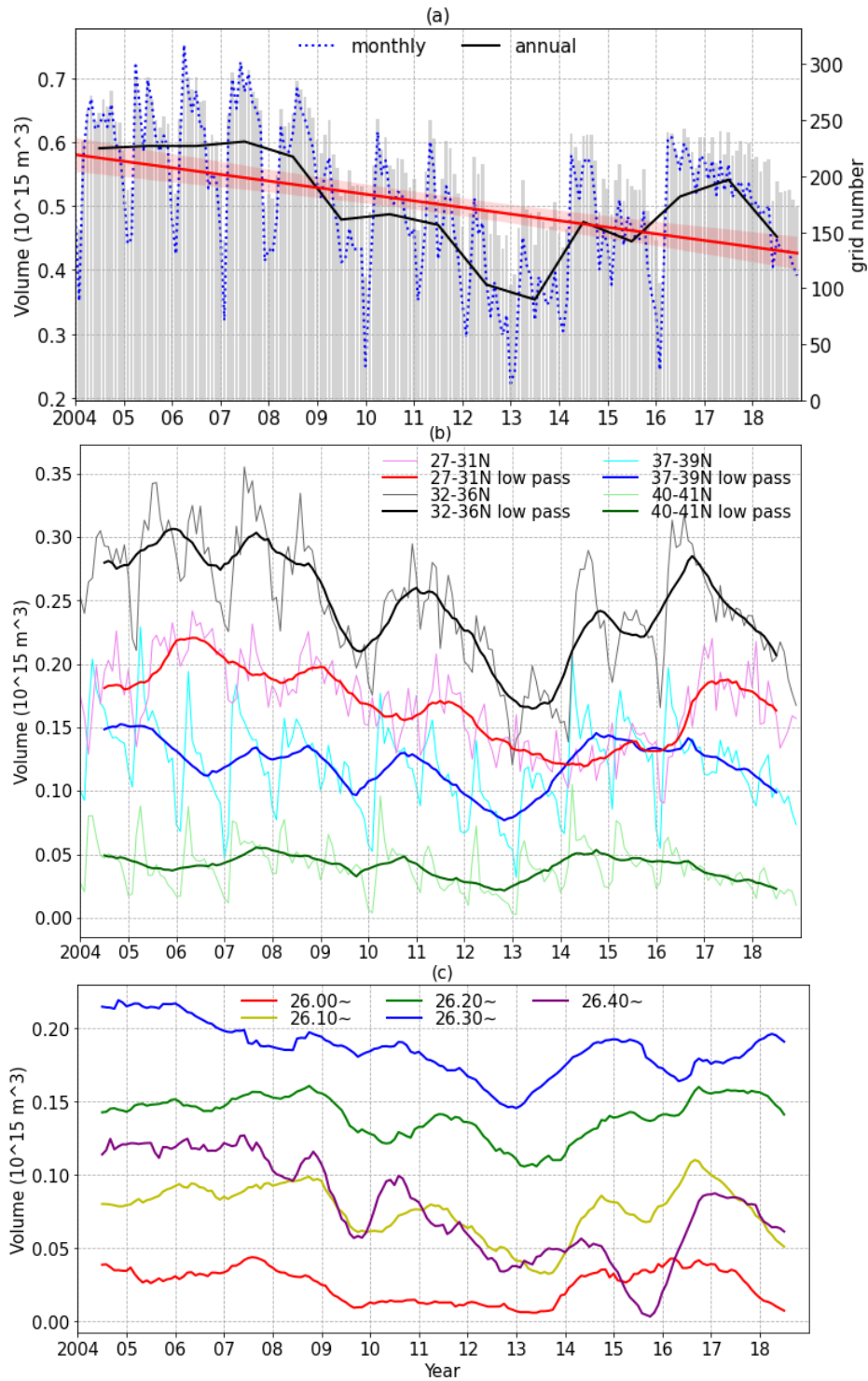


Figure 4.4 Same as **Figure 4.3** but for CMW. (b) In 27-31°N (pink and red), 32-36°N (gray and black), 37-39°N (light blue and blue), and 40-41°N (light green and green). (c) On surfaces $\gamma = 26.00$ -26.05 (red), 26.10-26.15 (yellow), 26.20-26.25 (green), 26.30-25.35 (blue), and 26.40-26.45 (purple).

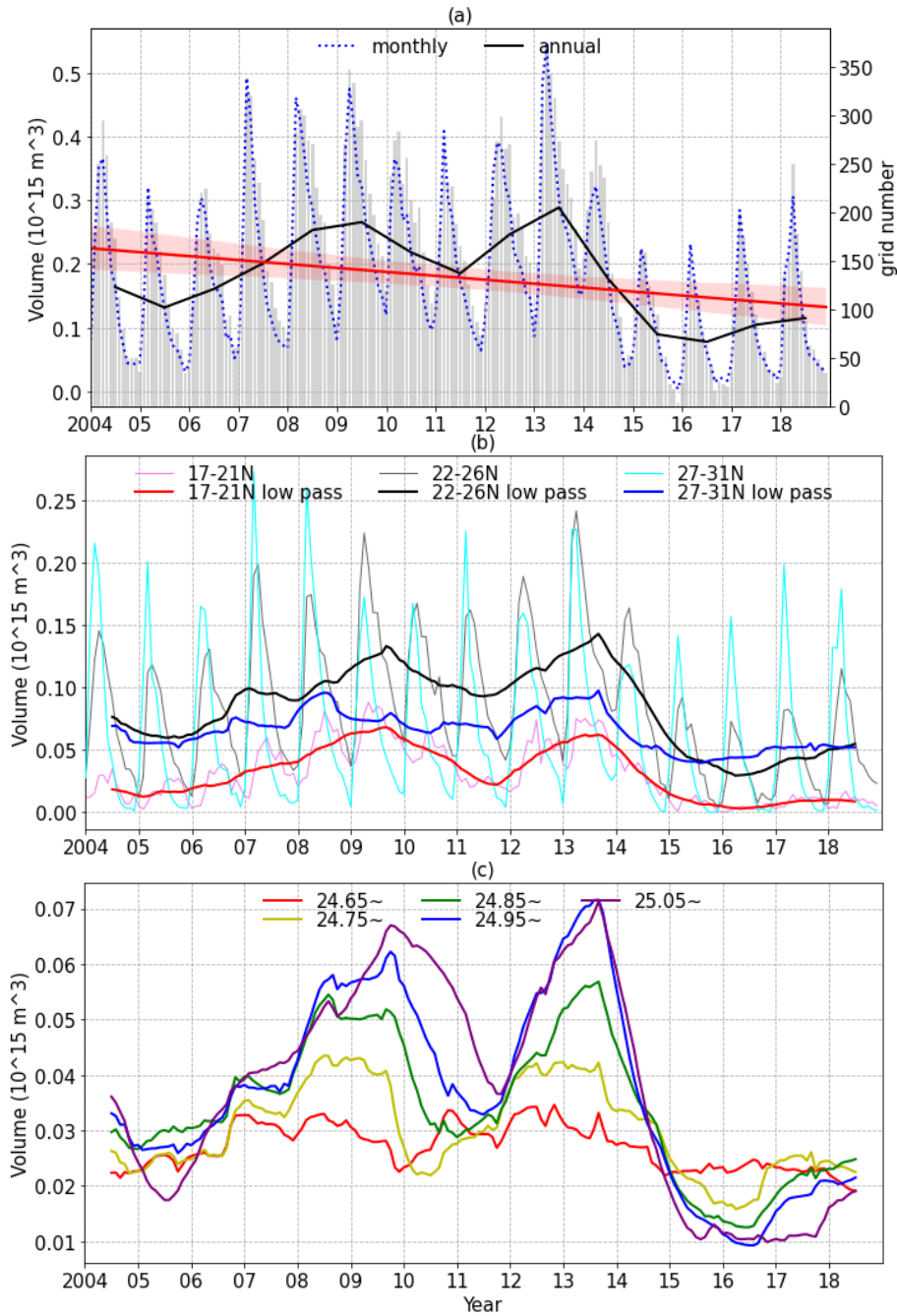


Figure 4.5 Same as **Figure 4.3** but for ESTMW. (b) In 17-21°N (pink and red), 22-26°N (gray and black), and 27-31°N (light blue and blue). (c) On surfaces $\gamma = 24.65$ -24.70 (red), 24.75-24.80 (yellow), 24.85-24.90 (green), 24.95-25.00 (blue), and 25.05-25.15 (purple).

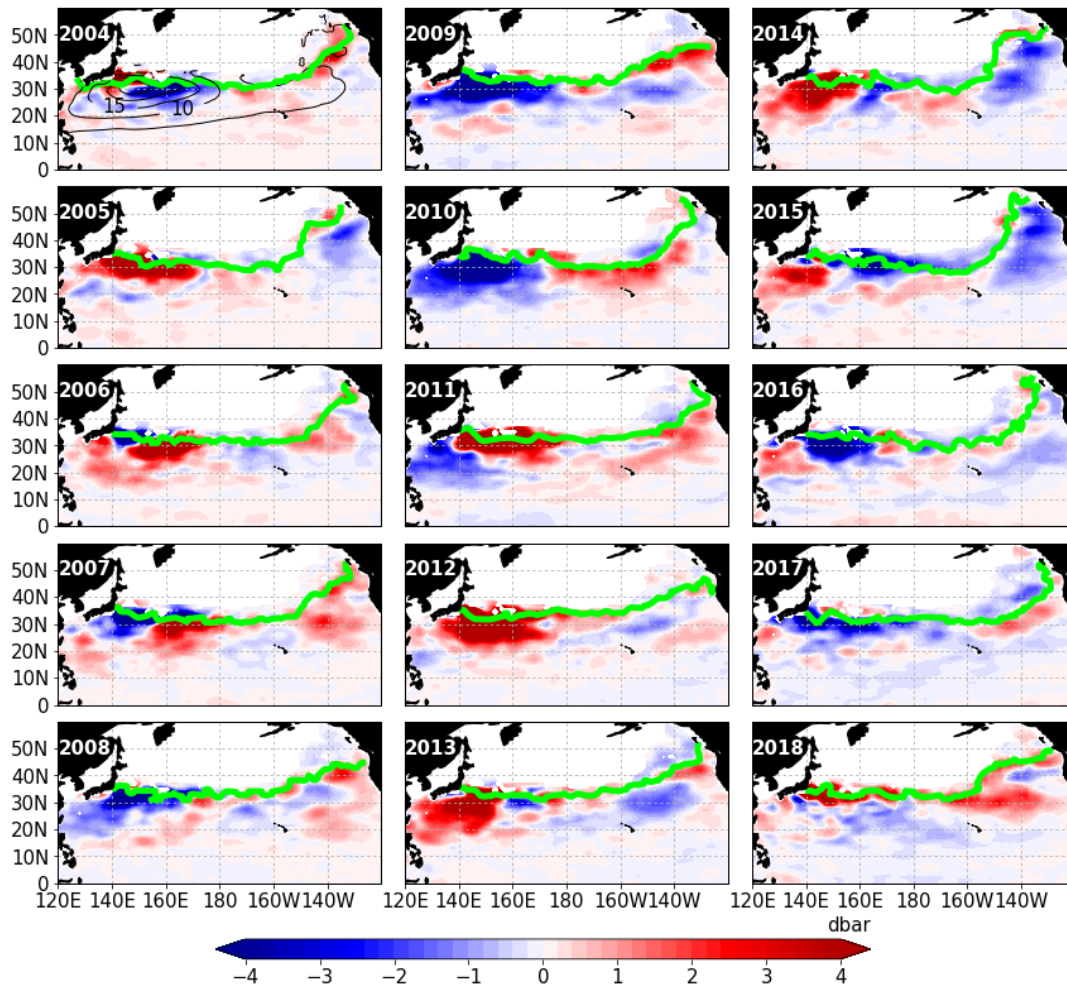


Figure 4.6 Annual mean thickness anomalies of layer 25.3 (± 0.025) γ . Black contours in the subplot of 2004 denote the climatological thickness with intervals of 5 and labels of 10 and 15. Light green lines denote the late winter outcrop line averaged in February and March of each year.

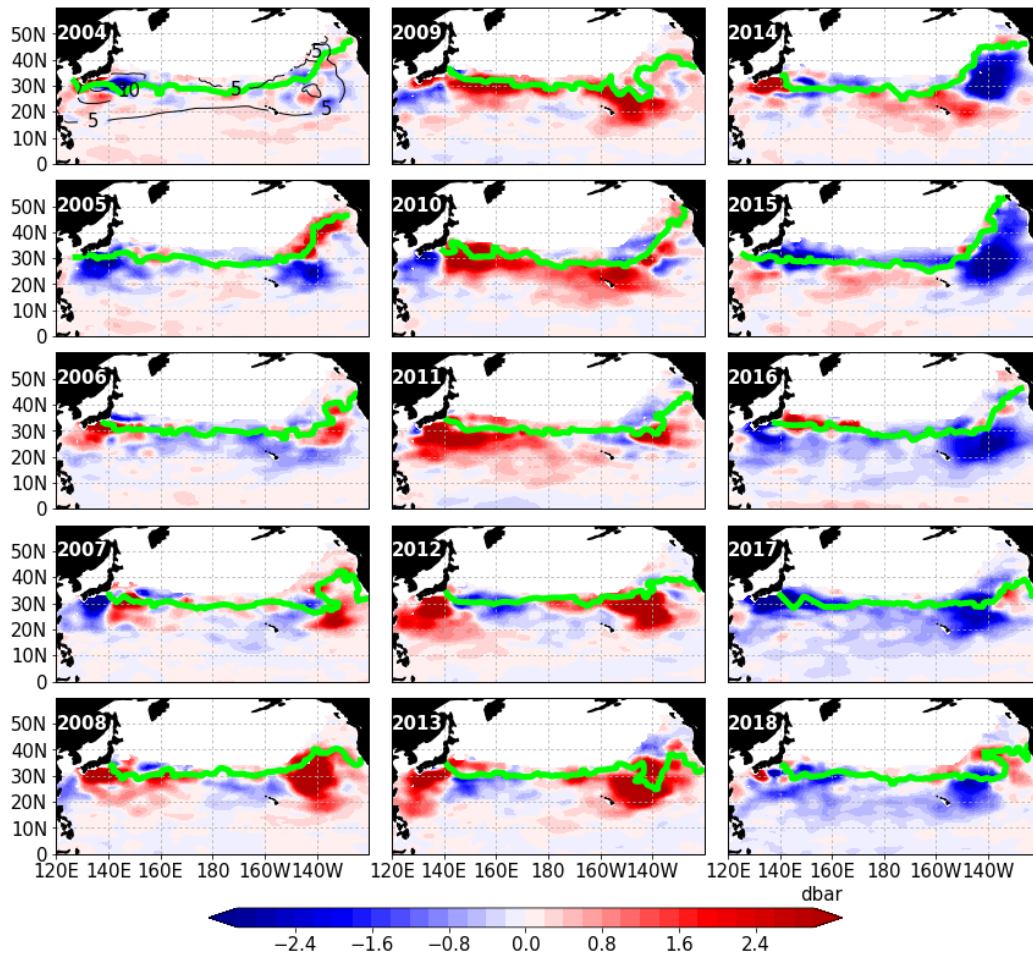


Figure 4.7 Same as **Figure 4.6** but for 25.00γ .

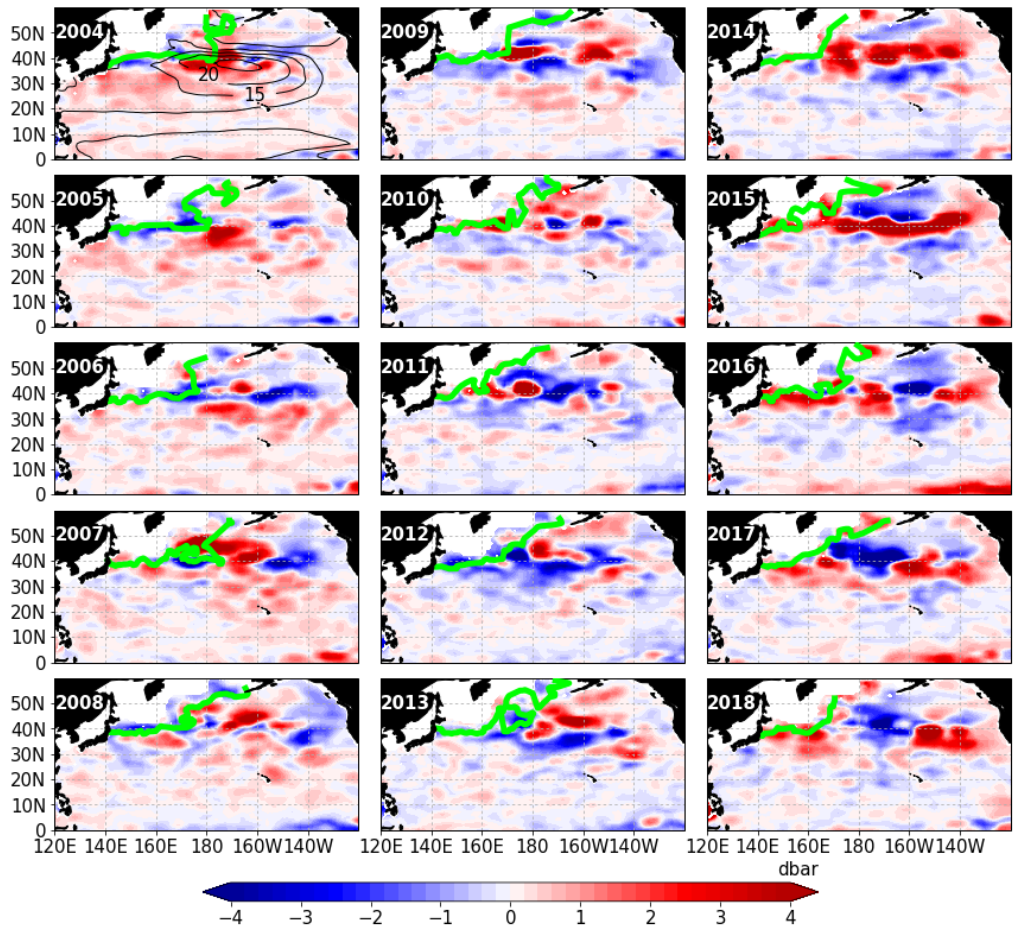


Figure 4.8 Same as **Figure 4.6** but for 26.30 γ .

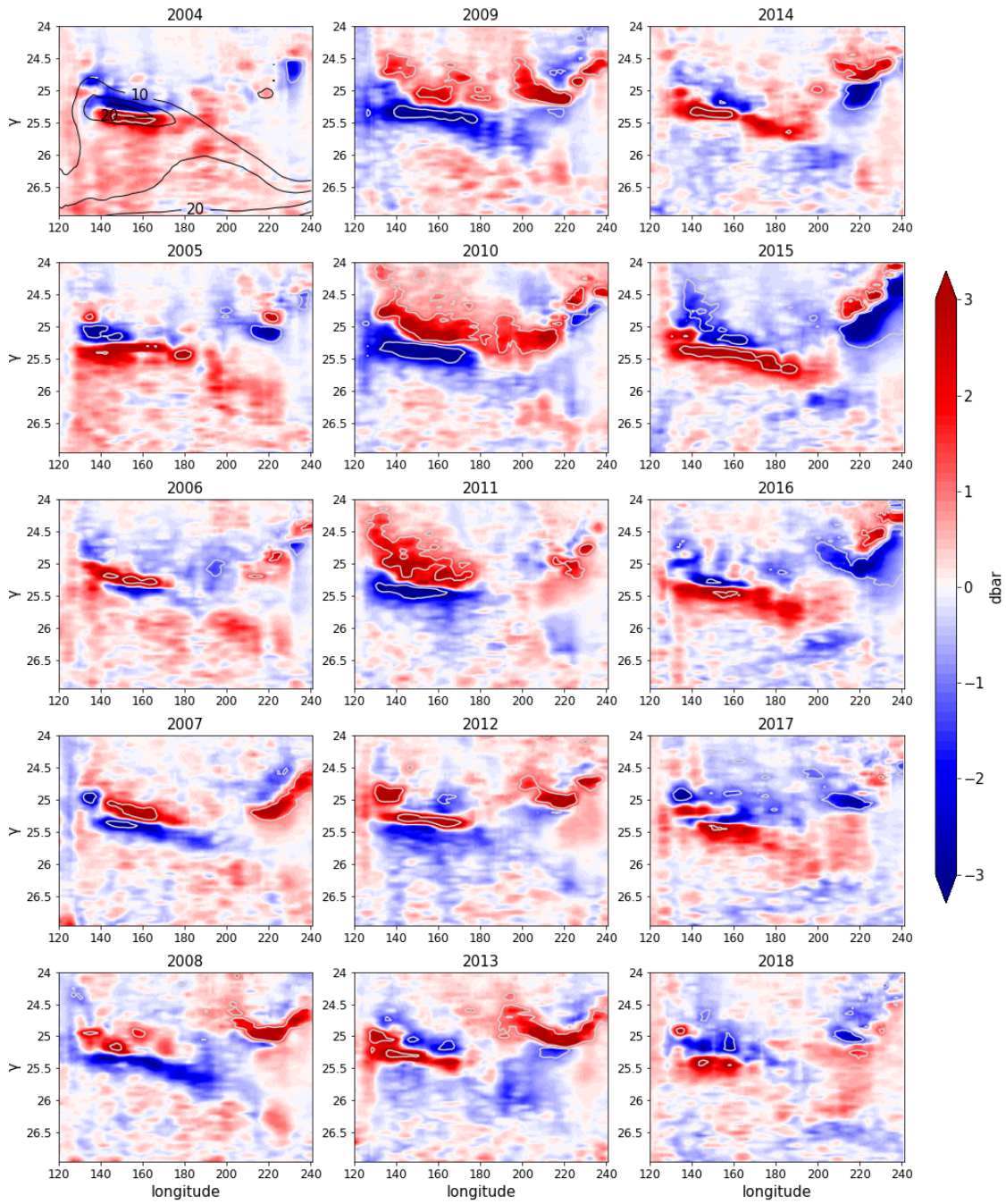


Figure 4.9-1 γ -longitude sections of annual mean thickness anomalies (units: dbar) averaged in 25-30°N. Gray contours denote the relative anomalies (anomalies divided by climatological thickness) larger than 20%.

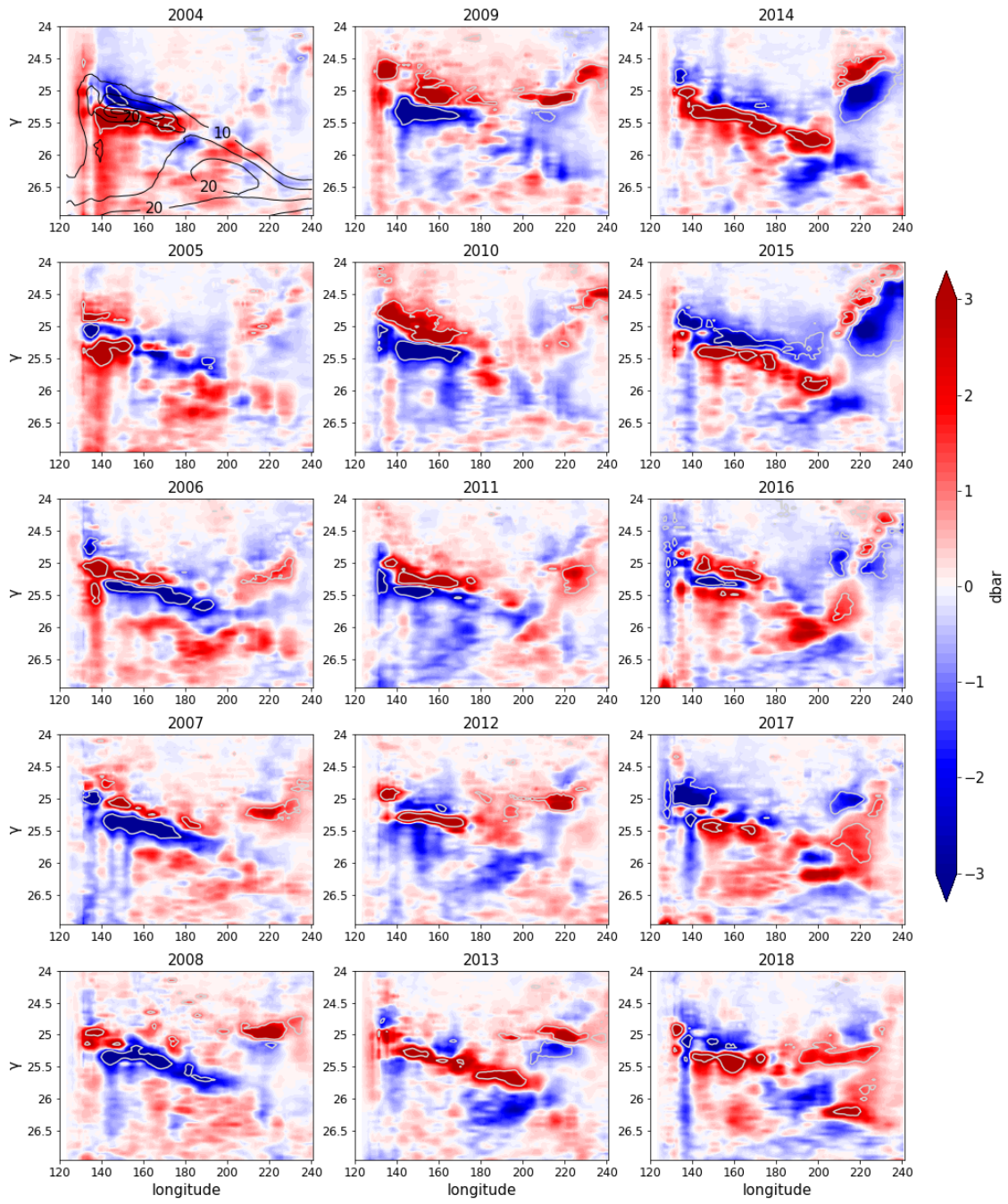


Figure 4.9-2 Same as **Figure 4.9-1** but averaged in 30-35°N.

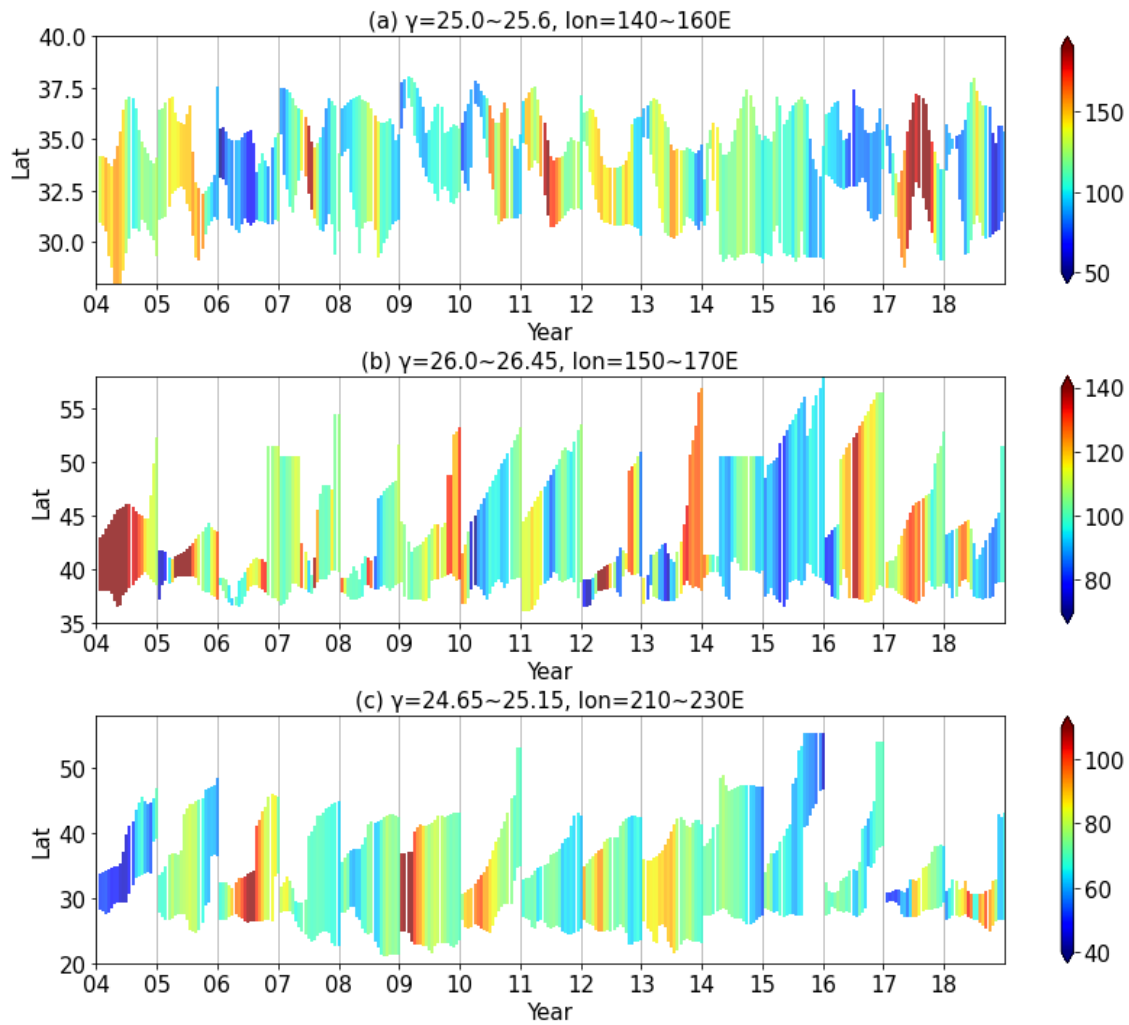


Figure 4.10 Plots for the latitude ranges of the winter outcrop region of the isopycnals in the formation region of the mode waters. (a) $\gamma = 25.00\text{-}25.60$ in $140\text{--}160^\circ\text{E}$, (b) $\gamma = 26.00\text{-}26.45$ in $150\text{--}170^\circ\text{E}$, and (c) $\gamma = 24.65\text{-}25.15$ in $130\text{--}150^\circ\text{W}$. The latitude range was calculated at each longitude from the latitudinal positions between the outcrop lines of the densest and the lightest isopycnals of each density range. Horizontal positions of the lines in each year are distributed from the west to the east from left to right. Colors of the lines indicate the MLD averaged in the outcrop latitudes at fixed longitudes.

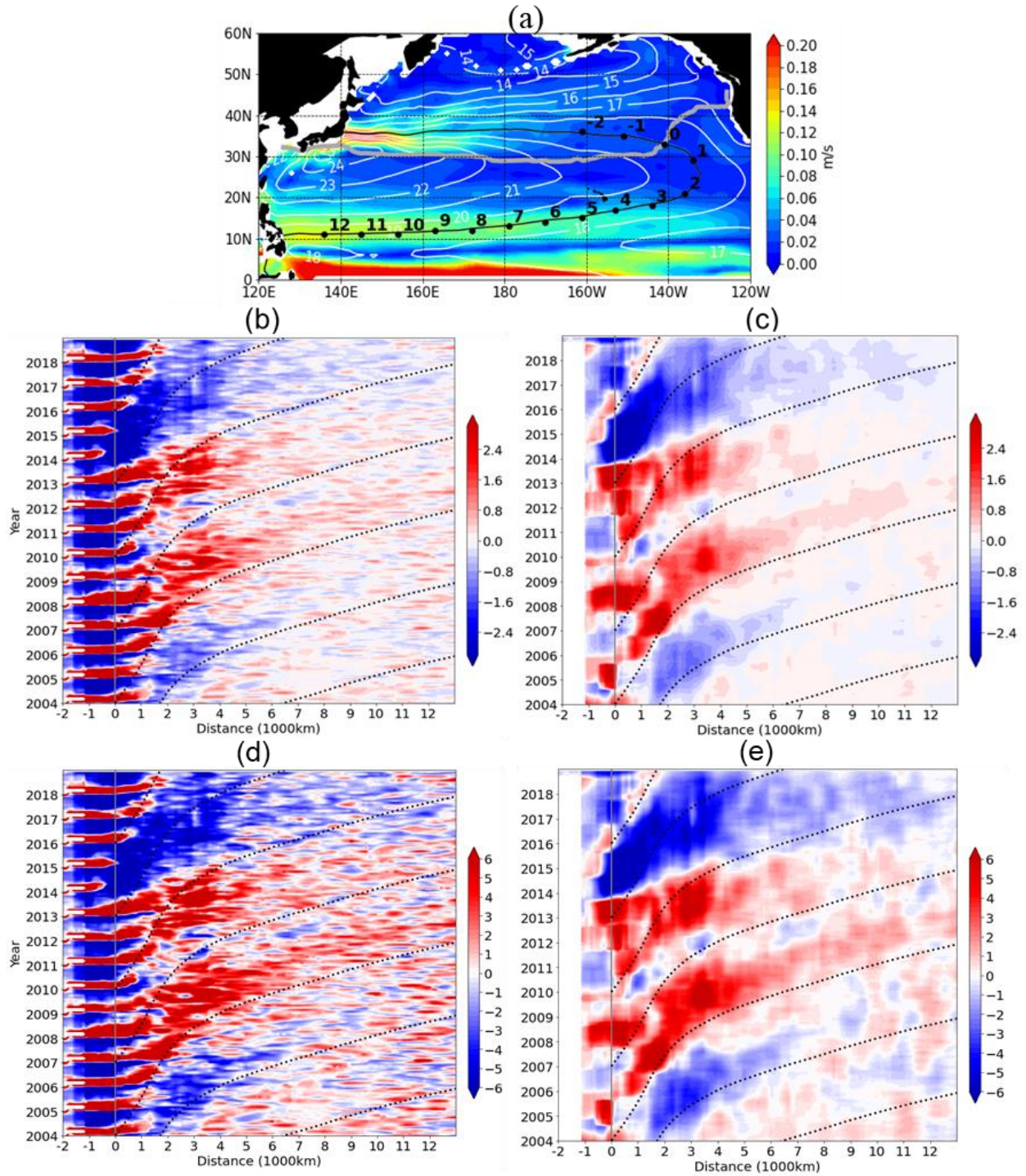


Figure 4.11 (a) (b) Same as **Figure 3.10** but for thickness anomalies. (c) Same as (b) but with thickness low-pass filtered by 12-month running average. (d) (e) Same as (b) (c) but for potential thickness anomalies.

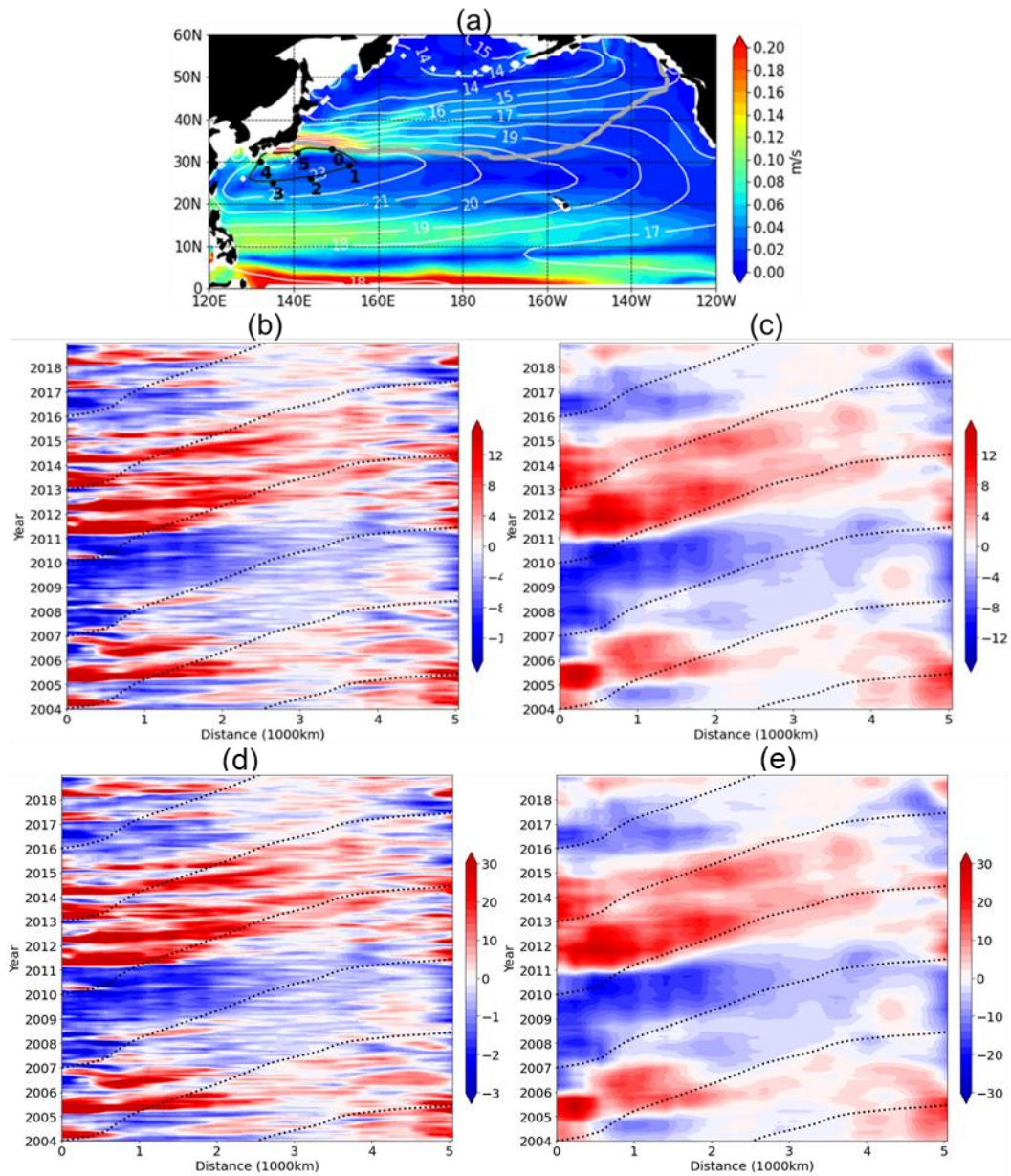


Figure 4.12 (a) (b) Same as **Figure 3.11** but for thickness anomalies. (c) Same as (b) but with thickness low-pass filtered by 12-month running average. (d) (e) Same as (b) (c) but for potential thickness anomalies.

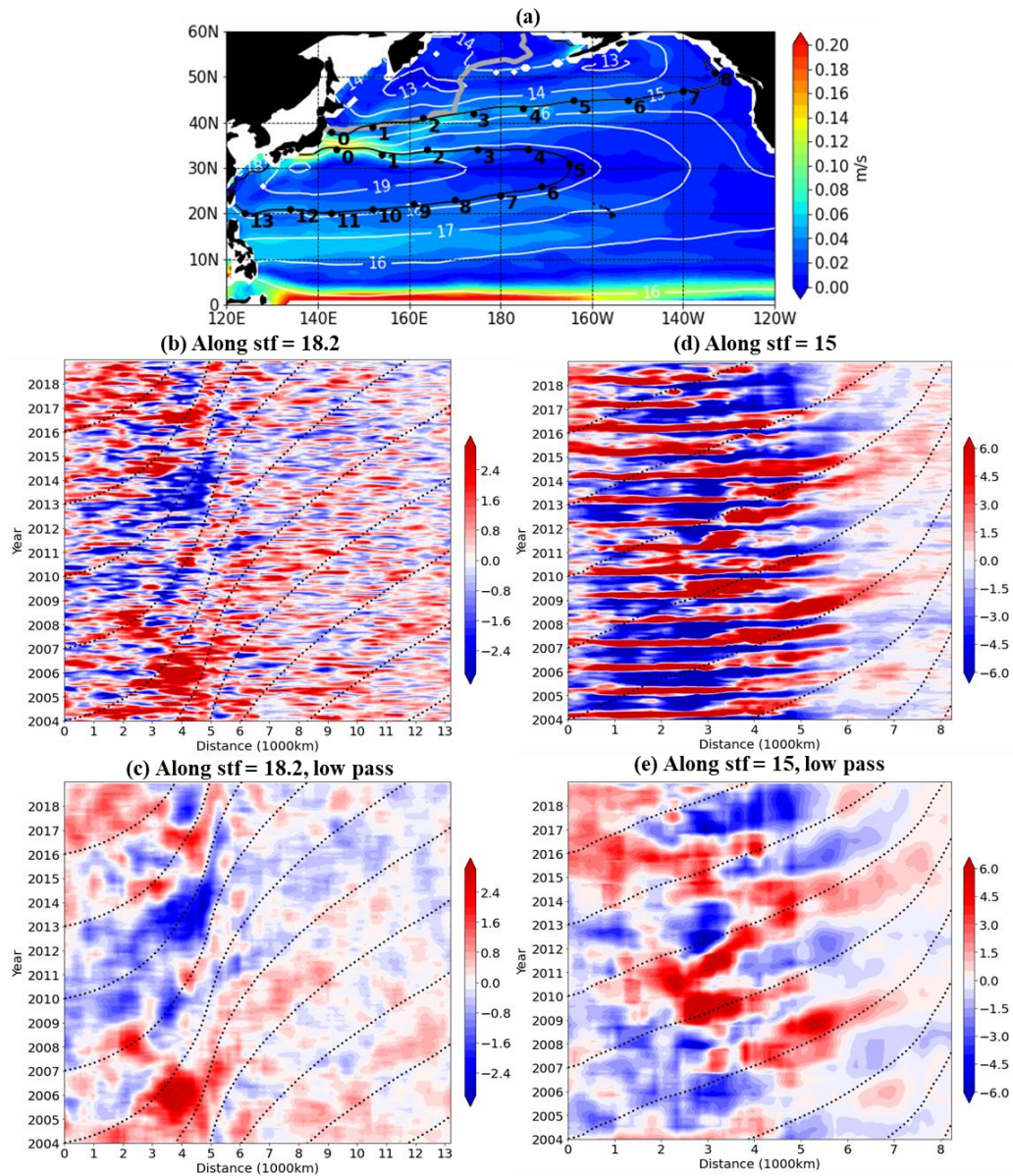


Figure 4.13 (a) (b) (d) Same as **Figure 3.12** but for thickness anomalies. (c) (e) Same as (b) (d) but with thickness low-pass filtered by 12-month running average.

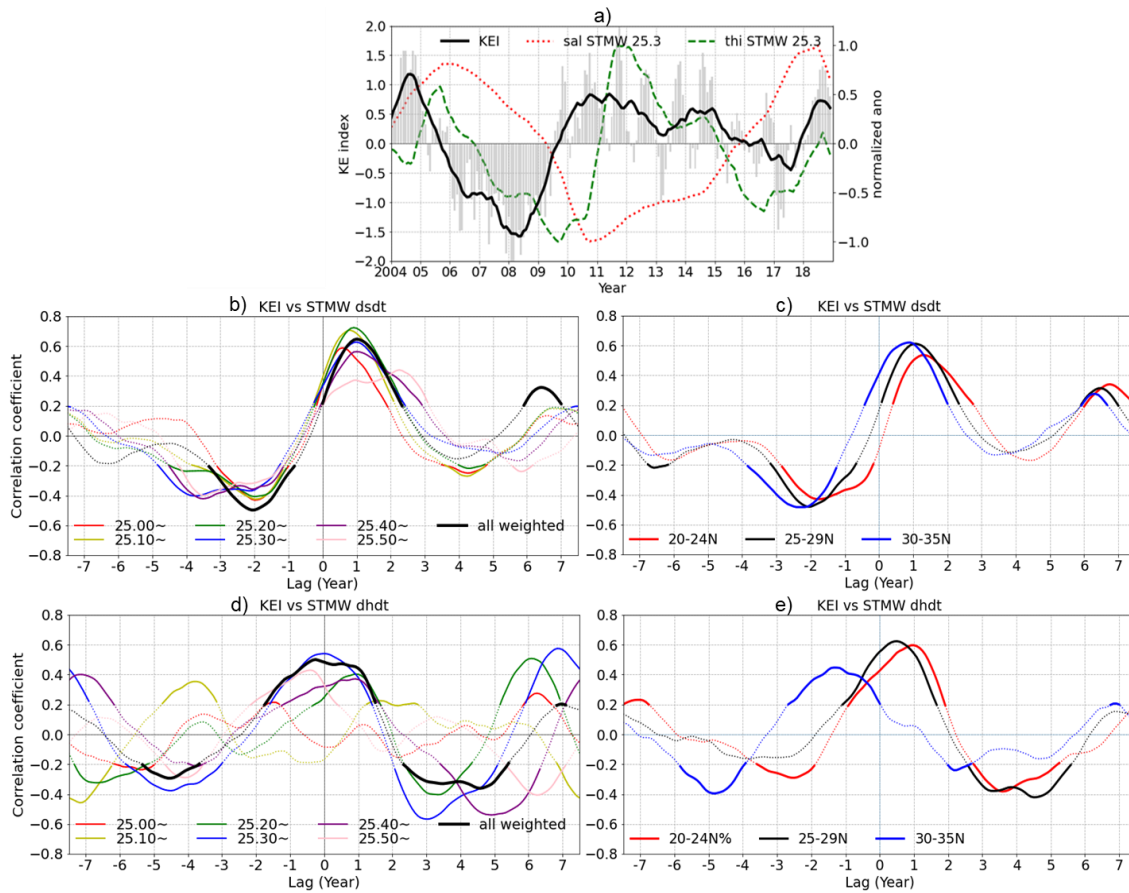


Figure 4.14 (a) Time series of monthly KEI (gray bars) and low-pass filtered KEI (solid black). Low-pass filtered spiciness anomalies and thickness anomalies in STMW on 25.3 γ is indicated by dashed red and green lines. KEI is from Qiu et al. (2021), based on AVISO-observed 4 dynamic properties. Positive (negative) KEI indicates a stable (unstable) KE state. (b) Lag-correlation coefficient between KEI and salinity change rate in STMW, averaged on surfaces $\gamma = 25.00-25.05$ (red), 25.10-25.15 (yellow), 25.20-25.25 (green), 25.30-25.35 (blue), 25.40-25.45 (purple), 25.50-25.60 (pink), and thickness-weighted on 25.00-25.60. Positive lags indicate KEI leads to salinity variation. The values significant at 99% are solid and thickened. All the series are detrended and low-pass filtered by the 12-month moving average before calculation. (c) Same but averaged in 20-24 $^{\circ}$ N (red), 25-29 $^{\circ}$ N (black), and 30-35 $^{\circ}$ N (blue), respectively. (d)(e) Same as (b)(c) respectively, but for thickness.

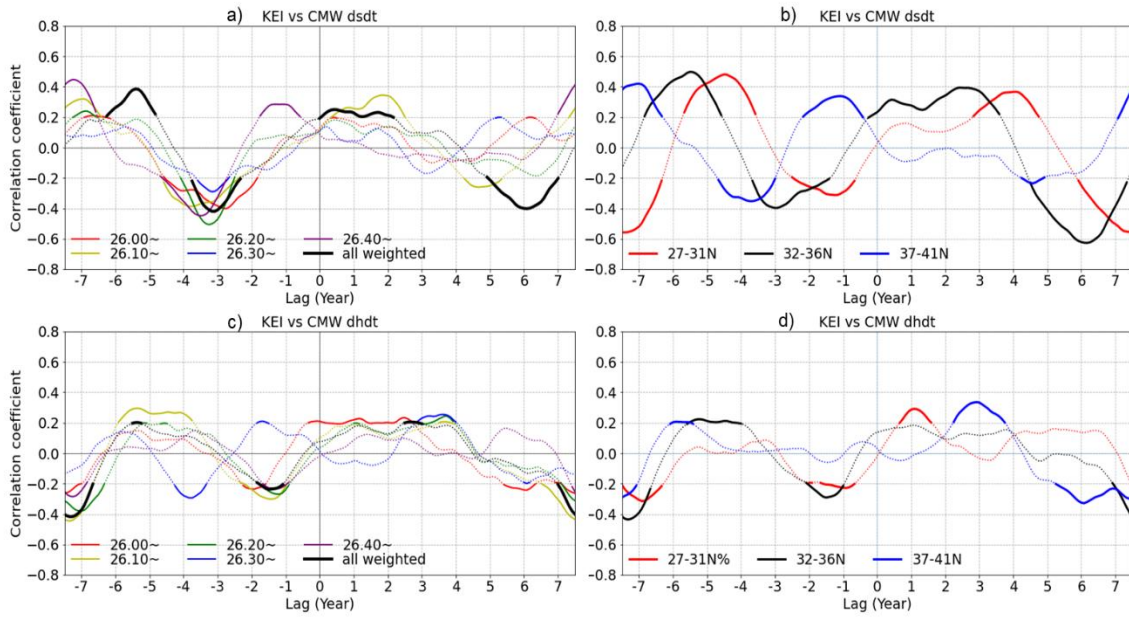


Figure 4.15 Same as **Figure 4.14** (b)-(e) but for CMW, averaged on surfaces $\gamma = 26.00$ - 26.05 (red), 26.10 - 26.15 (yellow), 26.20 - 26.25 (green), 26.30 - 25.35 (blue), and 26.40 - 26.45 (purple), and thickness-weighted on 26.00 - 26.45 .

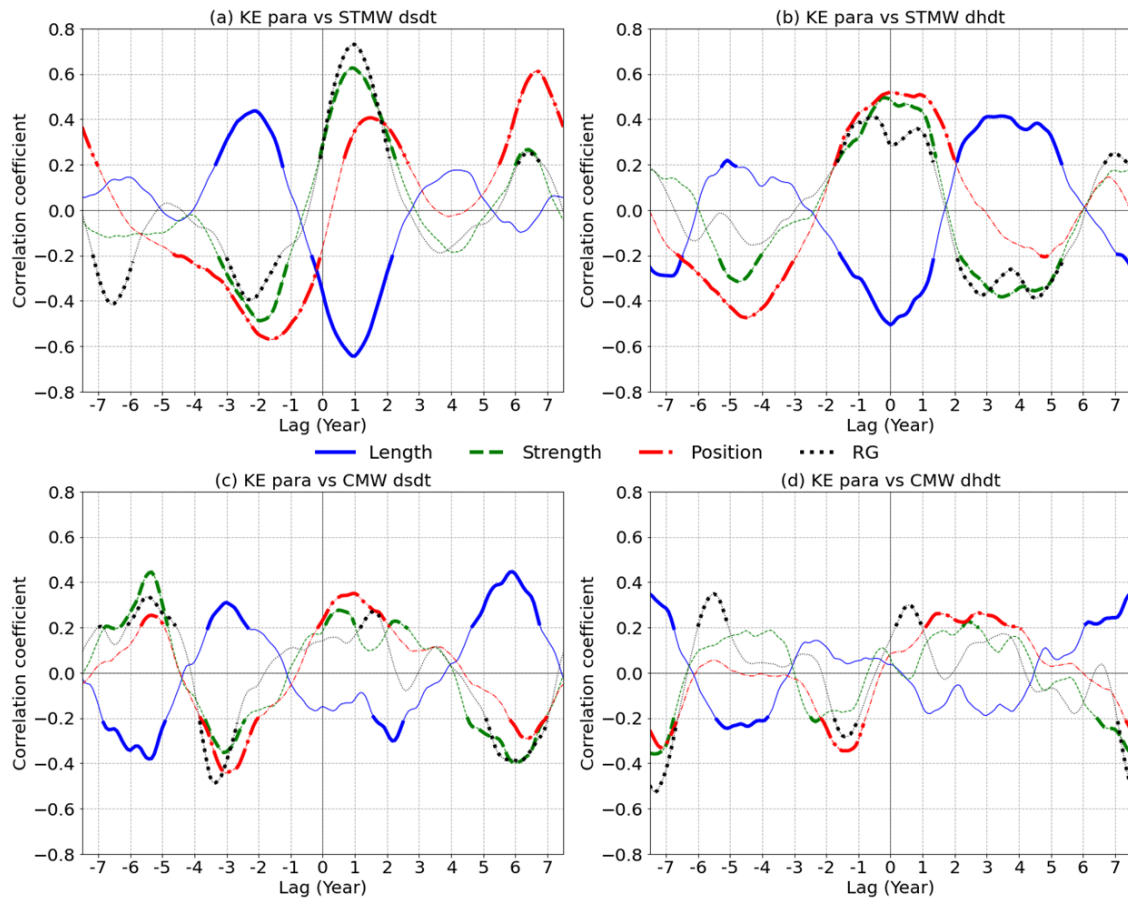


Figure 4.16 Lag-correlation coefficient between four KE parameters and (a) STMW salinity tendency, (b) STMW thickness tendency, (c) CMW salinity tendency, and (d) CMW thickness tendency. The methods of the calculations are the same as in **Figure 4.14**. The four parameters, upstream KE path length (141°-153°E), KE strength (141-165°E), upstream KE position (141-165°E), and KE recirculation gyre strength, were indicated in straight blue, dashed green, dash-dot red, and dotted black, respectively.

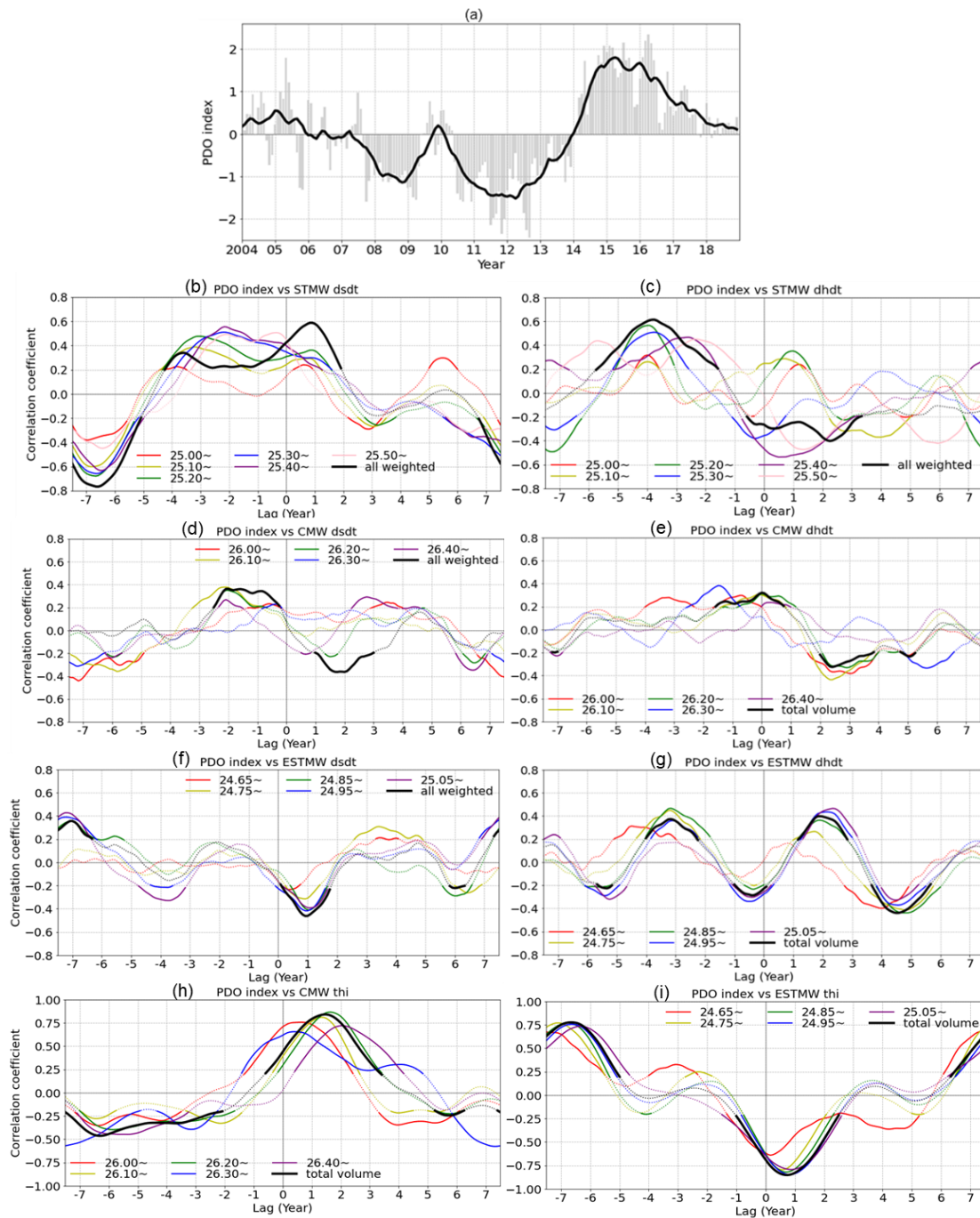


Figure 4.17 (a) PDO index available from https://ds.data.jma.go.jp/tcc/tcc/products/elnino/decadal/pdo_month.html. (b)(c)(d) Lag correlation coefficient between PDO index and the salinity change rate of STMW, CMW, and ESTMW respectively. All time series were detrended and low-pass filtered before the calculation. (e)(f)(g) Same as (b)(c)(d) but for the thickness change rate. (h)(i) Same as (e)(g) respectively but for thickness.

5 Propagation processes of water mass anomalies

5.1 Estimation of propagation processes along streamlines by salinity conservation equations

In section 3.5, the propagation direction and speed of spiciness anomalies were investigated along the geostrophic currents. It is then natural to ask about the contributions of different processes to the propagation of the spiciness anomalies. In this section, we estimated the effects of different processes quantitatively.

5.1.1 Methodology

Adopted from Kilpatrick et al. (2011), the conservation equation of salinity on the isopycnal surface can be written as:

$$\frac{\partial S}{\partial t} + \vec{u}_h \cdot \nabla_h S + \frac{D\sigma_\theta}{Dt} \frac{\partial S}{\partial \sigma_\theta} = 0, \quad (5.1)$$

where S is salinity, \vec{u} is geostrophic velocity, ∇_h is taken along constant isopycnals, $\frac{D\sigma_\theta}{Dt}$ is related to the transformation from z to σ_θ (Vallis, 2006), and subgrid-scale diffusion and mixing were neglected.

In the interior ocean, diapycnal mixing rates were negligible (Ledwell et al. 1993), so $\frac{D\sigma_\theta}{Dt}$ can be neglected,

$$\frac{\partial S}{\partial t} + \vec{u} \cdot \nabla S = 0, \quad (5.2)$$

And to focus on the effects of processes on the interannual variations, the S and \vec{u} fields are decomposed to climatology and anomalies:

$$S = \bar{S} + S', \quad \vec{u} = \vec{\bar{u}} + \vec{u}'. \quad (5.3)$$

So (5.2) can be converted into:

$$\frac{\partial S'}{\partial t} = -\vec{\bar{u}} \cdot \nabla S' - \vec{u}' \cdot \nabla \bar{S} - (\vec{u}' \cdot \nabla S' - \overline{\vec{u}' \cdot \nabla S'}) \quad (5.4)$$

The term in the LHS indicates the temporal change rate of salinity anomalies. The first term in the RHS is the mean advection term, which means the advection of the anomalous salinity gradient by the mean current; the second term is the anomalous advection term, describing the advection of the mean salinity gradient by the anomalous current; the last term is the eddy term, describing the influence of the covarying u and S fields.

In $1^\circ \times 1^\circ$ Argo data, (5.4) can be expressed in:

$$\frac{\partial S'}{\partial t} = -(\bar{u} \frac{\partial S'}{\partial x} + \bar{v} \frac{\partial S'}{\partial y}) - (u' \frac{\partial \bar{S}}{\partial x} + v' \frac{\partial \bar{S}}{\partial y}) - [(u' \frac{\partial S'}{\partial x} + v' \frac{\partial S'}{\partial y}) - \overline{(u' \frac{\partial S'}{\partial x} + v' \frac{\partial S'}{\partial y})}]. \quad (5.5)$$

The backward trajectory along a streamline was conducted in the following steps:

1. Take a starting time and estimate the arriving time at each grid from the mean geostrophic speed averaged between an upstream grid and a downstream grid.
2. Calculate the instant value of the terms at the arriving time obtained in 1 at each grid. The $\frac{\partial}{\partial t}$, $\frac{\partial}{\partial x}$, $\frac{\partial}{\partial y}$ were calculated from the arriving time and positions between a previous and a latter grid.
3. Calculate the time integration of the terms in 2 from the downstream to the upstream. The time integrations indicate accumulated changes of salinity anomalies caused by the different terms along the path.
4. Apply 1-3 from a starting time to all the other months and get the time-distance diagram of the terms.

The forward trajectory is calculated in the opposite direction, integrated from the upstream position to the downstream.

5.1.2 Forward integration

To investigate the causes of the spiciness anomalies and their propagation, the method was conducted primarily in a forward trajectory from the outcrop line to the downstream, with a starting time at the beginning of the data period.

An example is shown in Figure 5.1. We first compared the values of the term in the RHS and the sum of the terms in LHS in equation (5.5). They were comparable at most of the positions but showed large differences near points 1-4, and the integrated values had a large deviation from this region all the way to the downstream (Figure 5.1 b and c). This region coincides with the subduction and distribution regions of ESTMW at its base, where the potential of active double diffusion was observed (Section 3.6.3). Since equation (5.5) neglected the effects of diffusion, it is not appropriate to be used in this region. Therefore, the same calculation was conducted from a starting point south of the ESTMW distribution region. The instantaneous values in the LHS and RHS showed a good correlation with $R = 0.97$ (Figure 5.2 b). Their integrated values, though they still showed deviations, was comparable (Figure 5.2 c). So, we applied the forward integration in Figure 5.2 to every month, and the time-distance diagram was shown in Figure 5.3.

The salinity anomalies were mostly consistent with the mean advection term. The mean advection term reflected the phase and amplitude of the interannual salinity anomalies well. This is consistent with the previous analysis that suggested the spiciness anomalies move

approximately with geostrophic speed along a Montgomery Stream function contour (Sasaki et al., 2010). The anomalous advection term also showed the phases of the interannual variations but overestimated the amplitudes in the downstream. The eddy term showed a pattern with higher frequency. They made the total effects of the time-dependent terms much noisier than the time-independent terms, causing a large discrepancy.

5.1.3 Backward integration

Because the amplitudes of salinity anomalies were larger upstream than downstream, even a small error of the estimated processes can result in a large discrepancy after the time integration. Therefore, we also conducted the backward trajectory from the downstream to the upstream. In Figure 5.4, the correlation of the instantaneous values between the lhs and rhs of the equation was 0.95, and their time integrations were also correlated except near the outcrop line (points 0-2). Most of the time, the anomalous term and the eddy term canceled each other downstream, so the mean advection term was close to the total effects. However, at point 8, where the advection term was much larger than the real anomaly tendency, both the anomalous advection and the eddy term had a negative effect, making the estimated anomaly tendency closer to the real anomaly tendency than the effect of mean advection alone.

In the time-integrated diagram (Figure 5.5 c), the mean advection term was highly consistent with the real salinity anomalies. Especially in the downstream south of 20°N (points 5-15), the values of both the low-frequency and high-frequency signals show little difference between the salinity anomalies and the mean advection term (Figure 5.5 a, b, and e). However, north of 20°N (points 0-4), anomalous advection term induced strong signals with a time scale of several months to one year, and the eddy term induced positive signals the most time before 2009. Besides, the time-dependent terms also contributed to the propagation of the low-frequency anomalies. The discrepancy between the time-independent and the dependent terms was large in points (1-5). As mentioned in the forward integration, it could be caused by the diffusion at the base of the ESTMW.

A similar investigation was also conducted along the streamlines that go through the western and central longitudes (Figure 5.6 and Figure 5.7). A good correlation between the salinity anomalies and the mean advection term was also shown along the two streamlines. The anomalous advection term, however, showed the patterns of salinity anomalies that have earlier phases than the real ones, especially along the western streamline. Along the western streamline, the eddy term contributed to the low-frequency with large values but also induced high-frequency anomalies with opposite signs and larger amplitudes than low-frequency anomalies. This indicated a more important contribution of eddy terms in the western subtropics than in

the eastern subtropics and that they can both accelerate and disturb the propagation of anomalies. The discrepancy in the equation was strong in points 0-2 and points 0-4 along the western and central pathways, respectively. Both regions are near the outcrop line, around which the isopycnals may undergo diapycnal mixing, and the signals occurred almost simultaneously instead of propagating downstream. Both the two kinds of cases are in contradiction with the requirements of the equation.

5.2 Estimation of eddy effects with bolus velocity

Because the resolution of gridded Argo ($1^\circ \times 1^\circ$) is not high enough to resolve mesoscale eddies, in this section, we used the eddy-resolved ($1/10^\circ \times 1/10^\circ$, daily) reanalysis dataset FORA-WNP30 during 2004-2015. It is literally enough to resolve mesoscale eddies. For consistency with the previous chapters, we interpolated the dataset from pressure coordinates to potential density coordinates.

The transport of a water mass within an isopycnal layer can be calculated as $h\vec{u}$, where h is the thickness of an isopycnal layer, and \vec{u} is velocity.

We can split the terms into time-mean and time-varying components:

$$h = \bar{h} + h'$$

$$u = \bar{u} + u'$$

where the prime denotes the time-varying component.

The total thickness flux is then decomposed as:

$$\overline{hu} = \bar{h}\bar{u} + \overline{h'u'}$$

$\bar{h}\bar{u}$ is the mean transport and $\overline{h'u'}$ is the eddy-induced transport.

The eddy-induced transport divided by the mean layer thickness,

$$v = \frac{\overline{h'u'}}{\bar{h}}$$

is called the bolus velocity (Marshall, 1997).

Previous studies did not provide a uniform standard for the time period to separate the mean and the anomaly term. According to the theoretical work of Lee et al. (1997), the time-mean tracer was averaged over several eddy life cycles. Because the interest in this section is on the mesoscale eddies, which have a life cycle of about 3-4 months, we separated the mean and anomaly terms by running average with periods of 91, 181, and 361 days respectively. The climatology of the bolus velocity is shown in Figure 5.8. Bolus velocity was the largest, with a window of 361 days, which was over 3-4 cycles of the mesoscale eddies. Besides, if we chose a window longer than 361 days to obtain a larger bolus velocity, the time-varying term can also

include the interannual variabilities. Therefore, we only discussed the results with a 361-day window.

On $\sigma = 25.3$ surface, a large bolus velocity was discovered in the KE region (140°E-170°W, 30-40°N). The meridional component of bolus velocity showed opposite directions upstream of the KE (140-160°E). However, it was southward in most positions downstream of the KE (160-175°W) (Figure 5.9), indicating the vital role of eddies in transporting water from the KE region to the formation and distribution region of STMW. South of the KE region, northward bolus velocity was shown only west of 140°W and north of 25°N. The entire distribution region of STMW showed a southward bolus velocity component, and the speed was larger from the northeast to the southeast compared to that in other regions, which coincided with the distribution path of STMW and the propagation path of the salinity and thickness anomalies. This is consistent with the higher propagation speed of the anomalies compared to the geostrophic speed.

The zonal component of bolus velocity was eastward along the KE in 35-40°N but was westward south of KE in 30-35°N west of 160°E with a speed of ~ 0.02 m/s. The westward component was also found in 20-30°N west of 145°E, in a region containing the northwestern part of STMW. In the same region, while the geostrophic current was northeastward, the spiciness and thickness anomalies (Figure 3.11 Figure 4.12) propagated southwestward from the outcrop line. This can be explained by the rapid westward bolus velocity.

5.3 Discussions and conclusions

In Chapter 5, we quantitatively examined the effects of different processes during the propagation of the anomalies. The salinity conservation equation on isopycnals, which was used in ocean models in previous studies (Kilpatrick et al., 2011; Furue et al., 2015; Taguchi et al., 2017), was applied to and time-integrated in an observational dataset for the first time.

The propagation of spiciness anomalies is mainly attributed to the contributions of mean advection. This is for the streamline in western, central, and eastern subtropics. Anomalous advection has fewer overall contributions but was important in generating local signals. Eddy effects can both accelerate and disturb the propagation of spiciness anomalies and are important in the western subtropics. The reconstructed time-distance diagram of the salinity anomalies and the mean advection using gridded Argo data without numerical models showed a substantial agreement with the real anomalies, first proved that the observational dataset can also be used to estimate quantitatively the effects of different processes on propagating spiciness anomalies quantitatively. The discrepancies between the time-independent and time-

dependent terms were large near the outcrop line in the western to central longitudes and near the base of the ESTMW distribution region in the eastern longitudes. They are related to the isopycnal and diapycnal mixing/diffusion that cannot be neglected in the same regions.

A high-resolution reanalysis dataset was used to investigate the effects of mesoscale eddies, which cannot be fully resolved in Argo. The eddy-induced bolus velocity showed a southward component in the entire distribution region and the eastern part of the formation region of STMW and a westward component in the northwestern part of STMW. The results verified the effects of eddies on transporting the anomalies from KE to STMW. Though the bolus velocity is calculated from thickness, it indicates eddy transport on isopycnals, which can also transport other tracers such as spiciness anomalies. The eddy-induced bolus velocity explained to some degree the higher speed of propagation of spiciness and thickness anomalies compared to the geostrophic currents in the western subtropics. However, the bolus velocity itself is insufficient to explain the speed difference fully. It may be related that the spatial resolution in FORA can resolve the mesoscale eddies but cannot fully resolve the submesoscale eddies. Besides, the effects of wave dynamics also needed to be considered in further work.

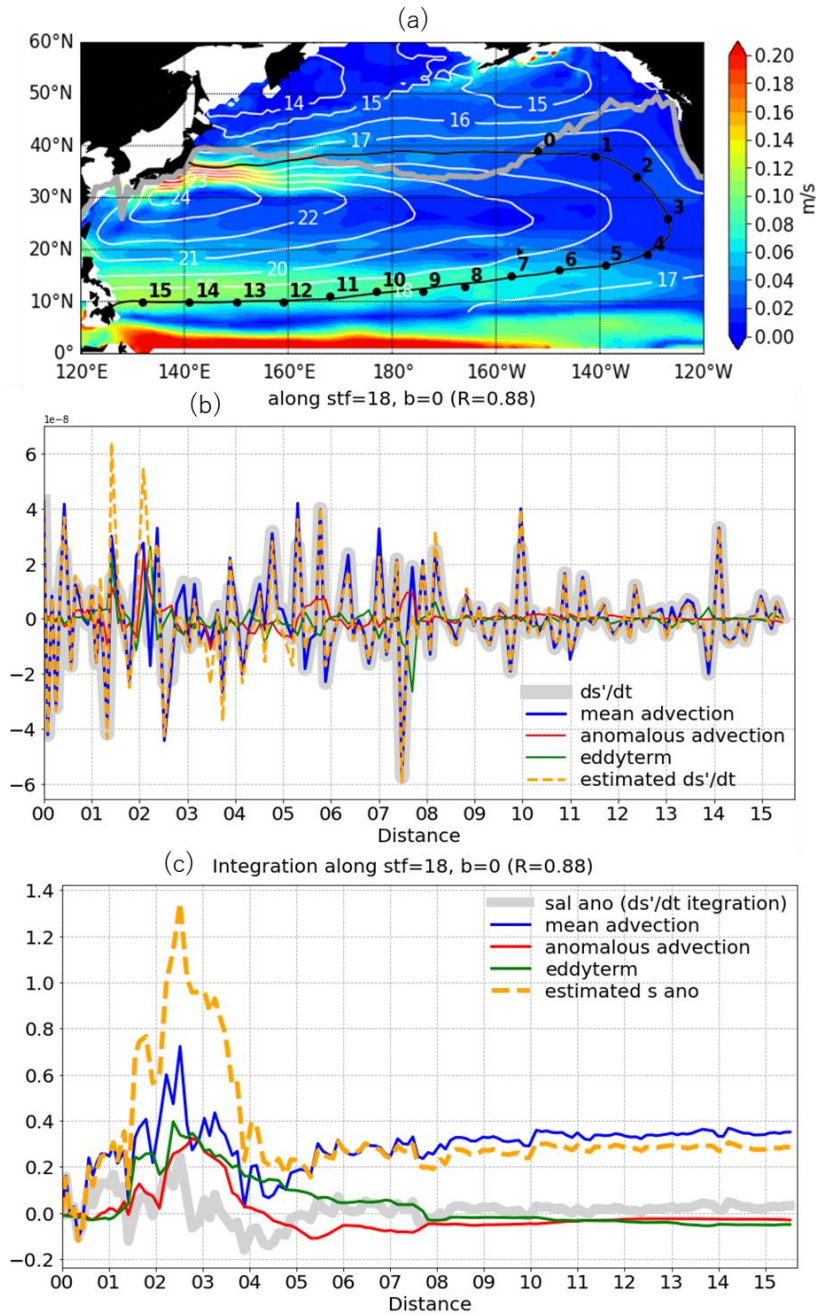


Figure 5.1 (a) Geostrophic velocity (color) and streamline (white contour) on $\gamma = 25.3$ surface (unit: m/s) relative to 1500 dbar. Black contour denotes the 18 isopycnal streamfunction isopleth. (b) The instantaneous values of each term in equation (5.5) calculated along the streamline with a forward trajectory started from the "0" point at Jan 2004. (c) Integrated values of (b). Estimated ds'/dt term is calculated from the sum up of the mean advection, anomalous advection, and eddy terms.

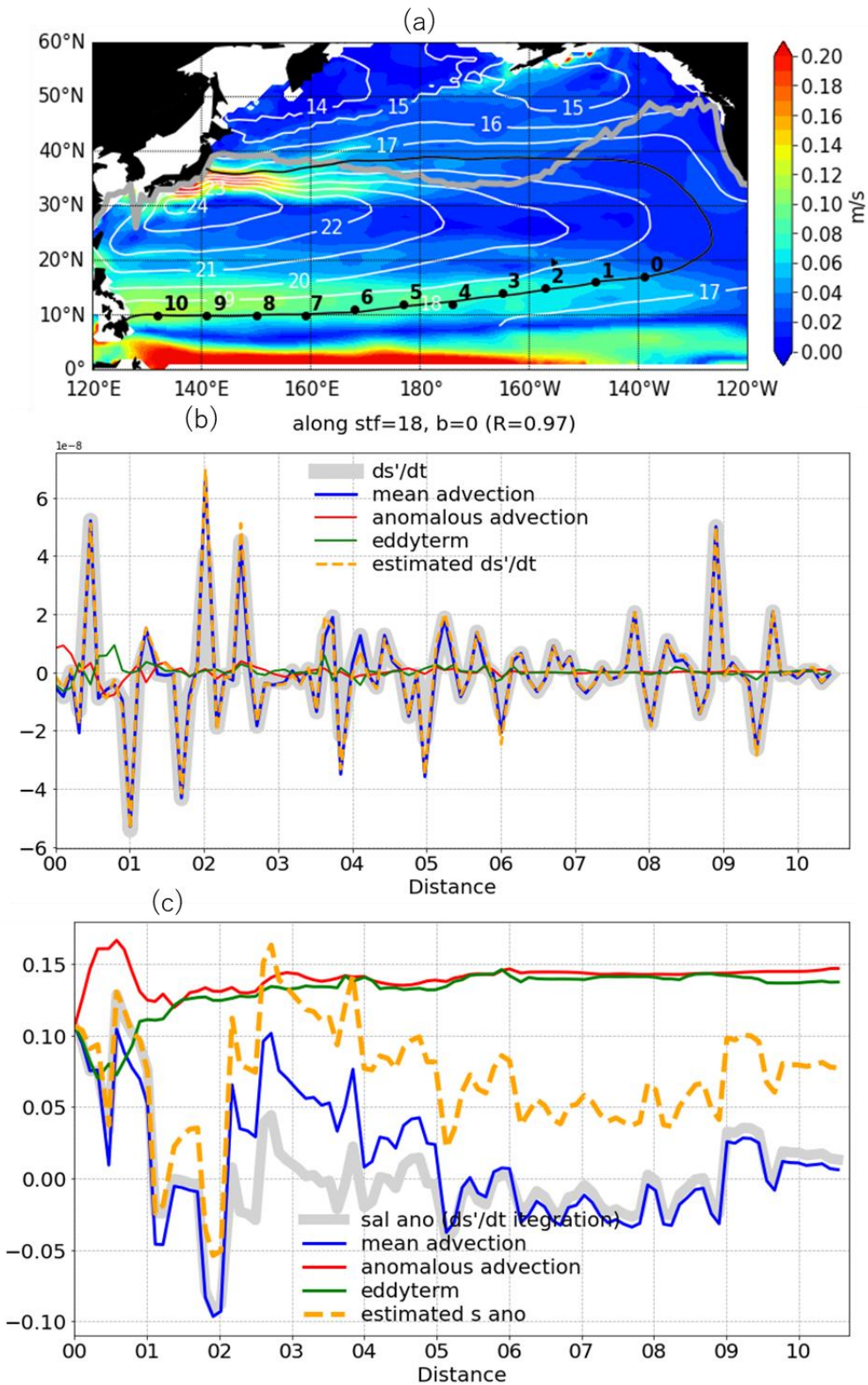


Figure 5.2 Same as **Figure 5.1** but with a “0” point that has a 5000 km distance from the outcrop line.

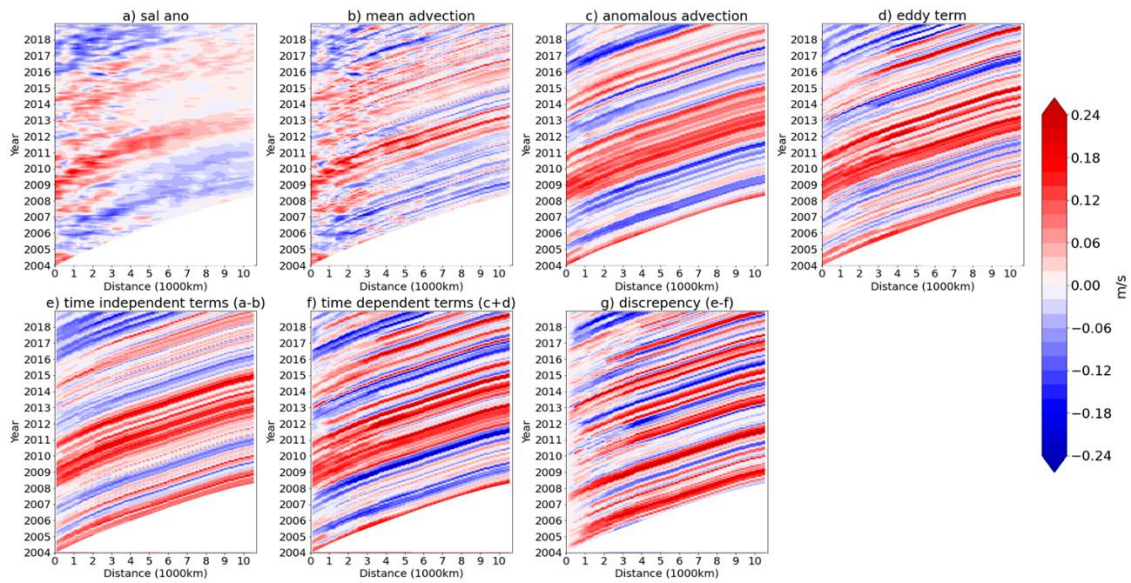


Figure 5.3 Time-distance diagram of the forward time integration along the path in Figure 5.2
a. (a) Integrated time change rate of salinity anomalies, i.e., salinity anomalies. (b) (c) (d) Integrated effects of mean advection, anomalous advection, and eddy term, respectively. (e) Total effects of time-independent terms, calculated from (a)-(b). (f) Total effects of time-dependent terms, calculated from (c)+(d). (g) Discrepancy of the equation, calculated from (e)-(f).

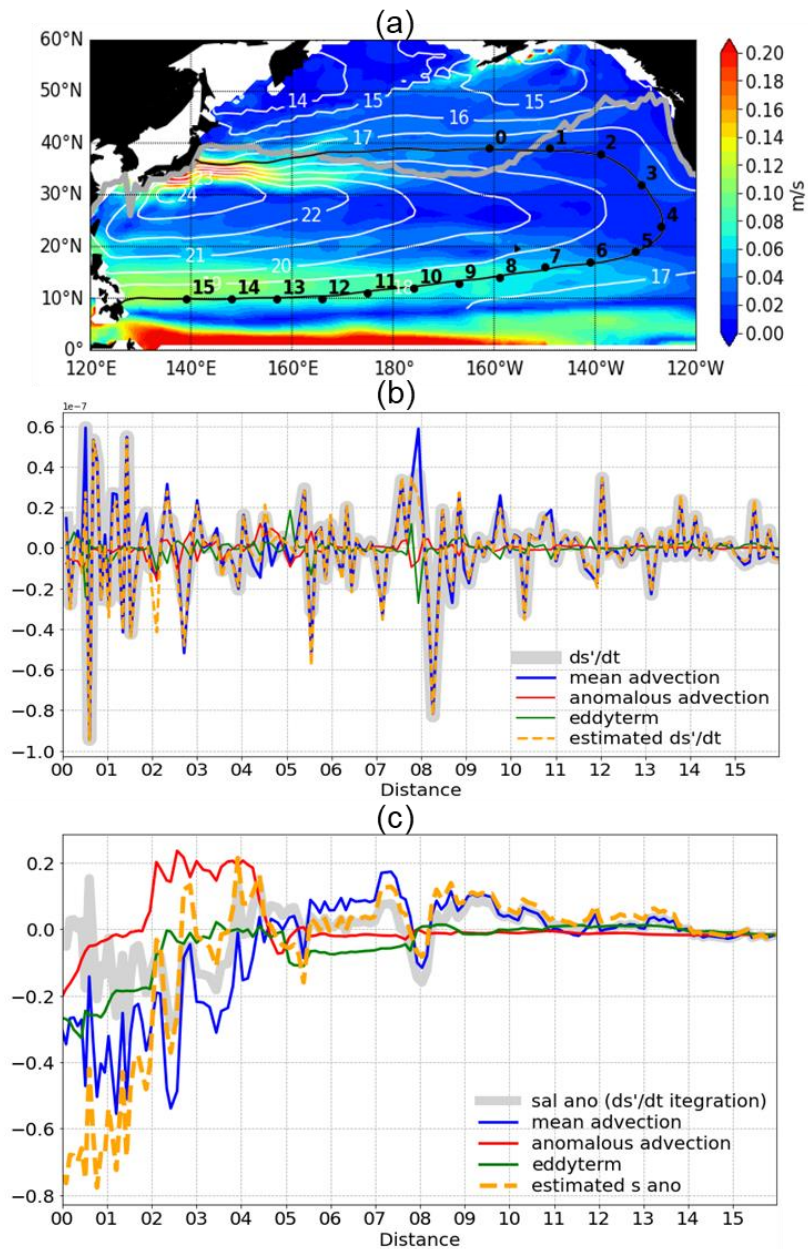


Figure 5.4 Same as Figure 5.1 but is traced backward from the downstream point near the western boundary in the tropics to “0” point north of the outcrop line, starting from the end of the data period, Dec 2018.

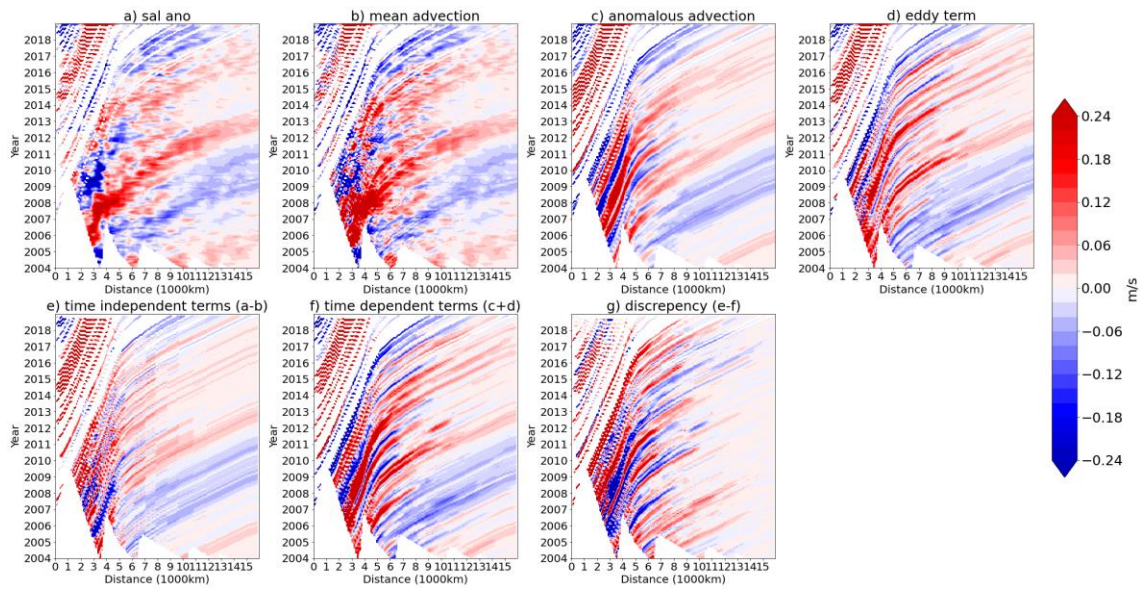


Figure 5.5 Same as Figure 5.3 but is backward integrated along the path in Figure 5.4.

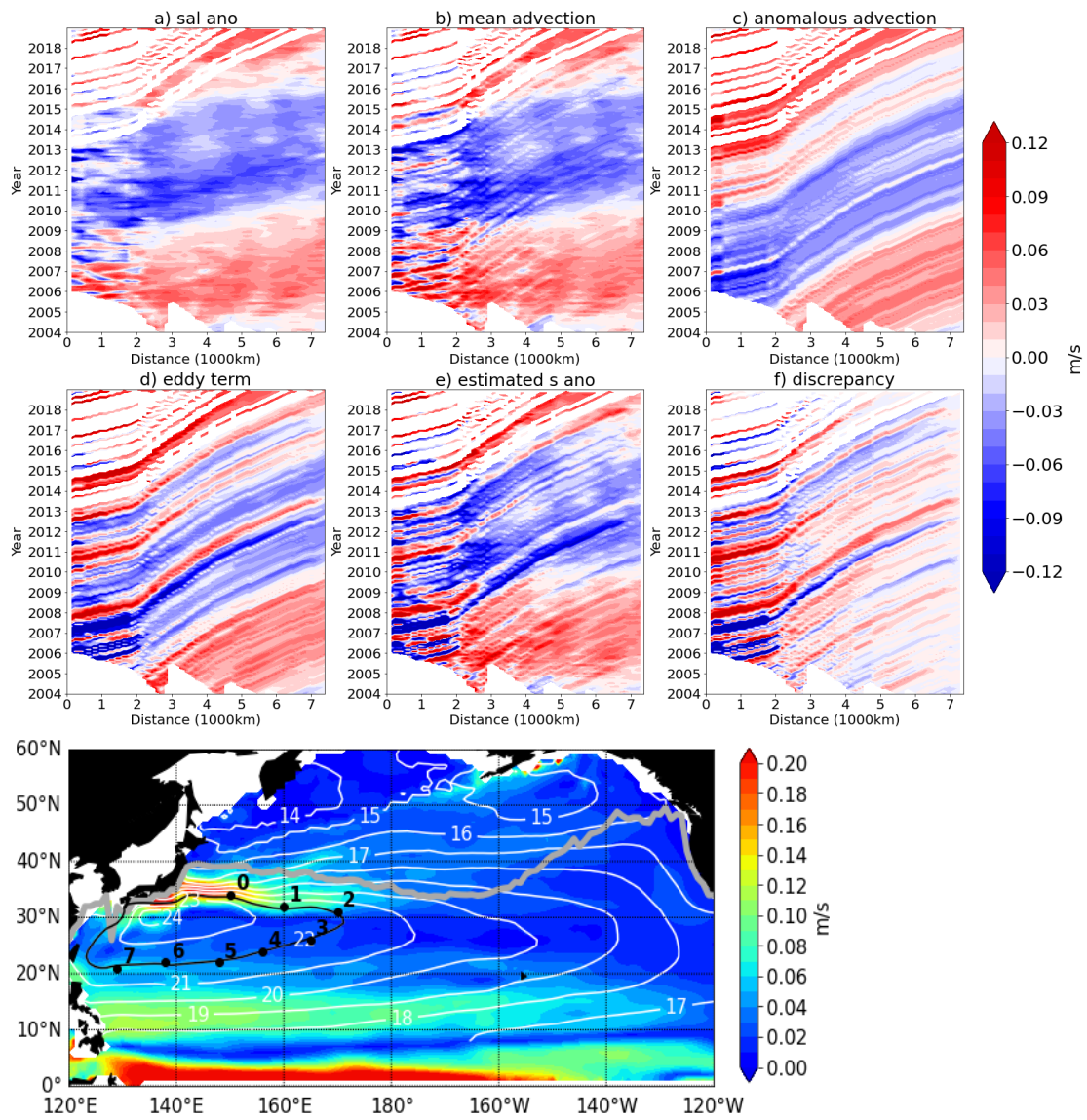


Figure 5.6 Same as Figure 5.5 but along 22 streamfunction isopleth.

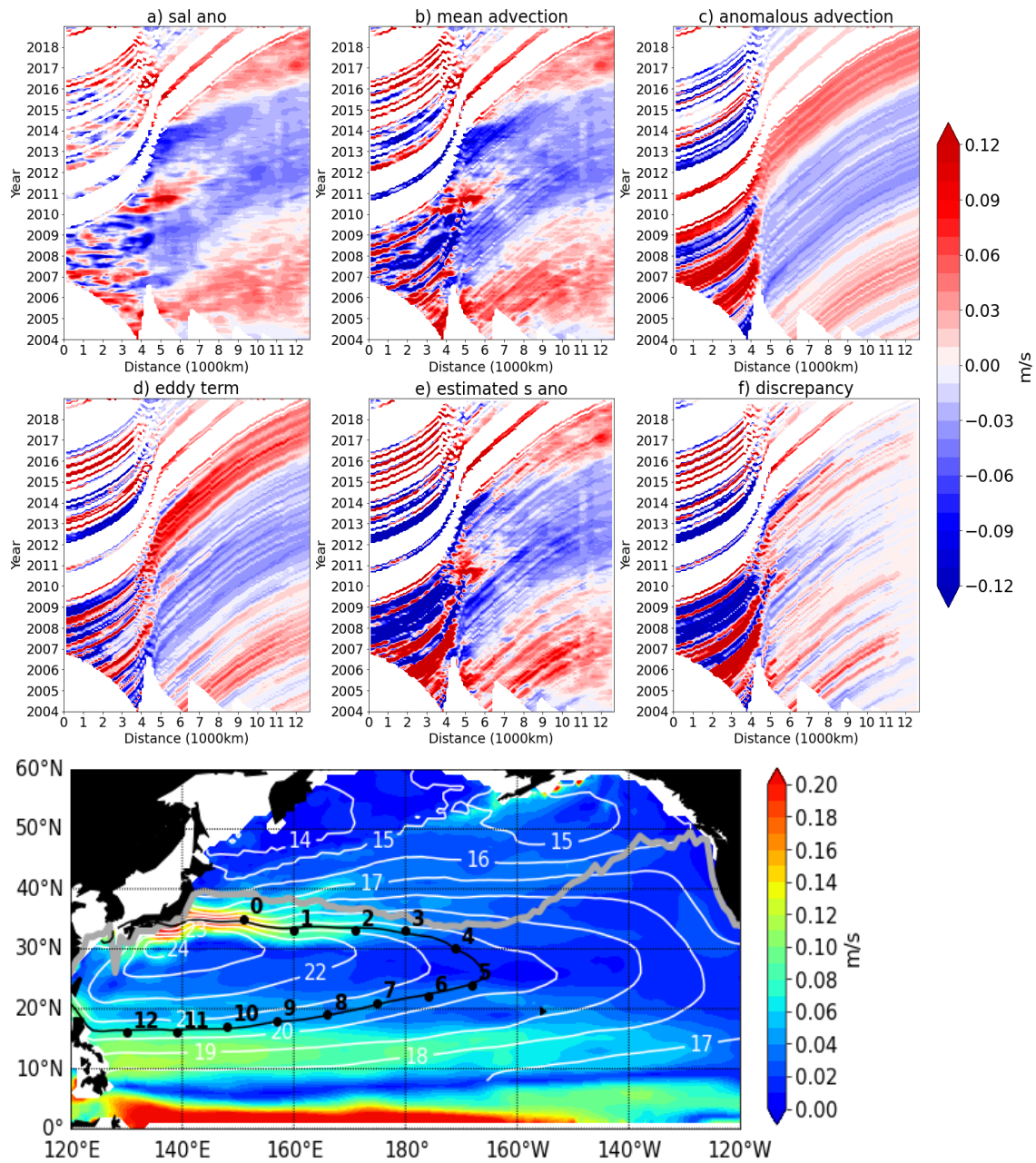


Figure 5.7 Same as Figure 5.5 but along 20.5 streamfunction isopleth.

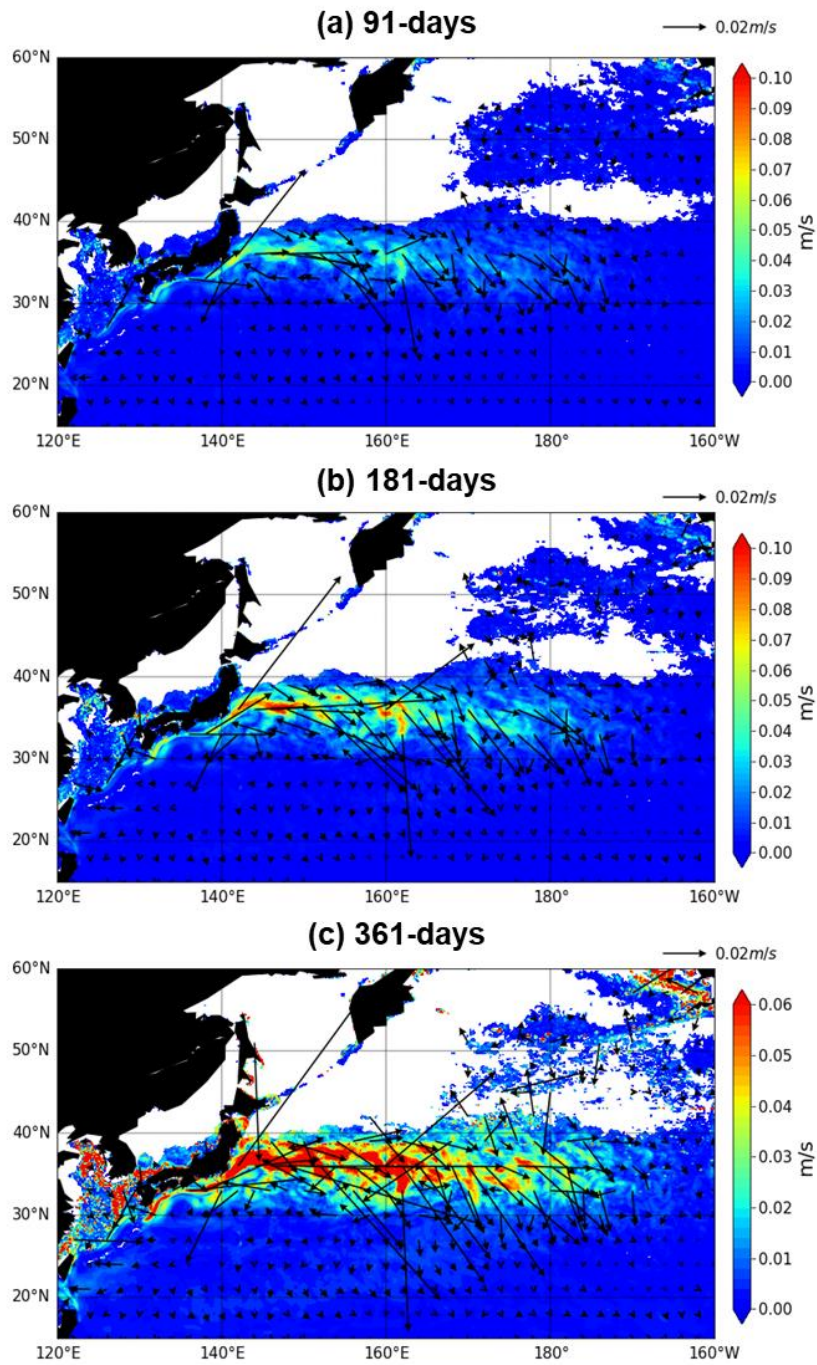


Figure 5.8 Bolus velocity (color) on $\gamma = 25.3$ surface calculated with a low-pass window of (a) 91 days, (b) 181 days, and (c) 361 days. The arrows indicate the direction.

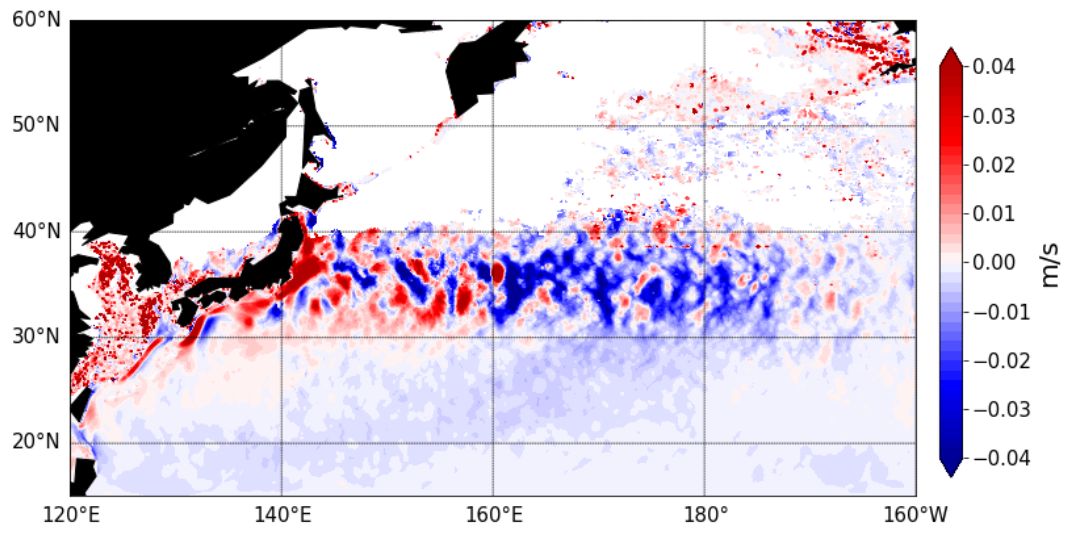


Figure 5.9 Meridional component of climatological bolus velocity on $\gamma = 25.3$.

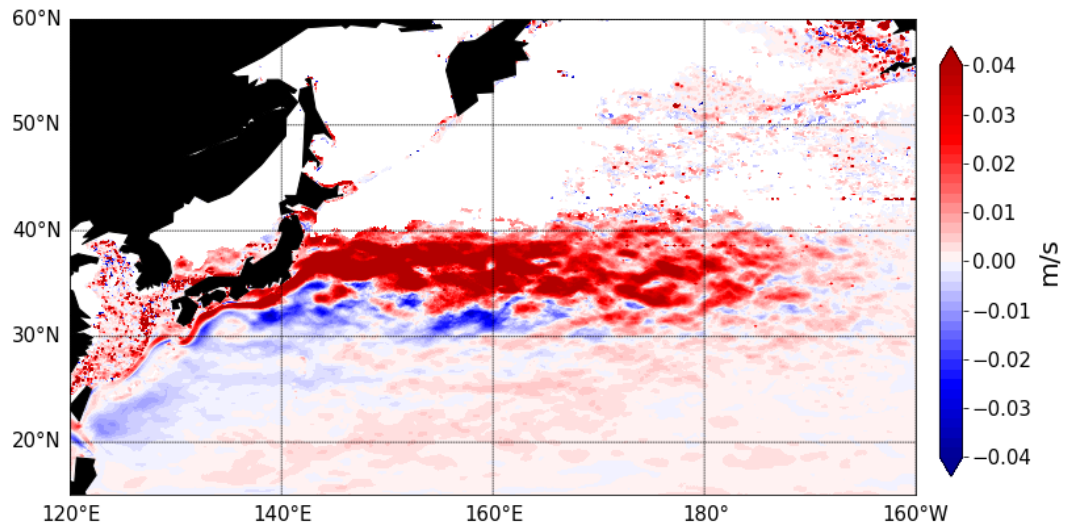


Figure 5.10 Same as Figure 5.9 but for the zonal component.

6 General conclusions

This study comprehensively described the evolutions of spiciness and thickness anomalies in the upper North Pacific during 2004-2018. The temporal variations, spatial patterns, propagation pathways, and velocities were described by linking to the changes and the processes of the three mode waters (i.e., STMW, CMW, and ESTMW). The possible causes of spiciness and thickness anomalies were discussed. The propagation processes of the anomalies were investigated quantitatively.

In Chapters 3 and 4, the main variabilities are as follows:

The subtropical gyre underwent a freshening trend in the main thermocline.

In the STMW, both its salinity and volume were dominated by quasi-decadal variability. Compared to salinity, total volume had an earlier phase of the decadal cycle. The variations of its lighter and denser parts were uniformed with a lag from light to dense layers in salinity but showed opposite signs in some years in thickness anomalies.

The interannual and longer variability in the CMW during the Argo period were described for the first time. Both the salinity and volume of the CMW showed a significant decreasing trend with a quasi-decadal variability that was out of the phase of the STMW, the phase in volume was later than salinity. There were robust year-to-year variations that were confined to the northern part of CMW, but the variations of volume between different latitudes were consistent with each other. The former is related to the double-diffusive spice injection related to the modification of TRMW into D-CMW, which was proved by large Tu in the region. Besides, distinct variations of salinity were shown between L-CMW and D-CMW.

In the ESTMW, salinity anomalies were dominated by a time scale of 3-4 years, while the volume showed a quasi-decadal variability and a rapid shrinking in 2010-2011. The different time scales indicated the mechanisms that generate spiciness and thickness anomalies.

The above results expanded the description of two dimensions in previous studies to three dimensions and discovered updated variations with different time-scale and amplitudes compared to previous periods.

The spiciness anomalies were generated mostly around the formation regions of the mode waters (i.e., the outcrop region of the isopycnals). The subducted spiciness anomalies showed a good correlation with the meridional migration of the outcrop line and the associated mixed layer salinity anomalies in the western to central North Pacific. This correlation, combined with the spatial patterns, supported the southward pathway from the KE region to the STMW directly and is opposed to the westward pathway from the outcrop region in the eastern basin, which had been raised by modelling studies. However, the above correlation in the eastern subtropics

is only applicable near the outcrop line, and the anomalies in ESTMW were influenced by spice injection at its base. The MLD did not show a correlation with spiciness anomalies.

The influences of winter outcrop on the thickness anomalies were also revealed, but with a different mechanism. Both a thick mixed layer and a wide outcrop range were favorable for a thicker STMW in the following year, and their effects can cancel each other, indicating the role of late winter buoyancy loss in generating thickness anomalies. This correlation was weak in both CMW and ESTMW. The latitudinal position, however, did not show a good correlation with thickness anomalies.

After generated, the seasonal and year-to-year variations of spiciness anomalies were dampened largely within the upstream part. Meanwhile, the low-frequency variations were preserved downstream. They propagated and decayed in the direction of geostrophic currents. The propagation speed of the spiciness anomalies was consistent with the geostrophic currents in the eastern subtropics and the gyre boundary. However, it was significantly faster than the geostrophic currents in the western subtropics. The latter is accompanied by a propagation pathway to the inner side of the streamlines.

The above differences between the western and eastern subtropics were also shown in the propagation of thickness anomalies. However, the propagation of thickness anomalies showed many differences from that of spiciness anomalies. Thickness anomalies with low-frequency were preserved well only in the upstream portion, and they decayed much more rapidly after, related to the mean thickness/Q gradient. The propagation velocity of thickness anomalies had a larger zonal component and a smaller meridional component in both the western and eastern subtropics and a slower speed in the western subtropics. The above differences suggested the contributions of Rossby waves on the propagating of thickness anomalies, which is suggested by previous studies.

While previous studies mainly focused on one water mass at a time or the basin-scale averaged patterns, this study compared similarities and differences between different water masses. Through this way, we discovered phenomena that imply large-scale teleconnection variabilities. For example, both STMW and CMW showed a quasi-decadal variability but with different phases. The lower part of ESTMW and the lighter part of STMW, which have similar density ranges, showed synchronized thickness anomalies despite their distant positions. On $\gamma = 26.30$ in the central longitudes, thickness anomalies of different time scales were generated west and east of the dateline. Those generated west of the dateline had a 6-year time scale and showed poor propagation to the west, and those generated east of the dateline had a 4-year time

scale and propagated eastward mainly by the geostrophic currents. They may influence the waters in the west and east corners at the same time.

The above phenomena were then discussed through lag correlations with KE and PDO. The tendency of both salinity and thickness of STMW showed a good correlation with KEI, but the time lag for that of salinity and of thickness was zero and 1 year, indicating that KE influenced STMW through both dynamical mechanisms and through heat/freshwater flux. CMW and ESTMW showed opposite correlations with PDO in volume, which is positive (negative) for CMW (ESTMW). The STMW and the ESTMW showed opposite correlations with PDO in salinity tendency. The light part of STMW and the dense part of ESTMW showed similar correlation with PDO at 1–2-year lag in thickness tendencies. In addition, CMW and PDO had an earlier phase than KEI. The above correlations and lags supported the hypothesis that PDO-related climate changes was related to the vertical stratification and horizontal spiciness patterns in the central longitudes and CMW directly, and anomalies generated there can be propagated both westward and eastward through different processes and influence the dynamical and thermohaline conditions there. However, the mechanisms of the above hypothesis were not investigated in detail, and future studies were expected to examine it.

In Chapter 5, we estimated the contributions of different processes involved in the propagation of the signals. Based on a salinity conservation equation on isopycnals this study reconstructed the propagation of anomalies with observational data for the first time, and the time-integrated effects were shown. The mean advection term, which indicates the advection of the anomalous salinity gradient by the mean current, took the dominant role in propagating spiciness anomalies. The two time-dependent terms, the anomalous advection term and the eddy term, which indicate the advection of the anomalous salinity gradient by the mean current and the influence of the covarying salinity and velocity fields, canceled the effects between each other in most of the instantaneous values. The anomalous advection term was generally small, but its cumulated effects can induce anomalies that has different phases with the mean advection term. The eddy term induced anomalies with high frequency which can both accelerate and disturb the propagation of the low-frequency anomalies. It was important in western subtropics.

If the ignored processes during the derivation of the equation had zero effects and the calculation were based on observations that were precise enough, the time-dependent and time-independent terms should be equal to each other. However, they showed obvious discrepancies in the upstream region near the outcrop line and the ESTMW distribution region. The diapycnal/isopycnal mixing and the double diffusion that were neglected in the equation can be

large in these regions. Besides, the missing data near the outcrop line and the time and spatial resolutions of the Argo observations also cause difficulties in estimating the effects precisely. Nevertheless, this study does show the possibility of estimating the propagation processes quantitatively based on observational data, and the results reflected well the dominant role of mean advection in the propagation of spiciness anomalies and provided instructive points on the time-dependent terms.

In the last part of this study, to investigate the effects of mesoscale eddies that cannot be fully resolved in $1^\circ \times 1^\circ$ monthly Argo data, we used a high-resolution reanalysis dataset to calculate the eddy-induced bolus velocity. The eddies caused a southward component in the entire distribution region and the eastern part of the formation region of STMW and a westward component in the northwestern part of STMW. The results were consistent with the propagation speed that was faster than the geostrophic speed and the propagation pathway that was to the inner side of the streamline in the western subtropics. However, the bolus velocity itself is not enough to fully explain the speed difference. Besides, we did not explain the different propagation velocities between spiciness and thickness anomalies which could be caused by wave dynamics according to theoretical and numerical studies; future work was expected to estimate the effects of other processes such as Rossby waves and submesoscale eddies.

The quantification of different propagation processes in Chapter 5 and the discussions on the origins of anomalies in Chapters 3 and 4 are instructive steps to understand how the anomalies are affected by variations at different origins, different occurrence time, along different pathways with different transit time (along streamline and across streamline), and how large is their contribution. Our future goal is to construct the Transit Time Distribution of the anomalies, so that it would be easier to predict water properties at a downstream point from the known changes in the upstream, and in turn derive what happened in an upstream position by the information in a downstream position. This method can be applied to other tracers including radioactive pollution from Fukushima Daiichi Nuclear accident.

References

- Akima, H. (1970). A New Method of Interpolation and Smooth Curve Fitting Based on Local Procedures. *J. ACM* 17, 589–602. doi:10.1145/321607.321609.
- Allen, M. R., and Ingram, W. J. (2002). Constraints on future changes in climate and the hydrologic cycle. *Nat.* 2002 4196903 419, 228–232. doi:10.1038/nature01092.
- Bindoff, N. L., and McDougall, T. J. (1994). Diagnosing climate change and ocean ventilation using hydrographic data. *J. Phys. Oceanogr.* 24, 1137–1152. doi:10.1175/1520-0485(1994)024<1137:DCCA0V>2.0.CO;2.
- Bingham, F. M. (1992). Formation and spreading of subtropical mode water in the North Pacific. *J. Geophys. Res.* 97. doi:10.1029/92jc01001.
- Cannon, G. A. (1966). Tropical waters in the western Pacific Ocean. 13.
- Cerovecki, I., and Giglio, D. (2016). North Pacific subtropical mode water volume decrease in 2006–09 estimated from Argo observations: Influence of surface formation and basin-scale oceanic variability. *J. Clim.* 29, 2177–2199. doi:10.1175/JCLI-D-15-0179.1.
- Chen, J., Qu, T., Sasaki, Y. N., and Schneider, N. (2010). Anti-correlated variability in subduction rate of the western and eastern North Pacific Oceans identified by an eddy-resolving ocean GCM. *Geophys. Res. Lett.* 37. doi:10.1029/2010GL045239.
- Desbruyères, D., McDonagh, E. L., King, B. A., and Thierry, V. (2017). Global and Full-Depth Ocean Temperature Trends during the Early Twenty-First Century from Argo and Repeat Hydrography. *J. Clim.* 30, 1985–1997. doi:10.1175/JCLI-D-16-0396.1.
- Durack, P. J., Wijffels, S. E., and Matear, R. J. (2012). Ocean salinities reveal strong global water cycle intensification during 1950 to 2000. *Science* (80-.). 336, 455–458. doi:10.1126/SCIENCE.1212222/SUPPL_FILE/DURACK.SM.PDF.
- Endoh, T., Jia, Y., and Richards, K. J. (2006). Sensitivity of the ventilation process in the North Pacific to Eddy-induced tracer transport. *J. Phys. Oceanogr.* 36, 1895–1911. doi:10.1175/JPO2941.1.
- Furue, R., Jia, Y., McCreary, J. P., Schneider, N., Richards, K. J., Müller, P., et al. (2015). Impacts of regional mixing on the temperature structure of the equatorial Pacific Ocean. Part 1: Vertically uniform vertical diffusion. *Ocean Model.* 91, 91–111. doi:10.1016/j.ocemod.2014.10.002.
- Furue, R., Takatama, K., Sasaki, H., Schneider, N., Nonaka, M., and Taguchi, B. (2018). Impacts of sea-surface salinity in an eddy-resolving semi-global OGCM. *Ocean Model.* 122, 36–56. doi:10.1016/j.ocemod.2017.11.004.
- Gu, D., and Philander, S. G. H. (1997). Interdecadal climate fluctuations that depend on exchanges between the tropics and extratropics. *Science* (80-.). 275, 805–807. doi:10.1126/science.275.5301.805.
- Guo, Y., Lin, X., Wei, M., Liu, C., and Men, G. (2018). Decadal Variability of North Pacific Eastern Subtropical Mode Water. *J. Geophys. Res. Ocean.* 123, 6189–6206. doi:10.1029/2018JC013890.

- Häkkinen, S., Rhines, P. B., and Worthen, D. L. (2016). Warming of the Global Ocean: Spatial Structure and Water-Mass Trends. *J. Clim.* 29, 4949–4963. doi:10.1175/JCLI-D-15-0607.1.
- Hanawa, K. (1987). Interannual variations of the winter-time outcrop area of subtropical mode water in the western north Pacific Ocean. *Atmos. - Ocean* 25, 358–374. doi:10.1080/07055900.1987.9649280.
- Hanawa, K., and D. Talley, L. (2001). “Chapter 5.4 Mode waters,” in *International Geophysics* (Academic Press), 373–386. doi:10.1016/S0074-6142(01)80129-7.
- Hanawa, K., and Sugimoto, S. (2004). ‘Reemergence’ areas of winter sea surface temperature anomalies in the world’s oceans. *Geophys. Res. Lett.* 31, n/a-n/a. doi:10.1029/2004GL019904.
- Hautala, S. L., and Roemmich, D. H. (1998). Subtropical mode water in the Northeast Pacific Basin. *J. Geophys. Res. Ocean.* 103, 13055–13066. doi:10.1029/98jc01015.
- Held, I. M., and Soden, B. J. (2006). Robust Responses of the Hydrological Cycle to Global Warming. *J. Clim.* 19, 5686–5699. doi:10.1175/JCLI3990.1.
- Helm, K. P., Bindoff, N. L., and Church, J. A. (2010). Changes in the global hydrological-cycle inferred from ocean salinity. *Geophys. Res. Lett.* 37, 18701. doi:10.1029/2010GL044222.
- Hosoda, S., Ohira, T., Sato, K., and Suga, T. (2010). Improved description of global mixed-layer depth using Argo profiling floats. *J. Oceanogr.* 66, 773–787. doi:10.1007/s10872-010-0063-3.
- Hosoda, S., Suga, T., Shikama, N., and Mizuno, K. (2009). Global surface layer salinity change detected by Argo and its implication for hydrological cycle intensification. *J. Oceanogr.* 65, 579–586. doi:10.1007/s10872-009-0049-1.
- Hosoda, S., Xie, S.-P. P., Takeuchi, K., and Nonaka, M. (2004). Interdecadal temperature variations in the North Pacific Central Mode Water simulated by an OGCM. *J. Oceanogr.* 60, 865–877. doi:10.1007/s10872-005-5779-0.
- Hu, H., Liu, Q., Yuan, Z., and Liu, W. (2011). Variability of subduction rates of the subtropical North Pacific mode waters. *Chinese J. Oceanol. Limnol.* 29, 0–000. doi:10.1007/s00343-011-0000-0.
- Jayne, S. R., and Marotzke, J. (2001). The dynamics of ocean heat transport variability. *Rev. Geophys.* 39, 385–411. doi:10.1029/2000RG000084.
- Joh, Y., and Di Lorenzo, E. (2019). Interactions between Kuroshio Extension and Central Tropical Pacific lead to preferred decadal-timescale oscillations in Pacific climate. *Sci. Rep.* 9, 1–12. doi:10.1038/s41598-019-49927-y.
- Johnson, G. C. (2006). Generation and initial evolution of a mode water θ -S anomaly. *J. Phys. Oceanogr.* 36, 739–751. doi:10.1175/JPO2895.1.

- Katsura, S. (2018). Properties, formation, and dissipation of the North Pacific Eastern Subtropical Mode Water and its impact on interannual spiciness anomalies. *Prog. Oceanogr.* 162, 395–410. doi:10.1016/j.pocean.2018.02.023.
- Katsura, S., Oka, E., Qiu, B., and Schneider, N. (2013). Formation and subduction of North Pacific tropical water and their interannual variability. *J. Phys. Oceanogr.* 43, 2400–2415. doi:10.1175/JPO-D-13-031.1.
- Kilpatrick, T., Schneider, N., and Di Lorenzo, E. (2011). Generation of Low-Frequency Spiciness Variability in the Thermocline. *J. Phys. Oceanogr.* 41, 365–377. doi:10.1175/2010JPO4443.1.
- Kobashi, F., Nakano, T., Iwasaka, N., and Ogata, T. (2021). Decadal-scale variability of the North Pacific subtropical mode water and its influence on the pycnocline observed along 137°E. *J. Oceanogr.* 77, 487–503. doi:10.1007/S10872-020-00579-X/FIGURES/16.
- Kolodziejczyk, N., and Gaillard, F. (2012). Observation of spiciness interannual variability in the Pacific pycnocline. *J. Geophys. Res. Ocean.* 117, 1–19. doi:10.1029/2012JC008365.
- Kolodziejczyk, N., Llovel, W., and Portela, E. (2019). Interannual Variability of Upper Ocean Water Masses as Inferred From Argo Array. *J. Geophys. Res. Ocean.* 124, 6067–6085. doi:10.1029/2018JC014866.
- Kolodziejczyk, N., Reverdin, G., Gaillard, F., and Lazar, A. (2014). Low-frequency thermohaline variability in the Subtropical South Atlantic pycnocline during 2002–2013. *Geophys. Res. Lett.* 41, 6468–6475. doi:10.1002/2014GL061160.
- Kouketsu, S., Osafune, S., Kumamoto, Y., and Uchida, H. (2017). Eastward salinity anomaly propagation in the intermediate layer of the North Pacific. *J. Geophys. Res. Ocean.* 122, 1590–1607. doi:10.1002/2016JC012118.
- Kouketsu, S., Tomita, H., Oka, E., Hosoda, S., Kobayashi, T., and Sato, K. (2011). The role of meso-scale eddies in mixed layer deepening and mode water formation in the western north pacific. *New Dev. Mode-Water Res. Clim. Eff.*, 63–77. doi:10.1007/s10872-011-0049-9.
- Kwon, E. Y., Downes, S. M., Sarmiento, J. L., Farneti, R., and Deutsch, C. (2013). Role of the seasonal cycle in the subduction rates of upper-southern ocean waters. *J. Phys. Oceanogr.* 43, 1096–1113. doi:10.1175/JPO-D-12-060.1.
- Ladd, C., and Thompson, L. A. (2000). Formation Mechanisms for North Pacific Central and Eastern Subtropical Mode Waters. *J. Phys. Oceanogr.* 30, 868–887. doi:10.1175/1520-0485(2000)030<0868:FMFNPC>2.0.CO;2.
- Ladd, C., and Thompson, L. A. (2002). Decadal Variability of North Pacific Central Mode Water*. *J. Phys. Oceanogr.* 32, 2870–2881. doi:10.1175/1520-0485(2002)032<2870:DVONPC>2.0.CO;2.
- Latif, M., and Barnett, T. P. (1996). Decadal Climate Variability over the North Pacific and North America: Dynamics and Predictability. *J. Clim.* 9, 2407–2423. doi:10.1175/1520-0442(1996)009<2407:DCVOTN>2.0.CO;2.

- Li, G., Zhang, Y., Xiao, J., Song, X., Abraham, J., Cheng, L., et al. (2019). Examining the salinity change in the upper Pacific Ocean during the Argo period. *Clim. Dyn.* 53, 6055–6074. doi:10.1007/s00382-019-04912-z.
- Li, Y., and Wang, F. (2015). Thermocline spiciness variations in the tropical Indian Ocean observed during 2003-2014. *Deep. Res. Part I Oceanogr. Res. Pap.* 97, 52–66. doi:10.1016/j.dsr.2014.12.004.
- Li, Y., Wang, F., and Sun, Y. (2012). Low-frequency spiciness variations in the tropical Pacific Ocean observed during 2003-2012. *Geophys. Res. Lett.* 39, n/a-n/a. doi:10.1029/2012GL053971.
- Lukas, R. (2001). Freshening of the upper thermocline in the North Pacific Subtropical Gyre associated with decadal changes of rainfall. *Geophys. Res. Lett.* 28, 3485–3488. doi:10.1029/2001GL013116.
- Lukas, R., and Santiago-Mandujano, F. (2008). Interannual to interdecadal salinity variations observed near Hawaii: Local and remote forcing by surface freshwater fluxes. *Oceanography* 21, 46–55. doi:10.5670/oceanog.2008.66.
- Luo, Y. (2005). On the connection between South Pacific subtropical spiciness anomalies and decadal equatorial variability in an ocean general circulation model. *J. Geophys. Res.* 110, C10002. doi:10.1029/2004JC002655.
- Mantua, N. J., Hare, S. R., Zhang, Y., Wallace, J. M., and Francis, R. C. (1997). A Pacific Interdecadal Climate Oscillation with Impacts on Salmon Production. *Bull. Am. Meteorol. Soc.* 78, 1069–1079. doi:10.1175/1520-0477(1997)078<1069:APICOW>2.0.CO;2.
- Masuzawa, J. (1969). Subtropical mode water. *Deep. Res. Oceanogr. Abstr.* 16, 463–472. doi:10.1016/0011-7471(69)90034-5.
- McDougall, T.J., Thorpe, S.A., Gibson, C. H. (1988). “Small-scale turbulence and mixing in the ocean,” in *Small-Scale Turbulence and Mixing in the Ocean*, 3–9. Available at: https://books.google.co.jp/books?hl=zh-CN&lr=&id=Y3EMJwv4I7kC&oi=fnd&pg=PP1&ots=VKjsVL_3bW&sig=KQdPRq8gPwKlgiB0wO54OcgGGxo&redir_esc=y#v=onepage&q&f=false [Accessed June 2, 2022].
- McDougall, T. J., and Klocker, A. (2010). An approximate geostrophic streamfunction for use in density surfaces. *Ocean Model.* 32, 105–117. doi:10.1016/j.ocemod.2009.10.006.
- Mei-Man, L., Marshall, D. P., and Williams, R. G. (1997). On the eddy transfer of tracers: Advective or diffusive?
- Miyazawa, Y., Zhang, R., Guo, X., Tamura, H., Ambe, D., Lee, J. S., et al. (2009). Water Mass Variability in the Western North Pacific Detected in a 15-Year Eddy Resolving Ocean Reanalysis. *J. Oceanogr.* 65, 737–756. doi:10.1007/s10872-009-0063-3.
- Montgomery, R. B. (1937). A Suggested Method for Representing Gradient Flow in Isentropic Surfaces. *Bull. Am. Meteorol. Soc.* 18, 210–212. doi:10.1175/1520-0477-18.6-7.210.

- Munk, W. (1962). Internal Waves and Small-Scale. *Intern. Waves*.
- Nakamura, H. (1996). A pycnostad on the bottom of the ventilated portion in the central subtropical North Pacific: Its distribution and formation. *J. Oceanogr.* 52, 171–188. doi:10.1007/BF02235668.
- Nakano, T., Kaneko, I., Soga, T., Tsujino, H., Yasuda, T., Ishizaki, H., et al. (2007). Mid-depth freshening in the North Pacific subtropical gyre observed along the JMA repeat and WOCE hydrographic sections. *Geophys. Res. Lett.* 34, 1–6. doi:10.1029/2007GL031433.
- Nakano, T., Kitamura, T., Sugimoto, S., Suga, T., and Kamachi, M. (2015). Long-term variations of North Pacific Tropical Water along the 137°E repeat hydrographic section. *J. Oceanogr.* 71, 229–238. doi:10.1007/s10872-015-0279-3.
- Nan, F., Yu, F., Xue, H., Wang, R., and Si, G. (2015). Ocean salinity changes in the northwest Pacific subtropical gyre: The quasi-decadal oscillation and the freshening trend. *J. Geophys. Res. C Ocean.* 120, 2179–2192. doi:10.1002/2014JC010536.
- Newman, M., Alexander, M. A., Ault, T. R., Cobb, K. M., Deser, C., Di Lorenzo, E., et al. (2016). The Pacific decadal oscillation, revisited. *J. Clim.* 29, 4399–4427. doi:10.1175/JCLI-D-15-0508.1.
- Nieves, D., and Spall, M. Propagation of North Atlantic Deep Water Anomalies. doi:10.1175/JPO-D-18-0068.1.
- Nishikawa, S., Tsujino, H., Sakamoto, K., and Nakano, H. (2010). Effects of mesoscale eddies on subduction and distribution of subtropical mode water in an eddy-resolving OGCM of the Western North PACIFIC. *J. Phys. Oceanogr.* 40, 1748–1765. doi:10.1175/2010JPO4261.1.
- Nishikawa, S., Tsujino, H., Sakamoto, K., and Nakano, H. (2013). Diagnosis of water mass transformation and formation rates in a high-resolution GCM of the North Pacific. *J. Geophys. Res. Ocean.* 118, 1051–1069. doi:10.1029/2012JC008116.
- Nonaka, M., and Sasaki, H. (2007). Formation mechanism for isopycnal temperature-salinity anomalies propagating from the Eastern South Pacific to the Equatorial region. *J. Clim.* 20, 1305–1315. doi:10.1175/JCLI4065.1.
- Nonaka, M., and Xie, S.-P. (2000). Propagation of North Pacific interdecadal subsurface temperature anomalies in an ocean GCM. *Geophys. Res. Lett.* 27, 3747–3750. doi:10.1029/2000GL011488.
- Ogata, T., and Nonaka, M. (2020). Mechanisms of Long-Term Variability and Recent Trend of Salinity Along 137°E. *J. Geophys. Res. Ocean.* 125. doi:10.1029/2019JC015290.
- Oka, E., Katsura, S., Inoue, H., Kojima, A., Kitamoto, M., Nakano, T., et al. (2017). Long-term change and variation of salinity in the western North Pacific subtropical gyre revealed by 50-year long observations along 137°E. *J. Oceanogr.* 73, 479–490. doi:10.1007/s10872-017-0416-2.

- Oka, E., Kouketsu, S., Toyama, K., Uehara, K., Kobayashi, T., Hosoda, S., et al. (2011). Formation and subduction of central mode water based on profiling float data, 2003-08. *J. Phys. Oceanogr.* 41, 113–129. doi:10.1175/2010JPO4419.1.
- Oka, E., Kouketsu, S., Yanagimoto, D., Ito, D., Kawai, Y., Sugimoto, S., et al. (2020). Formation of Central Mode Water based on two zonal hydrographic sections in spring 2013 and 2016. *J. Oceanogr.* 76, 373–388. doi:10.1007/s10872-020-00551-9.
- Oka, E., Qiu, B., Kouketsu, S., Uehara, K., and Suga, T. (2012). Decadal seesaw of the Central and Subtropical Mode Water formation associated with the Kuroshio Extension variability. *J. Oceanogr.* 68, 355–360. doi:10.1007/s10872-011-0098-0.
- Oka, E., Qiu, B., Takatani, Y., Enyo, K., Sasano, D., Kosugi, N., et al. (2015). Decadal variability of Subtropical Mode Water subduction and its impact on biogeochemistry. *J. Oceanogr.* 71, 389–400. doi:10.1007/s10872-015-0300-x.
- Oka, E., and Suga, T. (2003). Formation region of North Pacific subtropical mode water in the late winter of 2003. *Geophys. Res. Lett.* 30, 2205. doi:10.1029/2003GL018581.
- Oka, E., and Suga, T. (2005). Differential formation and circulation of North Pacific Central Mode Water. *J. Phys. Oceanogr.* 35, 1997–2011. doi:10.1175/JPO2811.1.
- Oka, E., Toyama, K., and Suga, T. (2009). Subduction of North Pacific central mode water associated with subsurface mesoscale eddy. *Geophys. Res. Lett.* 36, 3–6. doi:10.1029/2009GL037540.
- Oka, E., Yamada, K., Sasano, D., Enyo, K., Nakano, T., and Ishii, M. (2019). Remotely Forced Decadal Physical and Biogeochemical Variability of North Pacific Subtropical Mode Water Over the Last 40 Years. *Geophys. Res. Lett.* 46, 1555–1561. doi:10.1029/2018GL081330.
- Pan, A., and Liu, Q. (2005). Mesoscale eddy effects on the wintertime vertical mixing in the formation region of the North Pacific Subtropical Mode Water. *Chinese Sci. Bull.* 50, 1949–1956. doi:10.1360/982004-757.
- Qiu, B., and Chen, S. (2005). Variability of the Kuroshio Extension jet, recirculation gyre, and mesoscale eddies on decadal time scales. *J. Phys. Oceanogr.* 35, 2090–2103. doi:10.1175/JPO2807.1.
- Qiu, B., and Chen, S. (2006). Decadal variability in the formation of the North Pacific subtropical mode water: Oceanic versus atmospheric control. *J. Phys. Oceanogr.* 36, 1365–1380. doi:10.1175/JPO2918.1.
- Qiu, B., Chen, S., and Hacker, P. (2007). Effect of mesoscale eddies on subtropical mode water variability from the Kuroshio Extension System Study (KESS). *J. Phys. Oceanogr.* 37, 982–1000. doi:10.1175/JPO3097.1.
- Qiu, B., Chen, S., Schneider, N., Oka, E., and Sugimoto, S. (2021). On the reset of the wind-forced decadal kuroshio extension variability in late 2017. *J. Clim.* 33, 10813–10828. doi:10.1175/JCLI-D-20-0237.1.

- Qiu, B., Chen, S., Schneider, N., and Taguchi, B. (2014). A coupled decadal prediction of the dynamic state of the kuroshio extension system. *J. Clim.* 27, 1751–1764. doi:10.1175/JCLI-D-13-00318.1.
- Qiu, B., Huang, R., Bo Qiu, and Rui Xin Huang (1995). Ventilation of the North Atlantic and North Pacific: subduction versus obduction. *J. Phys. Oceanogr.* 25, 2374–2390. doi:10.1175/1520-0485(1995)025<2374:votnaa>2.0.co;2.
- Qu, T., and Chen, J. (2009). A North Pacific decadal variability in subduction rate. *Geophys. Res. Lett.* 36. doi:10.1029/2009GL040914.
- Qu, T., Xie, S. P., Mitsudera, H., and Ishida, A. (2002). Subduction of the North Pacific mode waters in a global high-resolution GCM. *J. Phys. Oceanogr.* 32, 746–763. doi:10.1175/1520-0485(2002)032<0746:SOTNPM>2.0.CO;2.
- Ren, L., and Riser, S. C. (2010). Observations of decadal time scale salinity changes in the subtropical thermocline of the North Pacific Ocean. *Deep. Res. Part II Top. Stud. Oceanogr.* 57, 1161–1170. doi:10.1016/j.dsr2.2009.12.005.
- Roemmich, D., Johnson, G. C., Riser, S., Davis, R., Gilson, J., Owens, W. B., et al. (2009). The Argo Program: Observing the global ocean with profiling floats. *Oceanography* 22, 34–43. doi:10.5670/oceanog.2009.36.
- Ruddick, B. (1983). A practical indicator of the stability of the water column to double-diffusive activity. *Deep Sea Res. Part A, Oceanogr. Res. Pap.* 30, 1105–1107. doi:10.1016/0198-0149(83)90063-8.
- Saito, H., Suga, T., Hanawa, K., and Shikama, N. (2011). The transition region mode water of the North Pacific and its rapid modification. *J. Phys. Oceanogr.* 41, 1639–1658. doi:10.1175/2011JPO4346.1.
- Saito, H., Suga, T., Hanawa, K., and Watanabe, T. (2007). New type of pycnostad in the western subtropical-subarctic transition region of the North Pacific: Transition Region Mode Water. *J. Oceanogr.* 63, 589–600. doi:10.1007/s10872-007-0052-3.
- Sasaki, Y. N., Schneider, N., Maximenko, N., and Lebedev, K. (2010). Observational evidence for propagation of decadal spiciness anomalies in the North Pacific. *Geophys. Res. Lett.* 37, n/a-n/a. doi:10.1029/2010GL042716.
- Schmitt, R. W. (1981). Form of the temperature-salinity relationship in the central water: Evidence for double-diffusive mixing. *J. Phys. Oceanogr.* 11, 1015–1026. doi:10.1175/1520-0485(1981)011<1015:FOTTSR>2.0.CO;2.
- Schneider, N. (2000). A decadal spiciness mode in the tropics. *Geophys. Res. Lett.* 27, 257–260. doi:10.1029/1999GL002348.
- Schneider, N., Miller, A. J., Alexander, M. A., and Deser, C. (1999a). Subduction of decadal North Pacific temperature anomalies: Observations and dynamics. *J. Phys. Oceanogr.* 29, 1056–1070. doi:10.1175/1520-0485(1999)029<1056:SODNPT>2.0.CO;2.
- Schneider, N., Miller, A. J., and Pierce, D. W. (2002). Anatomy of North Pacific decadal variability. *J. Clim.* 15, 586–605. doi:10.1175/1520-0442(2002)015<0586:AONPDV>2.0.CO;2.

Schneider, N., Venzke, S., Miller, A. J., Pierce, D. W., Barnett, T. P., Deser, C., et al. (1999b). Pacific thermocline bridge revisited. *Geophys. Res. Lett.* 26, 1329–1332. doi:10.1029/1999GL900222.

Skliris, N., Marsh, R., Josey, S. A., Good, S. A., Liu, C., and Allan, R. P. (2014). Salinity changes in the World Ocean since 1950 in relation to changing surface freshwater fluxes. *Clim. Dyn.* 43, 709–736. doi:10.1007/S00382-014-2131-7.

Suga, T., and Hanawa, K. (1995). Interannual variations of north pacific subtropical mode water in the 137°E section. *J. Phys. Oceanogr.* 25, 1012–1017. doi:10.1175/1520-0485(1995)025<1012:IVONPS>2.0.CO;2.

Suga, T., Kato, A., and Hanawa, K. (2000). North Pacific Tropical Water: its climatology and temporal changes associated with the climate regime shift in the 1970s. Available at: www.elsevier.com/locate/pocean.

Suga, T., Motoki, K., and Hanawa, K. (2003). Subsurface water masses in the Central North Pacific transition region: The repeat section along the 180° meridian. *J. Oceanogr.* 59, 435–444. doi:10.1023/A:1025536531583.

Suga, T., Saito, H., Toyama, K., Watanabe, T., and Oceanography, C. (2013). Water Mass Formation, Modification and Subduction in and around the Subarctic Frontal Zone in the North Pacific. *Bull. Coast. Oceanogr.* 50, 103–118. doi:10.32142/engankaiyo.50.2_103.

Suga, T., Sato, K., Nonaka, M., Hosoda, S., Ueno, H., Shikama, N., et al. (2012). A REVISIT TO CAUSES OF THE NORTH PACIFIC CENTRAL MODE WATER PROPERTY CHANGES ASSOCIATED WITH REGIME SHIFTS. Proceeding, 21–25. Available at: <http://www.aviso.oceanobs.com> [Accessed March 28, 2022].

Suga, T., Takei, Y., and Hanawa, K. (1997). Thermostat distribution in the North Pacific subtropical gyre: The central mode water and the subtropical mode water. *J. Phys. Oceanogr.* 27, 140–152. doi:10.1175/1520-0485(1997)027<0140:TDITNP>2.0.CO;2.

Sugimoto, S. (2005). Remote reemergence areas of winter sea surface temperature anomalies in the North Pacific. *Geophys. Res. Lett.* 32, L01606. doi:10.1029/2004GL021410.

Sugimoto, S., and Hanawa, K. (2007). Further evidence for non-reemergence of winter SST anomalies in the North Pacific eastern subtropical mode water area. *J. Oceanogr.* 63, 625–635. doi:10.1007/s10872-007-0055-0.

Sugimoto, S., and Hanawa, K. (2010). Impact of Aleutian Low activity on the STMW formation in the Kuroshio recirculation gyre region. *Geophys. Res. Lett.* 37, 3606. doi:10.1029/2009GL041795.

Sugimoto, S., Takahashi, N., and Hanawa, K. (2013). Marked freshening of North Pacific subtropical mode water in 2009 and 2010: Influence of freshwater supply in the 2008 warm season. *Geophys. Res. Lett.* 40, 3102–3105. doi:10.1002/grl.50600.

Taguchi, B., and Schneider, N. (2014). Origin of decadal-scale, eastward-propagating heat content anomalies in the North Pacific. *J. Clim.* 27, 7568–7586. doi:10.1175/JCLI-D-13-00102.1.

Taguchi, B., Schneider, N., Nonaka, M., and Sasaki, H. (2017). Decadal variability of upper-ocean heat content associated with meridional shifts of western boundary current extensions in the North Pacific. *J. Clim.* 30, 6247–6264. doi:10.1175/JCLI-D-16-0779.1.

Talley, L. D. (1988). Potential Vorticity Distribution in the North Pacific. American Meteorological Society doi:10.1175/1520-0485(1988)018<0089:PVDITN>2.0.CO;2.

Talley, L. D. (1993). Distribution and Formation of North Pacific Intermediate Water. *J. Phys. Oceanogr.* 23, 517–537.

Taneda, T., Suga, T., and Hanawa, K. (2000). Subtropical mode water variation in the northwestern part of the North Pacific subtropical gyre. *J. Geophys. Res. Ocean.* 105, 19591–19598. doi:10.1029/2000jc900073.

Toyama, K. (2015). Interannual variation of annual subduction rate in the North Pacific estimated from a gridded Argo product.

Toyama, K., and Suga, T. (2010). Vertical structure of North Pacific mode waters. *Deep. Res. Part II Top. Stud. Oceanogr.* 57, 1152–1160. doi:10.1016/j.dsr2.2009.12.004.

Tsubouchi, T., Suga, T., and Hanawa, K. (2016). Comparison study of subtropical mode waters in the world ocean. *Front. Mar. Sci.* 3, 1–15. doi:10.3389/fmars.2016.00270.

Turner, J. S. (1973). Buoyancy Effects in Fluids. doi:10.1017/CBO9780511608827.

Uehara, H., Suga, T., Hanawa, K., and Shikama, N. (2003). A role of eddies in formation and transport of North Pacific Subtropical Mode Water. *Geophys. Res. Lett.* 30, 1999–2002. doi:10.1029/2003GL017542.

Usui, N., Wakamatsu, T., Tanaka, Y., Hirose, N., and Toyoda, T. (2017). Four - dimensional variational ocean reanalysis : a 30 - year high - resolution dataset in the western North Pacific. *J. Oceanogr.* 73, 205–233. doi:10.1007/s10872-016-0398-5.

Vallis, G. K. (2006). *Atmospheric and Oceanic Fluid Dynamics*. doi:10.1017/cbo9780511790447.

Wong, A. P. S., Bindoff, N. L., and Church, J. A. (2001). Freshwater and heat changes in the North and South Pacific Oceans between the 1960s and 1985-94. *J. Clim.* 14, 1613–1633. doi:10.1175/1520-0442(2001)014<1613:FAHCIT>2.0.CO;2.

Xie, S. P., Kunitani, T., Kubokawa, A., Nonaka, M., and Hosoda, S. (2000). Interdecadal thermocline variability in the North Pacific for 1958-97: A GCM simulation. *J. Phys. Oceanogr.* 30, 2798–2813. doi:10.1175/1520-0485(2000)030<2798:ITVITN>2.0.CO;2.

Yan, Y., Xu, D., Yu, K., and Qi, Y. (2017). Propagation of the subsurface freshening water and its major source in the northwestern Pacific. *J. Geophys. Res. Ocean.* 122, 6857–6871. doi:10.1002/2017JC013033.

Yasuda, I. (2003). Hydrographic structure and variability in the Kuroshio-Oyashio Transition Area. *J. Oceanogr.* 59, 389–402. doi:10.1023/A:1025580313836.

Yasuda, T., and Hanawa, K. (1997). Decadal changes in the mode waters in the midlatitude North Pacific. *J. Phys. Oceanogr.* 27, 858–870. doi:10.1175/1520-0485(1997)027<0858:DCITMW>2.0.CO;2.

Yeager, S. G., and Large, W. G. (2004). Late-winter generation of spiciness on subducted isopycnals. *J. Phys. Oceanogr.* 34, 1528–1547. doi:10.1175/1520-0485(2004)034<1528:LGOSOS>2.0.CO;2.

Zhang, L., and Qu, T. (2014). Low-frequency variability of South Pacific Tropical Water from Argo. *Geophys. Res. Lett.* 41, 2441–2446. doi:10.1002/2014GL059490.

Zhang, R. H., and Liu, Z. (1999). Decadal thermocline variability in the North Pacific Ocean: Two pathways around the subtropical gyre. *J. Clim.* 12, 3273–3296. doi:10.1175/1520-0442(1999)012<3273:DTVITN>2.0.CO;2.